Model-Based Battery Management Systems: From Theory to Practice

Manan Pathak

A dissertation

submitted in partial fulfillment of the

requirements for the degree of

Doctor of Philosophy

University of Washington

2017

Committee

Venkat R. Subramanian (Chair)

Daniel T. Schwartz

Eric Stuve

Jihui Yang

Shriram Santhanagopalan

Program Authorized to Offer Degree:

Chemical Engineering

University of Washington

Abstract

Model-based Battery Management Systems: From Theory to Practice

Manan Pathak

Chair of the Supervisory Committee:

Prof. Venkat R. Subramanian

Department of Chemical Engineering

Lithium-ion batteries are now extensively being used as the primary storage source. Capacity and power fade, and slow recharging times are key issues that restrict its use in many applications. Battery management systems are critical to address these issues, along with ensuring its safety. This dissertation focuses on exploring various control strategies using detailed physics-based electrochemical models developed previously for lithium-ion batteries, which could be used in advanced battery management systems. Optimal charging profiles for minimizing capacity fade based on SEI-layer formation are derived and the benefits of using such control strategies are shown by experimentally testing them on a 16 Ah NMC-based pouch cell. This dissertation also explores different time-discretization strategies for non-linear models, which gives an improved order of convergence for optimal control problems.

Lastly, this dissertation also explores a physics-based model for predicting the linear impedance of a battery, and develops a freeware that is extremely robust and computationally fast. Such a code could be used for estimating transport, kinetic and material properties of the battery based on the linear impedance spectra.

Table of Contents

List of Figures

List of Tables

Acknowledgments

This marathon called PhD has been a fascinating journey and I want to thank all the people involved in making it a truly memorable one. I want to express my sincere gratitude towards my advisor Prof. Venkat Subramanian who accepted me into his group in 2013, and brought me to the University of Washington in Seattle in 2014. I want to thank him for his advice, his encouragement, and at times even pushing me to work hard during my doctoral education. His passion for numerical algorithms and mathematical problems has truly been an inspiration for me throughout my PhD. I have always been amazed to see his energy for working on codes, even during off-work hours, late nights and even at times on weekends. I am especially thankful to him for working with me on numerous problems and for his constructive criticism throughout my PhD.

I want to thank my committee members Prof. Eric Stuve and Prof. Jihui Yang for their suggestions and for critically reviewing this dissertation. I am grateful to Prof. Dan Schwartz for his invaluable feedback and guidance throughout this work, and for being a great mentor. I want to thank Dr. Shriram Santhanagopalan for all his suggestions and critical feedback throughout this work. He has been a wonderful collaborator and I have truly enjoyed working with him throughout the course of the ARPA-E project.

I would like to acknowledge the financial support from the US Department of Energy, Advanced Projects Research Agency- Energy (ARPA-E), award number DE-AR0000275. I am thankful to the Clean Energy Institute at the UW for giving me a fellowship, and for providing me with wonderful opportunities to interact with various seminar speakers, and other industry personnel that has helped me immensely not only in my research but also in my overall professional development. I want to thank Suzanne, Jill, Shawn, Adam and Renee at the CEI for their constant

help with the logistics. I am also grateful to the entire administrative staff of the Department of Chemical Engineering: Joanne, Debbie, Ao, Noel, Caroline, Rex, Nicole, Dave and Allison for helping me in a smooth transition to Seattle, and for patiently answering my perpetual questions.

I am thankful to all the past and present members of the MAPLE lab. I would like to thank Dr. Paul Northrop, Dr. Sumitava De, Dr. Bharat Suthar and Dr. Venkat Ramadesigan for all the countless discussions on batteries physics and thermodynamics. Thanks also to Dr. Matt Lawder who taught me how to effectively communicate our research to the outside audience. I am grateful to Seongbeom, Yanbo, Jerry, Neal, Caitlin, Tae-Jin, Mengdi and Akshay. It has been a pleasure to work with and especially learning from everyone in the lab. I am grateful to Dr. Kishalay Mitra, Dr. Dayaram Sonawane and Dr. Suryanarayana Kolluri for their help with control and optimization theory, for their guidance and for working with me on various problems during their stay at the MAPLE lab. I am also thankful to all the friends at the UW ECS student chapter who have helped in advancing my learning through discussions during the book and journal club meetings.

I wish to acknowledge the support of all the Umang friends: Arun, Kushal, Zeba, Khushmeen, Prabhleen, Vidit and Varun. They have been wonderful juniors and great friends. Varun has been an awesome roommate and I am thankful to him for helping with cooking and other house activities during last several months of finishing this dissertation. Khushmeen's ever smiling face has always been a stress-reliever, and Zeba has been tremendous at keeping everyone together. I also want to thank the entire *Swadhyay* family, and especially *Lt. Dada*, whose teachings have been a guiding light, and continues to motivate me to learn more.

I am forever indebted to Prof. A.K. Suresh at the IIT Bombay for believing in me, sowing the seeds of research, and motivating me to pursue a PhD. A word of thanks must all go to my first year

undergraduate friends, especially Divyash and Praveen, who helped me a lot during my stay at the IITB, and then Atish and Ishan, who helped me get accustomed to US right after I moved. I have learnt a lot from them throughout my undergradaute education. I would also like to thank Sharda for her constant and unwavering support and friendship, and for her countless skype sessions over the weekends.

I would also like to thank Ben Saheb for their blessings. And finally, I would like to thank my family: Mom, Dad and my brother Chintan for their constant support and encouragement. They have been the source of my strength throughout. It has been truly special to be able to work with Chintan in the same lab, and continuously learn from him, as I always have ever since my childhood. It is to them, that I dedicate all my achievements.

Manan Pathak

University of Washigton, Seattle

December 2017

Dedicated to Mom, Dad and Chintan

Chapter 1: What is a Battery Management System?

1.1. Introduction and Background

With the increase in global warming, there is an increasing emphasis on renewable and clean energy. Alternative energy sources are aggressively being investigated and developed. Norway has become the first country to ban fuel-based cars by 2025, pushing the development of electric vehicles (EVs). With programs such as Advanced Research Projects Agency – Energy (ARPA-E) sponsored by the U.S. Department of Energy (US-DOE) and the recent announcement of a $50M grant for the Battery500 initiative,[1] the U.S. government is also encouraging the commercialization of electric vehicles (EVs). Apart from the automobile industry, the economics of distributed energy resources for power generation are also becoming increasingly favorable. The efficient use of these systems composed of intermittent renewable sources, such as wind and solar energy, depends critically on the efficiency of energy storage technologies.

1.2. Electrochemical Energy Storage Sources

Electrochemical energy storage sources are required to store the energy generated from renewable energy sources. As the wind and solar energy is intermittent, storage alternatives are required to store energy whenever excess generation is available, and stored energy can later be used when the generation is low. Typically, electrochemical storage sources can be broadly classified into four main categories, namely, capacitors, electrochemical double layer capacitors (EDLCs), batteries and fuel cells. Figure 1-1 shows the Ragone plot comparison of various electrochemical energy storage devices. An ideal storage device should be able to provide a very high energy density at very high power, and should lie in the top right of Figure 1-1. Traditional and double

layer capacitors have a very low resistance to charge and discharge, providing very high power densities. They have very high reliability, durability, very low maintenance, long lifetime,

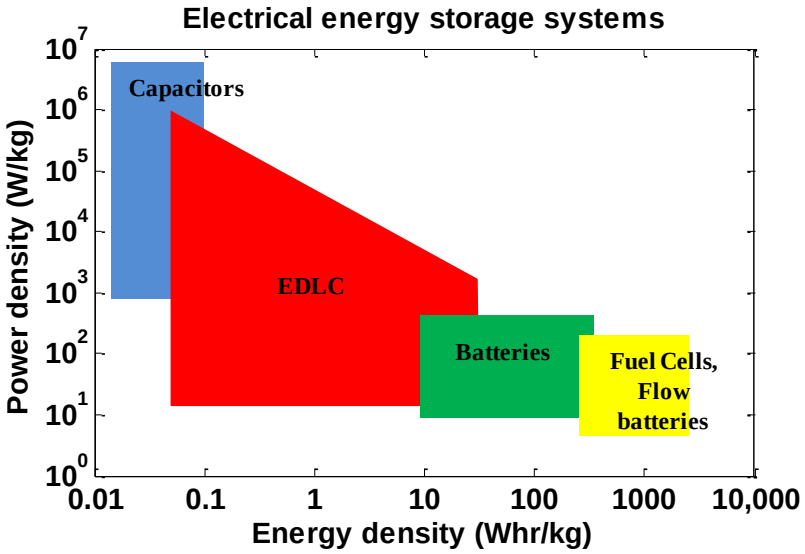

Figure 1-1: Ragone plot depicting power and energy density of electrical energy storage systems, (figure adapted from Nguyen and Savinell.[2] Reproduced by permission of The Electrochemical Society)

and operate over a wide range of temperature and environmental conditions. They are also environmentally friendly, and can be easily recycled. However, they offer very low energy density, which limits their usage in applications requiring very high charge/discharge rates. For example, modern EVs or plug-in hybrid electric vehicles (PHEVs) use capacitors to store the energy generated through regenerative braking, before transferring that energy to batteries, as it is generated at a very high rate, during very short time duration.[3-5] Directly putting that energy into batteries results in the batteries experiencing very high charge rates, which could lead to a higher capacity fade. Capacitors and EDLCs store energy by storing electrical charge at their surface, without involving any charge transfer across the interface or any electrochemical reaction, which limits their energy density. Batteries on the other hand, store charge inside the bulk material and

involve faradaic reactions for charge transfer. Availability of active bulk material allows a higher energy that can be stored in batteries. However, the diffusion, transport and kinetic resistance encountered while charge transfer, affects the power output in batteries.

Several kinds of batteries are available in the market, ranging from lead acid, to Nickel-based batteries, lithium-ion or lithium-sulfur batteries and even flow batteries. Different batteries have different mechanisms of storing energy. Recently, intercalation-based batteries have gained prominence, with lithium-based batteries being the frontrunners. On the other hand, flow batteries primarily store energy as electroactive materials in outside tanks, and a continuous flow of the electrolyte delivers the desired energy, depending on the requirement of the application. However, the use of a battery can be very application-specific depending on the requirement of the particular application. For example, consumer electronics and EV applications currently use lithium-based batteries because of its high energy density, while stationary storage applications which do not have space or weight constraints can use any kind of battery, including flow batteries, which can provide very high energy density, but provide very low cycle life or power density.

1.3. Lithium-ion Battery

A lithium-ion battery works on the principle of intercalation, and has been an active area of research for the past several years. Figure 1-2 shows a typical schematic of a lithium-ion battery. The positive electrode or cathode consists of a lithium-metal oxide (such as $LiMnO_2$, $LiCoO_2$, or $LiFePO_4$), and the negative electrode or anode consists of graphite. These materials store energy by storing lithium particles inside their interstitial sites. The two electrodes are separated by a porous membrane called separator, which allows free movement of ions across the electrodes. An organic solvent, such as ethyl carbonate (EC) or dimethyl carbonate (DMC) is used as an

electrolyte because of its stability in the operating potential window of a lithium-ion battery. A lithium-ion battery takes advantage of the thermodynamic electrochemical potential difference of the electrode materials, which gets converted to useful work. While discharging, lithium particles deintercalate from the anode and react at the solid-electrolyte interface to form lithium ions. The lithium ions then migrate inside the electrolyte from the anode to the cathode side through the separator. At the cathode, the lithium ions react again at the solid-electrolyte interface and the resulting lithium particle gets intercalated inside the cathode. The reverse of this entire process takes place while the battery is being charged, where lithium ions migrate from the cathode to the anode side. The electrochemical potential of the electrode material changes with the change in the occupancy of the interstitial sites by the lithium particles, inside the host material. Active research is being pursued to design new materials for both electrodes, which could provide higher energy/power densities, or could enhance the performance of the battery by reducing the transport or kinetic resistance.

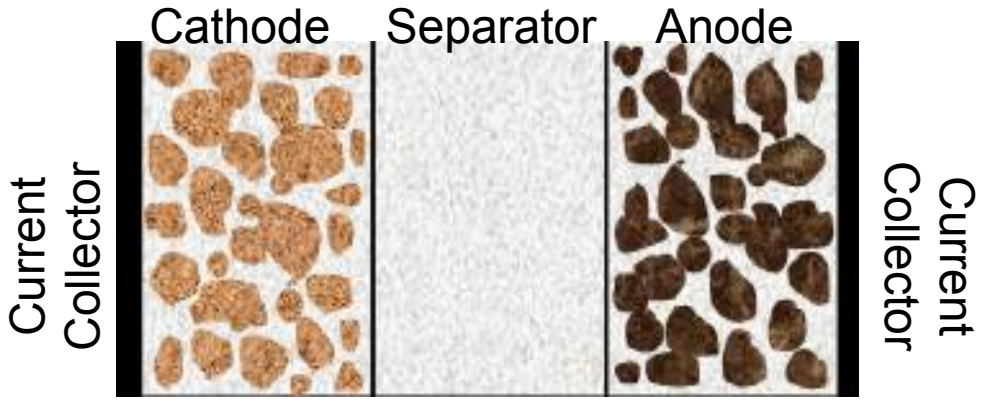

Figure 1-2: Typical diagram of a lithium-ion battery cell system, (figure adapted from Ramadesigan *et. al.*[6] Reproduced by permission of The Electrochemical Society)

While a lot of work has already been done since its commercialization, more research is needed to ensure the batteries are utilized to its full extent. The performance of a lithium-ion battery depends on the conditions of its use, along with the state of its internal variables such as state-of-charge etc. Current issues with lithium-ion batteries for the end users are cost, safety, and cycle-life, whereas at the system level, the critical issues are underutilization, capacity fade, thermal runaways, and lower energy density. These issues in turn depend on the internal working of the cell associated with the Solid-Electrolyte Interface (SEI)-layer growth, unwanted side reactions, mechanical degradation, loss of active material, and the increase of various internal resistances such as ohmic and mass transfer resistance. Active research is being pursued to mitigate these issues. Figure 1-3 shows a spider plot from the US-DOE with the USABC goals for EVs, and the current state of the lithium-ion batteries with respect to these goals.

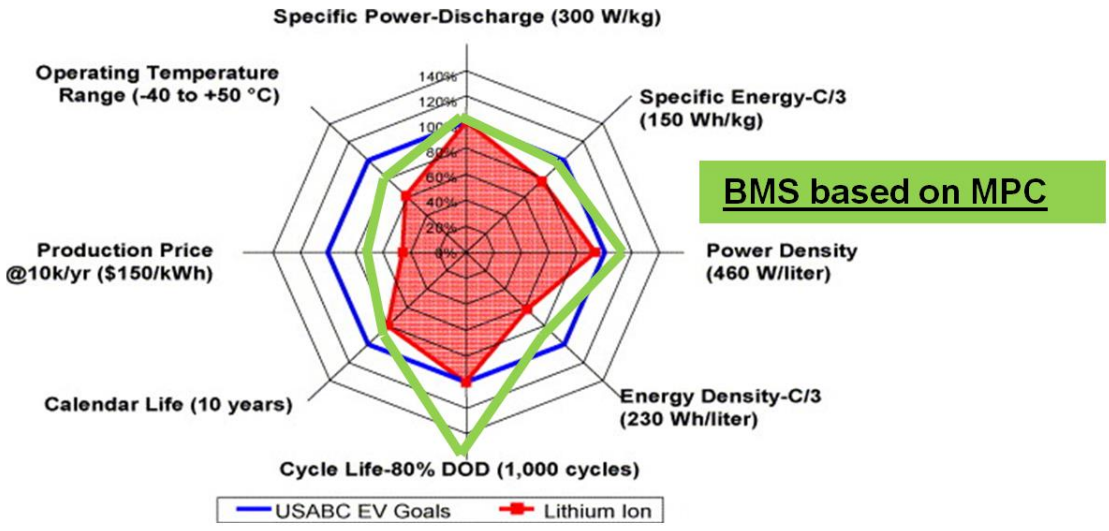

Figure 1-3: Spider plot showing USABC EV goals (figure taken from the website of US-DOE) Green line marks the space that could be achieved through a BMS based on model predictive control (MPC)

Various system-level strategies are being investigated to increase the efficiency of existing and emerging systems. At the system level, battery management systems (BMS) play a critical role in managing the battery. A BMS that accounts for the physics of the battery can provide extended benefits without making any changes to the existing cell chemistry or the control hardware. Exploring this in detail is the fundamental goal of this dissertation.

1.4. Battery Management Systems

A BMS is a device that is responsible for safe and optimum operation of a battery (pack). A BMS is therefore required wherever a battery is found. It is responsible for monitoring the voltage, current and temperature of the battery as well as predicts the State of Charge (SOC) of the battery and estimates the time remaining before the battery is completely discharged. It also contains elements and logic for over and under-voltage protection as well as other limits on current, temperature etc. Depending on the importance and cost of the system, the features of a BMS may vary. Figure 1-4 shows a typical battery system diagram.

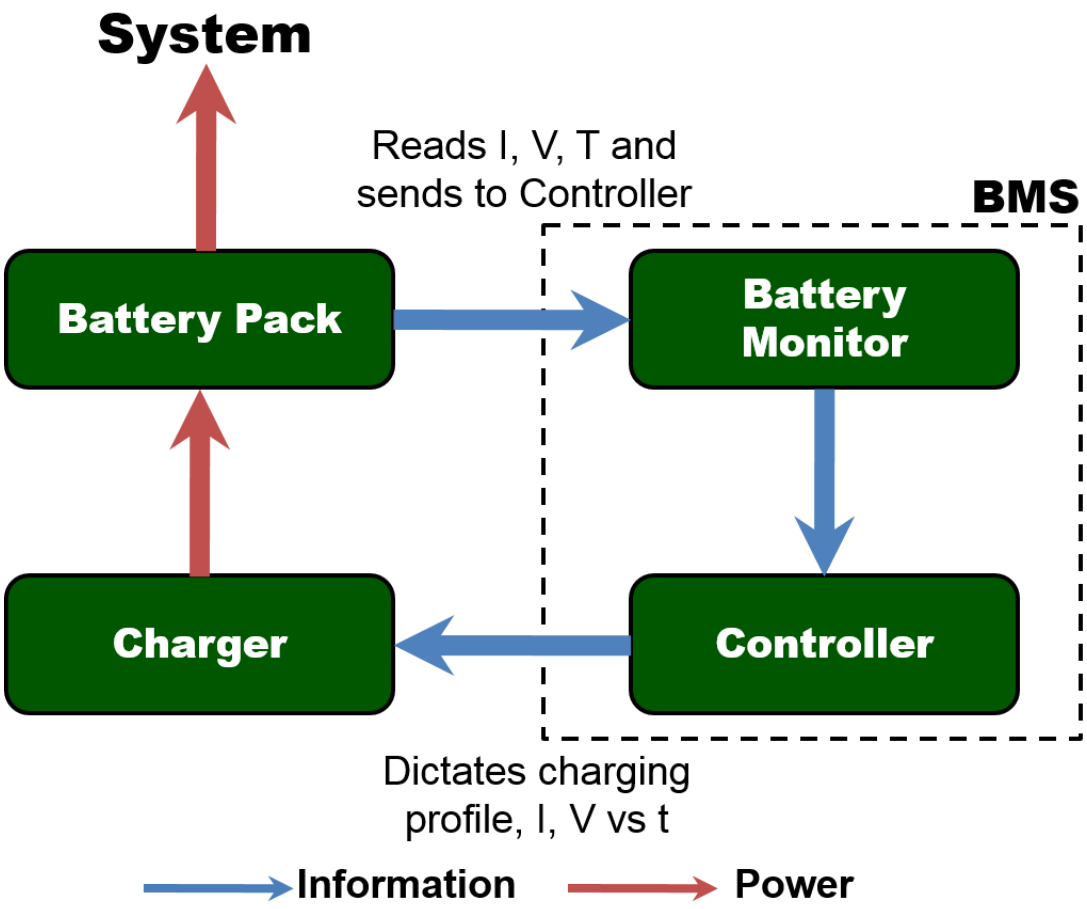

Figure 1-4: Typical Battery System Diagram

As such the battery deployments can be distinguished as under:

A. *Based on mobility*: Depending on how the device is being commonly used, it can either be of following types:

1) Stationary - These systems are typically found in applications like electric grids, commercial and industrial buildings, etc.

2) Mobile - These are found in EVs of various sizes, wheelchairs, e-bikes, cars, trucks and consumer electronics like cell-phones etc.

B. Based on function of portable device: Whether the system where the battery and BMS is deployed is a

1) Sensor: These devices collect information from the environment like a thermometer, etc.
2) Actuator: These devices perform a predefined action at command, like a switch or a motor etc.
3) Control System: These devices may employ a set of sensors and actuators, like laptop, EVs etc.

C. Based on charging capability:

1) Wireless: The new breed of wireless chargers allow for contact-less, hassle-free charging.
2) Wired: Typical charging using wires is perfect for transferring reliable, high power for charging.

D. Based on availability of on-board accessories:

1) Computational Power: Pool of computational resources available for the system can be bifurcated into local, edge and cloud based where each resource has its associated reliability and reaction time.
2) Sensors: Contains one or more sensors on-board providing system information like temperature, voltage, current, GPS, etc. for helping establish the context.
3) Programmability: Systems often feature programmable chargers, which can receive directions from BMS controller, which can guide the charging/discharging method.

E. Condition Monitoring Capability:

1) Cell-traceability through life: If the BMS contains sensors as well as capability to store the cell-usage data throughout the life of the cell.

2) Intermittent monitoring: Sensors maybe available, but the usage data is not stored or stored infrequently.

3) No monitoring: Some systems may not have many sensors or storage capability.

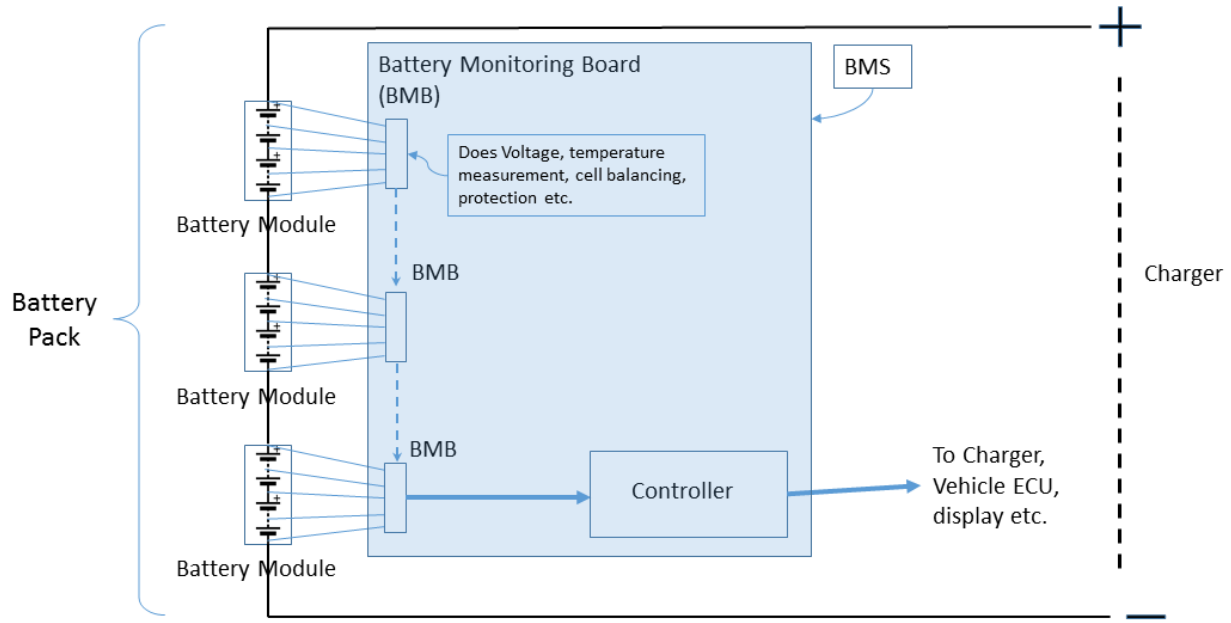

Figure 1-5: Example multi-cell battery system like found in EVs

Multi-cell systems often need hierarchical monitoring and control. Figure 1-5 shows an example of a multi-cell system found in EVs. It is composed of several modules connected in series. Each module in turn may contain several cells in series, where each cell can be a single cell or several cells in parallel.

There are several BMS topologies, i.e. the hierarchy of monitoring and control depending again on the application. Figure 1-6 shows the common topologies in use.

Centralized BMS: In a centralized BMS, the main control board as well as the cell-monitoring control boards is collocated in one single unit.

Distributed BMS: In a distributed BMS, there is a master controller that is located centrally, and gets its feed from several monitoring boards that are mounted on battery modules. Based on the information from individual modules, the master controller then decides to operate the pack, such that individual battery modules remain safe. This is the typical system that is used in most high voltage installations such as EVs.

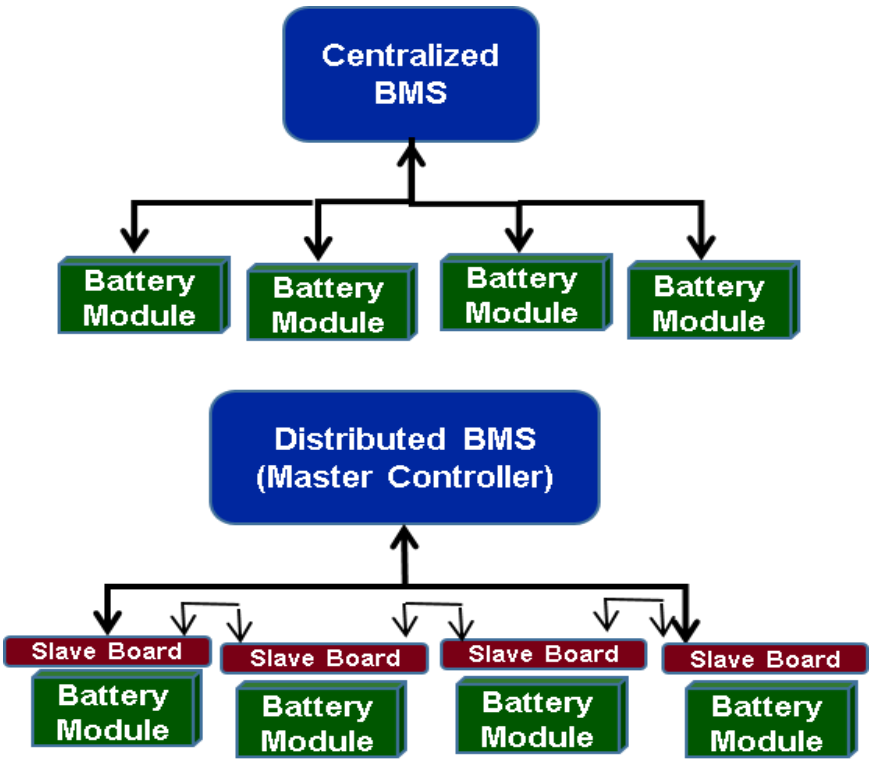

Figure 1-6: BMS Topologies, Centralized and Distributed

In a battery pack, the cells that are connected in parallel always remain at the same voltage. However, even if the cells are identical and from the same manufacturing batch, during operation, the cells connected in series might have different voltages. This may be due to slight manufacturing differences that get added up over time, or because the cells in different parts of the pack might encounter different environmental conditions. Due to these differences, the cells connected in

series might undergo different capacity fade. As the dynamics of the cell is governed by the weakest cell connected in series, it is essential for the BMS to ensure the cells connected in series remain balanced in their voltage/SOC at all times. The typical balancing methods are passive and active balancing. Passive balancing is easier to implement as the current is easily drained off through certain resistors. However, this leads to unnecessary wastage of energy as Joule's heating. Active balancing is more complicated, as the energy from the cells with the higher SOC is transferred to the cells with the lower SOC by the BMS, while the charging is active. In case if there is a thermal management system (TMS) for the battery pack, the BMS must also communicate with the TMS to ensure that the cells experience the adequate and desired environmental temperature conditions.

1.5. Battery Modeling

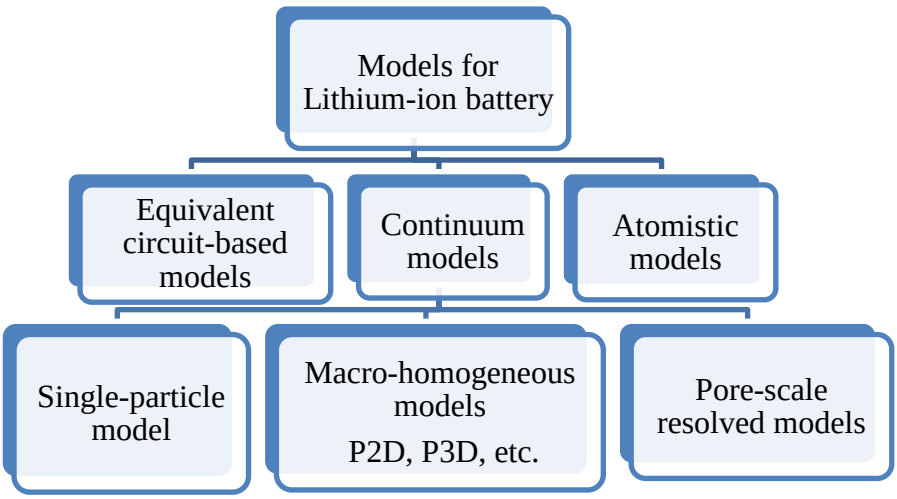

Figure 1-7: Some modeling frameworks for the lithium-ion battery (figure adapted from the PhD thesis of Bharat Suthar[7])

Most of the currently available BMS use empirical or lookup table-based models to predict the internal states of the battery.[8] While computationally easy to solve, these models are not always accurate.[9] The inaccuracy increases as the battery degrades as it cycles. Use of continuum-level

physics-based battery models is an alternative to empirical models. Battery models based on transport, physical, electrochemical and thermodynamics principles can be used to monitor the internal states of the battery and to obtain optimal control strategies. Below, we briefly review the most common continuum physics-based models, namely the single particle model, and the pseudo two-dimensional model.

1.5.1 Single Particle Model

The simplest physics-based model is the single particle model (SPM). This model accounts for the intercalation and deintercalation of lithium particles inside the electrode by assuming the dynamics being governed by the Fick's law of diffusion. The charge transfer reaction is assumed to take place at the surface of the electrode particle, and follows Butler-Volmer type reaction kinetics. The model ignores the dynamics in the electrolyte phase, and does not account for the variation of lithium-ion concentration in the electrolyte. Table 1-1 shows the governing equation for an isothermal SPM model. The isothermal model can easily be modified to include an energy balance in a lumped form, to account for the temperature change inside the battery.

Table 1-1: Governing equations for the SPM

	Governing equation	Boundary conditions	
Solid phase concentration (cathode): $c_p^s(r,t)$	$\frac{\partial c_p^s}{\partial t} = \frac{1}{r^2}\frac{\partial}{\partial r}\left[r^2 D_p^s \frac{\partial c_p^s}{\partial r} \right]$	$\left.\frac{\partial c_p^s}{\partial r}\right\|_{r=0} = 0,\ -D_p^s \left.\frac{\partial c_p^s}{\partial r}\right\|_{R_p} = \frac{I_{\text{overall}}}{a_p F}$	(1.1)
Solid phase concentration (anode): $c_n^s(r,t)$	$\frac{\partial c_n^s}{\partial t} = \frac{1}{r^2}\frac{\partial}{\partial r}\left[r^2 D_n^s \frac{\partial c_n^s}{\partial r} \right]$	$\left.\frac{\partial c_n^s}{\partial r}\right\|_{r=0} = 0,\ -D_n^s \left.\frac{\partial c_n^s}{\partial r}\right\|_{R_n} = \frac{-I_{\text{overall}}}{a_n F}$	(1.2)
Voltage $V(t)$:	$V(t) = \phi_p^s(t) - \phi_n^s(t)$		(1.3)

1.5.2 Pseudo Two-Dimensional Model

Pseudo two-dimensional (P2D) model is one of the most widely used model for lithium-ion batteries. It is a macro-homogeneous model based on the fundamentals of concentrated-solution theory, and is derived by a volume-averaging of solid and electrolyte phase at a particular location inside the battery. Instead of a single particle as in SPM, the P2D model considers a continuous collection of solid particles across the spatial domain of the electrode, and assumes the intercalation and deintercalation of the lithium-particle inside the solid particle, to follow a Fickian diffusion. It also considers the variation of lithium-ion concentration as well as potential distribution in the electrolyte phase. The pore-wall flux at the surface of the particle is given by flux of the charge transfer reaction taking place at the solid-electrolyte interface. The charge transfer at the interface is assumed to follow a Butler-Volmer type kinetics. Similar to the SPM, a lumped energy balance can be used to describe the temperature change inside the cell. Table 1-2 shows the governing equations for the P2D thermal model.

Table 1-2: Governing equations for the P2D model

Governing Equations	Boundary Conditions	
Positive Electrode		
$\varepsilon_{\mathrm{p}} \dfrac{\partial c}{\partial t} = \dfrac{\partial}{\partial x}\left[D_{\mathrm{eff,p}} \dfrac{\partial c}{\partial x} \right] + a_{\mathrm{p}} \left(1 - t_{+}\right) j_{\mathrm{p}}$	$\left.\dfrac{\partial c}{\partial x}\right\|_{x=0} = 0\ ,\ -D_{\mathrm{eff,p}} \left.\dfrac{\partial c}{\partial x}\right\|_{x=l_p^-} = -D_{\mathrm{eff,s}} \left.\dfrac{\partial c}{\partial x}\right\|_{x=l_p^+}$	(1.4)
$-\sigma_{eff,p} \dfrac{\partial \Phi_1}{\partial x}$ $-\kappa_{\mathrm{eff,p}} \dfrac{\partial \Phi_2}{\partial x} + \dfrac{2\kappa_{\mathrm{eff,p}} RT}{F}\left(1 - t_{+}\right) \dfrac{\partial \ln c}{\partial x} = I$	$\left.\dfrac{\partial \Phi_2}{\partial x}\right\|_{x=0} = 0,$ $\kappa_{\mathrm{eff,p}} \left.\dfrac{\partial \Phi_2}{\partial x}\right\|_{x=l_p^-} = \kappa_{\mathrm{eff,s}} \left.\dfrac{\partial \Phi_2}{\partial x}\right\|_{x=l_p^+}$	(1.5)
$\dfrac{\partial}{\partial x}\left[\sigma_{\mathrm{eff,p}} \dfrac{\partial \Phi_1}{\partial x} \right] = a_{\mathrm{p}} F j_{\mathrm{p}}$	$\sigma_{eff,p} \left.\dfrac{\partial \Phi_1}{\partial x}\right\|_{x=0} = -I,\ \left.\dfrac{\partial \Phi_1}{\partial x}\right\|_{x=l_p^-} = 0$	(1.6)

$\frac{\partial c_p^s}{\partial t} = \frac{1}{r^2}\frac{\partial}{\partial r}\left[r^2 D_p^s \frac{\partial c_p^s}{\partial r} \right]$	$\left.\frac{\partial c_p^s}{\partial r}\right\|_{r=0} = 0,\ D_p^s \left.\frac{\partial c_p^s}{\partial r}\right\|_{r=R_P} = -j_p$	(1.7)
Separator		
$\varepsilon_s \frac{\partial c}{\partial t} = \frac{\partial}{\partial x}\left[D_{\text{eff,s}} \frac{\partial c}{\partial x} \right]$	$c\|_{x=l_p^-} = c\|_{x=l_p^+},\ c\|_{x=l_p+l_s^-} = c\|_{x=l_p+l_s^+}$	(1.8)
$-\kappa_{\text{eff,s}} \frac{\partial \Phi_2}{\partial x} + \frac{2\kappa_{\text{eff,s}} RT}{F}(1-t_+)\frac{\partial \ln c}{\partial x} = I$	$\Phi_2\|_{x=l_p^-} = \Phi_2\|_{x=l_p^+}$ $\Phi_2\|_{x=l_p+l_s^-} = \Phi_2\|_{x=l_p+l_s^+}$	(1.9)
Negative Electrode		
$\varepsilon_n \frac{\partial c}{\partial t} = \frac{\partial}{\partial x}\left[D_{\text{eff,n}} \frac{\partial c}{\partial x} \right] + a_n (1-t_+) j_n$	$\left.\frac{\partial c}{\partial x}\right\|_{x=l_p+l_s+l_n} = 0$ $-D_{\text{eff,s}} \left.\frac{\partial c}{\partial x}\right\|_{x=l_p+l_s^-} = -D_{\text{eff,n}} \left.\frac{\partial c}{\partial x}\right\|_{x=l_p+l_s^+}$	(1.10)
$-\sigma_{\text{eff,n}} \frac{\partial \Phi_1}{\partial x}$ $-\kappa_{\text{eff,n}} \frac{\partial \Phi_2}{\partial x} + \frac{2\kappa_{\text{eff,n}} RT}{F}(1-t_+)\frac{\partial \ln c}{\partial x} = I$	$-\kappa_{\text{eff,s}} \left.\frac{\partial \Phi_2}{\partial x}\right\|_{x=l_p+l_s^-} = -\kappa_{\text{eff,p}} \left.\frac{\partial \Phi_2}{\partial x}\right\|_{x=l_p+l_s^+}$ $\Phi_2\|_{x=l_p+l_s+l_n} = 0$	(1.11)
$\frac{\partial}{\partial x}\left[\sigma_{\text{eff,n}} \frac{\partial \Phi_1}{\partial x} \right] = a_n F j_n$	$\left.\frac{\partial \Phi_1}{\partial x}\right\|_{x=l_p+l_s^+} = 0, \sigma_{eff,n} \left.\frac{\partial \Phi_1}{\partial x}\right\|_{x=l_p+l_s+l_n} = -I$	(1.12)
$\frac{\partial c_n^s}{\partial t} = \frac{1}{r^2}\frac{\partial}{\partial r}\left[r^2 D_n^s \frac{\partial c_n^s}{\partial r} \right]$	$\left.\frac{\partial c_n^s}{\partial r}\right\|_{r=0} = 0,\ D_n^s \left.\frac{\partial c_n^s}{\partial r}\right\|_{r=R_P} = -j_n$	(1.13)
$\rho_n C_{p,n} \frac{dT_n}{dt} = \frac{1}{l_n}\frac{\partial}{\partial X}\left[\frac{\lambda_n}{l_n}\frac{\partial T_n}{\partial X} \right] + Q_{\text{rxn,n}} + Q_{\text{rev,n}} + Q_{\text{ohm,n}}$	$\frac{\lambda_s}{l_s}\left.\frac{\partial T_s}{\partial X}\right\|_{X=1} = -\frac{\lambda_n}{l_n}\left.\frac{\partial T_n}{\partial X}\right\|_{X=0}$ $-Keff_n \left.\frac{\partial T_n}{\partial X}\right\|_{X=1} = h_{env}\left(T_{air} - T_n\|_{X=1}\right)$	(1.14)

Table 1-3: Additional equations required for the P2D model

$j_p = 2k_p c^{0.5} c_p^s\|_{r=R_P}{}^{0.5} \left(c_{\max,p}^s - c_p^s\|_{r=R_P} \right)^{0.5} \sinh\left[\frac{F}{2RT}\left(\Phi_1 - \Phi_2 - U_p \right) \right]$	(1.15)
$j_n = 2k_n c^{0.5} c_n^s\|_{r=R_P}{}^{0.5} \left(c_{\max,n}^s - c_n^s\|_{r=R_P} \right)^{0.5} \sinh\left[\frac{F}{2RT}\left(\Phi_1 - \Phi_2 - U_n \right) \right]$	(1.16)

$\kappa_{eff,i} = \varepsilon_i^{brugg_i} \times 10^{-4} c \left(\begin{array}{l} -10.5 + 0.074T - 6.96\times10^{-5}T^2 + 6.68\times10^{-4}c - \\ 1.78\times10^{-5}cT + 2.8\times10^{-8}cT^2 + 4.94\times10^{-7}c^2 \\ -8.86\times10^{-10}Tc^2 \end{array} \right)^2$ $, i = p, s, n$	(1.17)
$\sigma_{eff,i} = \sigma_i \left(1 - \varepsilon_i - \varepsilon_{f,i}\right), i = p, s, n$	(1.18)
$D_{eff,i} = D\varepsilon_i^{brugg_i}, i = p, s, n$ $D = 2.33\times10^{-4} \times 10^{-4.43 - \frac{54}{\left(T - 5\times10^{-3}c - 229\right)} - 2.2\times10^{-4}c}$	(1.19)
$a_i = \frac{3}{R_i}\left(1 - \varepsilon_i - \varepsilon_{f,i}\right), i = p, s, n$	(1.20)
$U_{p,ref} = \frac{-4.656 + 88.669\theta_p^{\,2} - 401.119\theta_p^{\,4} + 342.909\theta_p^{\,6} - 462.471\theta_p^{\,8} + 433.434\theta_p^{\,10}}{-1.0 + 18.933\theta_p^{\,2} - 79.532\theta_p^{\,4} + 37.311\theta_p^{\,6} - 73.083\theta_p^{\,8} + 95.96\theta_p^{\,10}}$ $\theta_p = \frac{c_n^s\big\vert_{r=R_P}}{c_{p,\max}^s}; 0.4955 \le \theta_p \le 0.99$	(1.21)
$U_{n,ref} = -0.057 + 0.53\mathrm{e}^{-57\theta} - 0.184\tanh\left(20.0\theta - 21.0\right)$ $- 0.012\tanh\left(7.57\theta - 4.431\right) - 0.0304\tanh\left(18.518\theta - 3.24\right)$ $- 0.01\tanh\left(0.255\theta - 0.02653\right)$ $\theta_n = \frac{c_p^s\big\vert_{r=R_P}}{c_{n,\max}^s};\ 0.01 \le \theta_n \le 0.99$	(1.22)
$D_i^s = D_{i,ref}^s \exp\left(-\frac{E_a^{D_i^s}}{R}\left(\frac{1}{T} - \frac{1}{T_{ref}}\right)\right),\ i = p, n$	(1.23)
$k_i = k_{i,ref} \exp\left(-\frac{E_a^{k_i}}{R}\left(\frac{1}{T} - \frac{1}{T_{ref}}\right)\right),\ i = p, n$	(1.24)
$Q_{\mathrm{rxn},i} = Fa_i j_i \left(\Phi_{1,i} - \Phi_{2,i} - U_i\right), i = p, n$	(1.25)
$Q_{\mathrm{rev},i} = Fa_i j_i T_i \frac{\partial U_i}{\partial T}, i = p, n$	(1.26)

$Q_{\text{ohm},i} = \sigma_{\text{eff},i}\left(\frac{1}{l_i}\frac{\partial\Phi_{1,i}}{\partial X}\right)^2 + \kappa_{\text{eff},i}\left(\frac{1}{l_i}\frac{\partial\Phi_{2,i}}{\partial X}\right)^2 + \frac{2\kappa_{\text{eff},i}RT_i}{F}\left(1-t_+^0\right)\frac{1}{l_i^2}\frac{1}{c_i}\frac{\partial c_i}{\partial X}\frac{\partial\Phi_{2,i}}{\partial X}, i = p,n$	(1.27)
$Q_{\text{ohm,s}} = \kappa_{\text{eff},s}\left(\frac{1}{l_s}\frac{\partial\Phi_{2,s}}{\partial x}\right)^2 + \frac{2\kappa_{\text{eff},s}RT_s}{F}\left(1-t_+^0\right)\frac{1}{c_s}\frac{1}{l_s^2}\frac{\partial c_s}{\partial X}\frac{\partial\Phi_{2,i}}{\partial X}$	(1.28)
$U_i\left(T_i,\theta_i\right) = U_{i,\text{ref}}\left(T_{\text{ref}},\theta_i\right) + \left(T_i - T_{\text{ref}}\right)\left[\frac{dU_i}{dT}\right]_{T_{\text{ref}}}, i = p,n$	(1.29)

The assumption of the lithium particle intercalating inside the electrode material has been widely debated, and the exact intercalating entity might be different for different materials. Various mechanisms and models have been proposed to account for the transport in the solid phase. The assumption of the charge-transfer reaction at the interface following a Butler-Volmer type of kinetics has also been challenged. However, the P2D model provides a very general framework for modeling the processes inside a lithium-ion cell, and different mechanisms for charge transfer or transport in various phases can easily be integrated into the existing framework. Materials involving phase change (such as $LiFePO_4$) needs a slightly different treatment. In addition to this, P2D model also allows adding various models for capacity fade depending on the electrode materials.

The usable capacity of any lithium-ion battery decreases as the battery is used in any application. While the capacity fade occurs because of a variety of issues, below we review some of the reasons believed to be responsible for causing majority of the capacity fade.

1.6. Reasons for capacity fade

Lithium plating: The lithium plating side reaction is one the most dangerous mechanisms for capacity fade, and can cause severe safety issues. Because of structural changes or other reasons, lithium-ion traveling from the electrolyte might get deposited at the surface of the anode instead of intercalating inside the particle. As the battery cycles, repeated deposition at the particle surface can lead to dendrite formation. As the dendrites grow in size, there remains a risk of them puncturing through the separator, and internally short-circuiting the battery. This could lead to high temperature rise and a potential thermal runaway, which could potentially result in disastrous consequences. The plating side reaction primarily occurs at low operating temperatures and high charge rates. A negative overpotential at the anode favors the plating side reaction, and the separator-anode interface is most prone to plating.

SEI layer formation: In the operating potential window for a lithium-ion battery, the typical organic electrolytes (ethyl carbonate/dimethyl carbonate) used react with the active material to form a passivating layer called as the solid-electrolyte interface (SEI) layer at the solid-electrolyte interface. An optimum SEI growth during the first few cycles (also called as formation cycles) is essential to an efficient use of a battery. Hence, most battery manufacturers typically control the charging/discharging of the battery in the first few cycles to get the desired SEI properties. The growth of the SEI layer restricts further solvent diffusion to the electrode active material, and becomes self-limiting. SEI layer growth is proportional to the charge rates and temperature inside a cell.

Various models have been proposed to model the formation of SEI layer, and its growth as the battery cycles.[10-13] While the exact composition of SEI layer consists of various organic lithium salts, most models account for the product of the SEI layer side reaction in a lumped form. For most battery chemistries, SEI layer side reaction dominates the capacity fade mechanism.

Intercalation-induced stress effects: For the electrodes with intercalation-based chemistry, the lithium particle gets inserted into the interstitial space of the host material. The insertion of the additional lithium changes the local spacing of the lattice structure, causing it to expand. The volume expansion for certain host materials (such as silicon-based anodes) can be extremely significant. Concentration gradients inside the particle lead to radial and tangential stresses inside the particle. Development of significant stresses inside the particle can lead to fracture of the particles which reduce the effective storage capacity of the electrode and can also reduce the internal connectivity of the particles. Both of these reasons ultimately lead to the capacity fade of the battery. Models of varying complexity have been proposed to account for the volume expansion of the particles, as well as to model the capacity fade occurring inside the battery because of the intercalation-induced radial and tangential stresses.

In addition to the above-mentioned causes, various other factors depending on the operating window of the battery could lead to capacity fade. Overcharge or overdischarge can lead to electrolyte reduction or oxidation (depending on the operating voltage) which can cause significant damage to the health of the battery. A battery management system becomes critical to avoiding the operation of the battery in such windows.

While the physics-based models provide more insight inside the battery, most of these models are also highly non-linear in nature, which adds significant challenges to implement control strategies to mitigate the above-mentioned issues. Various issues, such as the onset of dynamics of some internal states only during use of batteries at high charge/discharge rates, and several other states which are active only while charging or discharging, adds to the challenges of the observability of these physics-based electrochemical models. Hence, various approximated and reduced order models have been proposed in the past, to make the models strongly observable in local intervals.[14-

[18] Mathematical reformulation is one way to ensure the fidelity of the original model while significantly reducing the computational cost. Most of these reformulation techniques employ spectral methods (such as orthogonal collocation) where different degree of accuracy can be obtained based on the choice of the trial function, or the number of internal collocation points used in a specific region (cathode/separator/anode).

1.7. Scope of the dissertation

The work presented in this dissertation mainly contains various strategies to obtain optimal control profiles based upon previously developed reformulated pseudo-2 dimensional models. Past researchers have shown multivariable control techniques like Dynamic Matrix Control (DMC)[19], Internal Model Control (IMC)[20], and Model Predictive Heuristic Control (MPHC)[21] for a variety of systems. However, these approaches suffer from their reliability on the linear approximations of the experimentally obtained step-response data and do not consider the full nonlinear model directly and explicitly. Chapter 2 presents a control strategy called *Generic Model Control* (GMC) to arrive at optimal control profiles, using a set-point strategy for measured (state) variables. Application of GMC requires robust and efficient DAE solvers. By combining GMC approach with robust DAE solvers, we show the ability to reformulate some of the common control and optimization problems for batteries as direct simulation problems. By rewriting charging and optimization objective as set-point control problems, we derive optimal profiles using the GMC approach. The advantages and limitations of this approach, along with its comparison with other traditional control approaches are discussed in detail.

Chapter 3 discusses the simultaneous discretization, and control-vector parameterization strategies to derive optimal charging profiles for minimizing capacity fade in Lithium ion batteries using

P2D model. While several papers have been published for estimating optimal model-based control strategies for various objectives, none of the past papers have validated the control strategies in a detailed experimental study. In Chapter 3, we also present the experimental validation and results obtained after implementing optimal charging profiles on a 16Ah NMC-based pouch cell. Model-based control algorithms were derived in a university environment, and laboratory testing was performed at the National Renewables Energy Laboratory (NREL).To the best of our knowledge, this study is the first to experimentally demonstrate that the improved extra knowledge obtained by sophisticated physics-based models results in significant improvements in battery performance.

In order to perform robust optimal control, the choice of the discretization scheme in the temporal domain is also crucial. Chapter 4 provides a method to improve the order of accuracy in the simultaneous formulation for optimal control. In particular, a second derivative method (SDM) is developed and presented.

Chapter 5 presents a method and the code developed for linear impedance simulations for the P2D model. A collocation approach in the spatial direction is used to solve for the dependent variables. The resulting code is extremely fast and robust, can be used for parameter estimation purposes. Chapter 6 summarizes the dissertation, and presents the future direction for a physics-model based battery management system.

Chapter 2: An Alternate Control Strategy for Lithium-Ion Batteries

2.1. Why do we need alternate control strategies?

Several researchers have been working to design optimal charging profiles for batteries by implementing a wide range of control strategies. Methekar *et al.*[22] derived optimal charging profiles for maximizing the energy using the Control Vector Parameterization (CVP) approach. Rahimian *et al.*[23] calculated the charging current to minimize the capacity fade vs. cycle number using a single particle model (SPM). Perez *et al.*[24] obtained optimal charging profiles for batteries with constraints on temperature as well as concentration of lithium in solid and electrolyte phase. Suthar *et al.*[25] proposed optimal charging profiles for minimizing the intercalation induced stresses inside particle using simultaneous discretization approach. Hoke *et al.*[26] proposed a method to minimize the cost of battery charging in markets with variable electricity costs after accounting for battery degradation. Methekar *et al.*[22] derived optimal charging profiles for maximizing the energy using the Control Vector Parameterization (CVP) approach. Rahimian *et al.*[23] calculated the charging current to minimize the capacity fade vs. cycle number using a single particle model (SPM). Perez *et al.*[24] obtained optimal charging profiles for batteries with constraints on temperature as well as concentration of lithium in solid and electrolyte phase. Suthar *et al.*[25] proposed optimal charging profiles for minimizing the intercalation induced stresses inside particle using simultaneous discretization approach. Hoke *et al.*[26] proposed a method to minimize the cost of battery charging in markets with variable electricity costs after accounting for battery degradation. However, all of these methods require nonlinear and robust optimization approaches.

Here, we present an alternative approach to control batteries, applying the method of *Generic Model Control* (GMC)[27], also known as *Reference System Synthesis*.[28] This approach is based on a set-point strategy for the measured (state) variable. GMC has previously been implemented on various applications such as multistage flash desalination[29], distillation column control[30-32], control of nutrients – removing activated sludge systems[33], armature current control of DC motor[34], etc. In this article, we apply the GMC technique to physics-based battery models. Lee and Sullivan[27] originally proposed the GMC algorithm for ordinary differential equations (ODEs) and for problems in which the measured variable is not explicitly dependent on the manipulated variable. Here, we extend the GMC technique to differential algebraic equations (DAEs) with set points for algebraic variables, and for problems in which the output is directly dependent on control, for applying it to battery models. While the theoretical internal stability for the GMC approach is yet to be proven unlike nonlinear model predictive control approaches[35], in our experience, the GMC approach is computationally competitive as it avoids the need for optimization for unconstrained problems, and for problems with bounds on the manipulated variable. The gain in CPU time is obtained only if efficient and robust DAE solvers are used.

In subsequent sections, we discuss the theory behind the GMC framework, followed by case studies for applying GMC control formulation for a thin film nickel hydroxide electrode, a single particle model, along with discussing various objectives for a physics-based Li-ion battery model. For the physics-based Li-ion battery model, the first case demonstrates the implementation and the problem formulation for obtaining a current profile for a set-point given on the charge stored in the battery. The second case considers a set-point of 4.2V for voltage of the cell, without any bounds on the applied current, followed by current containing bounds.

2.2. Introduction to Generic Model Control

The generic model control (GMC) strategy is based on finding values for the manipulated variable that forces the controlled (measured) variable to reach its set-point in a non-linear process model. The desired set-point and its measured variable is compared to generate the error. The obtained error is used in GMC architecture to generate control input for the system (process dynamics) to direct the controlled variable towards the desired set-point.

The strategy for implementing generic model control is described as follows. Consider a dynamic process model given by a set of differential equations:

$$\frac{dx}{dt} = f(x,u,t) \tag{2.1}$$

Where x is the vector of state variables of dimension *n*, u is the scalar process input (also called as manipulated variable) of dimension *m*, t is the time. The relation for output variables is given by:

$$Y = M(x,u) \tag{2.2}$$

where *Y* is a vector of output variables (measured variables) of dimension *p*.

To obtain control law from above equations (2.1) and (2.2), a reference trajectory proposed by Lee and Sullivan[27] is given as,

$$\left(\frac{dY}{dt}\right) = K(Y^{set} - Y) + \frac{K}{\tau_i}\int_0^t \left(Y^{set} - Y\right) d\tau \tag{2.3}$$

Where Y^{set} is the desired set-point, K and τ_i are the tuning parameters. The first term of the right hand side of equation (2.3) is the rate of change of Y moving towards the desired set-point Y^{set}, and can be referred to as the *Proportional* term. The second term is added to minimize the offset

between the actual value and the desired set-point, and can be referred to as the *Integral* term. Using equation (2.3), a generic control law is obtained for GMC, which is given as,

$$\frac{dY}{dt} - K\left(Y^{set} - Y\right) - \frac{K}{\tau_i}\int_0^t \left(Y^{set} - Y\right) d\tau = 0 \tag{2.4}$$

The term $\left(\frac{dY}{dt}\right)$ is the reference trajectory that can be obtained using equations (2.1) and (2.5).

$$\left(\frac{dY}{dt}\right) = \frac{\partial M}{\partial x} f\left(x,u,t\right) + \frac{\partial M}{\partial u} \cdot \frac{du}{dt} \tag{2.5}$$

Combining equations (2.4) and (2.5) gives the control law of GMC in terms of the process model and the reference trajectory.

$$\frac{\partial M}{\partial x} f\left(x,u,t\right) + \frac{\partial M}{\partial u}\frac{du}{dt} - K\left(Y^{set} - Y\right) - \frac{K}{\tau_i}\int_0^t \left(Y^{set} - Y\right) d\tau = 0 \tag{2.6}$$

Most physics-based battery models are given by partial differential equations (PDEs), which are converted to DAEs for simulation or optimization. Often times, the output or the measured variable is a direct function of the manipulated variable. Below, we discuss an approach to apply GMC for DAEs, including cases for which set point is given for an algebraic variable.

Consider an index-1DAE system governing two scalars *y* and *z* given by:

$$\frac{dy}{dt} = f\left(y,z,u\right) \tag{2.7}$$

$$g(y,z,u) = 0 \tag{2.8}$$

Where, *y* is the differential variable, *z* is the algebraic variable and *u* is the manipulated variable. If the controlled (measured) variable is y, then equations (2.4) and (2.6) can be used directly, as the derivative is explicitly available from the model equations. If the measured variable is *z* (for example potential as in the case of batteries), then the derivative $\left(\frac{dz}{dt}\right)$ is not available directly

from the model equations. The derivative $\left(\frac{dz}{dt}\right)$ in such cases, can be obtained by differentiating equation (2.8) with time to get:

$$\frac{dg}{dt} = \frac{\partial g}{\partial y}(y,z,u)\cdot f(y,z,u) + \frac{\partial g}{\partial z}(y,z,u)\cdot\frac{dz}{dt} + \frac{\partial g}{\partial u}(y,z,u)\cdot\frac{du}{dt} = 0 \tag{2.9}$$

GMC equation for this case is given by:

$$\left(\frac{dz}{dt}\right) = K(z^{set} - z) + \frac{K}{\tau_i}\int_0^t \left(z^{set} - z\right)d\tau \tag{2.10}$$

Equation (2.10) can now be substituted in equation (2.9) to get:

$$\frac{dg}{dt} = \frac{\partial g}{\partial y}(y,z,u)\cdot f(y,z,u) + \frac{\partial g}{\partial z}(y,z,u)\cdot\left[K(z^{set} - z) + \frac{K}{\tau_i}\int_0^t \left(z^{set} - z\right)d\tau\right] + \frac{\partial g}{\partial u}(y,z,u)\cdot\frac{du}{dt} = 0 \tag{2.11}$$

In this case, equation (2.7) governs the dynamics of the variable *y*, while variables *z* and *u* are governed by equations (2.8) and (2.11) respectively. Even though a $\frac{du}{dt}$ term appears in (2.11), since the experimental value of *z* is known initially at time *t* = 0, the initial condition for *u* can be calculated using (2.8). The final form of the equations to be solved for obtaining the control profile is summarized in (2.12) as:

$$\left.\begin{aligned}
&\frac{dy}{dt} = f(y,z,u) && \text{(a)}\\
&g(y,z,u) = 0 && \text{(b)}\\
&\frac{dg}{dt} = \frac{\partial g}{\partial y}(y,z,u)\cdot f(y,z,u) + \frac{\partial g}{\partial z}(y,z,u)\cdot\left[K(z^{set} - z) + \frac{K}{\tau_i}\int_0^t \left(z^{set} - z\right)d\tau\right] + \\
&\quad \frac{\partial g}{\partial u}(y,z,u)\cdot\frac{du}{dt} = 0 && \text{(c)}
\end{aligned}\right\} \tag{2.12}$$

2.3. Generic Model Control for Battery Models

In this section, we discuss the performance of generic model control strategy for different types of battery models.

2.3.1 Thin film nickel hydroxide electrode

Consider the DAE model describing a galvanostatic charge of a thin-film nickel hydroxide electrode as described by Wu *et al.*[36] The model equations are given by:

$$\frac{dy_1}{dt} = \frac{j_1 \cdot W}{F \rho V} \tag{2.13}$$

$$j_1 + j_2 = I_{app} \tag{2.14}$$

$$\frac{dQ}{dt} = I_{app} \tag{2.15}$$

$$j_1 = i_{0,1}\left[2(1-y_1)\exp\left(\frac{(\phi_1 - \phi_{01})F}{2RT} \right) - 2y_1 \exp\left(-\frac{(\phi_1 - \phi_{01})F}{2RT} \right) \right] \tag{2.16}$$

$$j_2 = i_{0,2}\left[\exp\left(\frac{(\phi_1 - \phi_{02})F}{RT} \right) - \exp\left(-\frac{(\phi_1 - \phi_{02})F}{RT} \right) \right] \tag{2.17}$$

Where y_1 is the mole fraction of nickel hydroxide, ϕ_1 represents the potential difference at the solid-liquid interface and Q is the total charge stored in the battery. I_{app} represents the applied current and is the manipulated variable for this model. The initial condition of all the variables is $y_1(0) = 0.05$, $\phi_1(0) = 0.350236$, $Q(0) = 0$ and $I_{app}(0) = 1 \times 10^{-5}$. The parameters for this model are given in Table 2-1.

Table 2-1: List of parameters for the thin-film nickel hydroxide model

Symbol	Parameter	Value	Units
F	Faraday constant	96,487	C/mol
R	Gas constant	8.314	J/(mol K)
T	Temperature	303.15	K

ϕ_{01}	Equilibrium potential	0.420	V
ϕ_{02}	Equilibrium potential	0.303	V
W	Mass of active material	92.7	g
V	Volume	1×10^{-5}	m^3
i_{01}	Exchange current density	1×10^{-4}	A/cm^3
i_{02}	Exchange current density	1×10^{-10}	A/cm^3
P	Density	3.4	g/cm^3

For this model, three different objectives are studied as discussed below.

a) In the first objective, we solve the model for mole-fraction $\left(y_1\right)$ to reach its desired set point $\left(y_1^{set}\right)$. Even though this model is a DAE, the equation for the total derivative of the measured variable $\left(\frac{dy_1}{dt}\right)$ is directly available from the model (equation (2.13)). This can be compared with equation (2.2) to realize $Y = y_1$.

The GMC formulation for this case is given by:

$$\frac{dy_1}{dt} = \frac{j_1 \cdot W}{F \rho V} \tag{2.18}$$

$$\frac{dy_1}{dt} = K \cdot \left(y_1^{set} - y_1(t)\right) + \frac{K}{\tau_i} r(t) \tag{2.19}$$

where $r(t)$ represents the integral of the offset and is defined in equation (2.20) as

$$\frac{dr}{dt} = \left(y_1^{set} - y_1(t)\right) \tag{2.20}$$

From equations (2.18) and (2.19), the following relation can be derived:

$$\frac{j_1 W}{F\rho V} = K\left(y_1^{set} - y_1(t)\right) + \frac{K}{\tau_i} r(t) \tag{2.21}$$

Further, equation (2.14) can be used to get:

$$\frac{\left(I_{app} - j_2\right)W}{F\rho V} = K\left(y_1^{set} - y_1(t)\right) + \frac{K}{\tau_i} r(t) \tag{2.22}$$

Using equation (2.22), an explicit relation for I_{app} can be written as,

$$I_{app} = \frac{F\rho V}{W}\left(K\left(y_1^{set} - y_1(t)\right) + \frac{K}{\tau_i} r(t)\right) + j_2 \tag{2.23}$$

Equations (2.13) – (2.17) along with (2.23) are solved simultaneously to get the GMC control profile. The final set of equations (GMC model) to be solved for this case are summarized again in (2.24).

$$\left.\begin{aligned}
&\frac{dy_1}{dt} = \frac{j_1 \cdot W}{F\rho V} && \text{(a)}\\
&j_1 + j_2 = I_{app} && \text{(b)}\\
&\frac{dQ}{dt} = I_{app} && \text{(c)}\\
&\frac{dr}{dt} = \left(y_1^{set} - y_1(t)\right) && \text{(d)}\\
&I_{app} = \frac{F\rho V}{W}\left(K\left(y_1^{set} - y_1(t)\right) + \frac{K}{\tau_i} r(t)\right) + j_2 && \text{(e)}\\
&j_1 = i_{0,1}\left[2\left(1 - y_1\right)\exp\left(\frac{\left(\phi_1 - \phi_{01}\right)F}{2RT}\right) - 2y_1\exp\left(-\frac{\left(\phi_1 - \phi_{01}\right)F}{2RT}\right)\right] && \text{(f)}\\
&j_2 = i_{0,2}\left[\exp\left(\frac{\left(\phi_1 - \phi_{02}\right)F}{RT}\right) - \exp\left(-\frac{\left(\phi_1 - \phi_{02}\right)F}{RT}\right)\right] && \text{(g)}
\end{aligned}\right\} \tag{2.24}$$

It should be noted that the manipulated variable $\left(I_{app}\right)$ is governed by equation (2.24)(e), whereas equation (2.24)(a), (b) and (c) govern y_1, ϕ_1 and Q respectively. The initial condition for $r(t)$ is assumed to be zero, the proportionality constant *K* is taken to be 0.02, and τ_i is assumed to be 3500. Figure 2-1(a) shows the profiles for mole fraction $\left(y_1\right)$ for various set-points of $y_1^{set} = [0.5, 0.6, 0.7]$. Figure 2-1(b) shows the profiles of manipulated variable $\left(I_{app}\right)$ that directs mole fraction $\left(y_1\right)$ to reach its desired set-point. An upper bound of 120 μA/cm^2 is used for this case. The strategy to implement bounded currents is explained in detail in the next example.

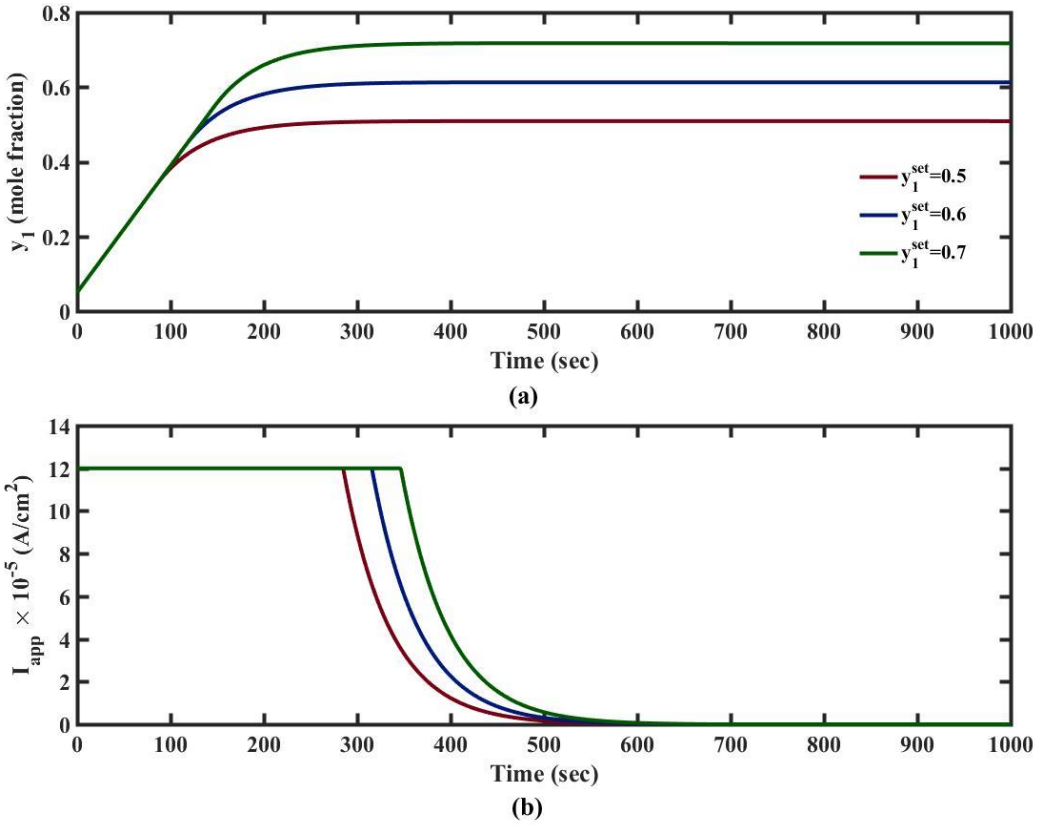

Figure 2-1: Profiles of (a) Mole fraction (y_1) and (b) Applied current (I_{app}) with time for the Wu and White model

b) In the second case, the same DAE model is solved for total charged stored $\left(Q\right)$ to reach its desired set point $\left(Q^{set}\right)$. This case is similar to the case (a) discussed above. Equation (2.15) can be used to get the explicit derivative of the measured variable *Q*. Hence, for this case:

$$Y = Q$$

The GMC formulation is given by the following set of models,

$$\frac{dQ}{dt} = K\left(Q^{set} - Q\left(t\right)\right) + \frac{K}{\tau_i} r(t) \tag{2.25}$$

$$\frac{dr}{dt} = \left(Q^{set} - Q(t)\right) \tag{2.26}$$

From equations (2.15) and (2.25), we can get:

$$I_{app}(t) = K\left(Q^{set} - Q(t)\right) + \frac{K \cdot r(t)}{\tau_i} \tag{2.27}$$

If there are no bounds on current, the final set of equations to be solved for this case is given as follows:

$$\left.\begin{aligned}
&\frac{dy_1}{dt} = \frac{j_1 \cdot W}{F \rho V} && \text{(a)}\\
&j_1 + j_2 = I_{app} && \text{(b)}\\
&\frac{dQ}{dt} = I_{app} && \text{(c)}\\
&\frac{dr}{dt} = \left(Q^{set} - Q(t)\right) && \text{(d)}\\
&I_{app} = K\left(Q^{set} - Q(t)\right) + \frac{K}{\tau_i} r(t) && \text{(e)}\\
&j_1 = i_{0,1}\left[2(1-y_1)\exp\left(\frac{(\phi_1 - \phi_{01})F}{2RT}\right) - 2y_1 \exp\left(-\frac{(\phi_1 - \phi_{01})F}{2RT}\right)\right] && \text{(f)}\\
&j_2 = i_{0,2}\left[\exp\left(\frac{(\phi_1 - \phi_{02})F}{RT}\right) - \exp\left(-\frac{(\phi_1 - \phi_{02})F}{RT}\right)\right] && \text{(g)}
\end{aligned}\right\} \tag{2.28}$$

The controller parameters for this case are K = 0.1 and τ_i = 20, and the initial condition for $r(t)$ is taken to be zero. Different set points for charge stored are tried for this case.

In case if there are bounds on the applied current, it is bounded by applying upper and lower limits using relation given in equation (2.27). Here, we assume a lower bound of zero, and an upper bound of 120 μA/cm^2. Such a case can be solved by introducing a dummy variable $\left(I_1(t)\right)$, that

represents the applied current in the GMC equation (e), and the bounds are then applied on the current variable $\left(I_1(t)\right)$ as shown in equation (2.29).

$$I_{app}(t) = \min\left(12\times10^{-5}, \max\left(0, I_1(t)\right)\right) \tag{2.29}$$

For the bounded case, the final equations to be solved are summarized below.

$$\left.\begin{aligned}
&\frac{dy_1}{dt} = \frac{j_1 \cdot W}{F\rho V} && (\text{a})\\
&j_1 + j_2 = I_{app} && (\text{b})\\
&\frac{dQ}{dt} = I_{app} && (\text{c})\\
&\frac{dr}{dt} = \left(Q^{set} - Q(t)\right) && (\text{d})\\
&I_1 = K\left(Q^{set} - Q(t)\right) + \frac{K}{\tau_i} r(t) && (\text{e})\\
&I_{app} = \min\left(12\times10^{-5}, \max\left(0, I_1\right)\right) && (\text{f})\\
&j_1 = i_{0,1}\left[2\left(1-y_1\right)\exp\left(\frac{\left(\phi_1-\phi_{01}\right)F}{2RT}\right) - 2y_1\exp\left(-\frac{\left(\phi_1-\phi_{01}\right)F}{2RT}\right)\right] && (\text{g})\\
&j_2 = i_{0,2}\left[\exp\left(\frac{\left(\phi_1-\phi_{02}\right)F}{RT}\right) - \exp\left(-\frac{\left(\phi_1-\phi_{02}\right)F}{RT}\right)\right] && (\text{h})
\end{aligned}\right\} \tag{2.30}$$

Figure 2-2(a) shows the profiles for charge stored with time for various set points of $Q^{set} = [0.15, 0.2, 0.3]$ and Figure 2-2(b) shows the corresponding control profile for current for different set points. It can be seen that the charge stored reaches its set point in all the cases.

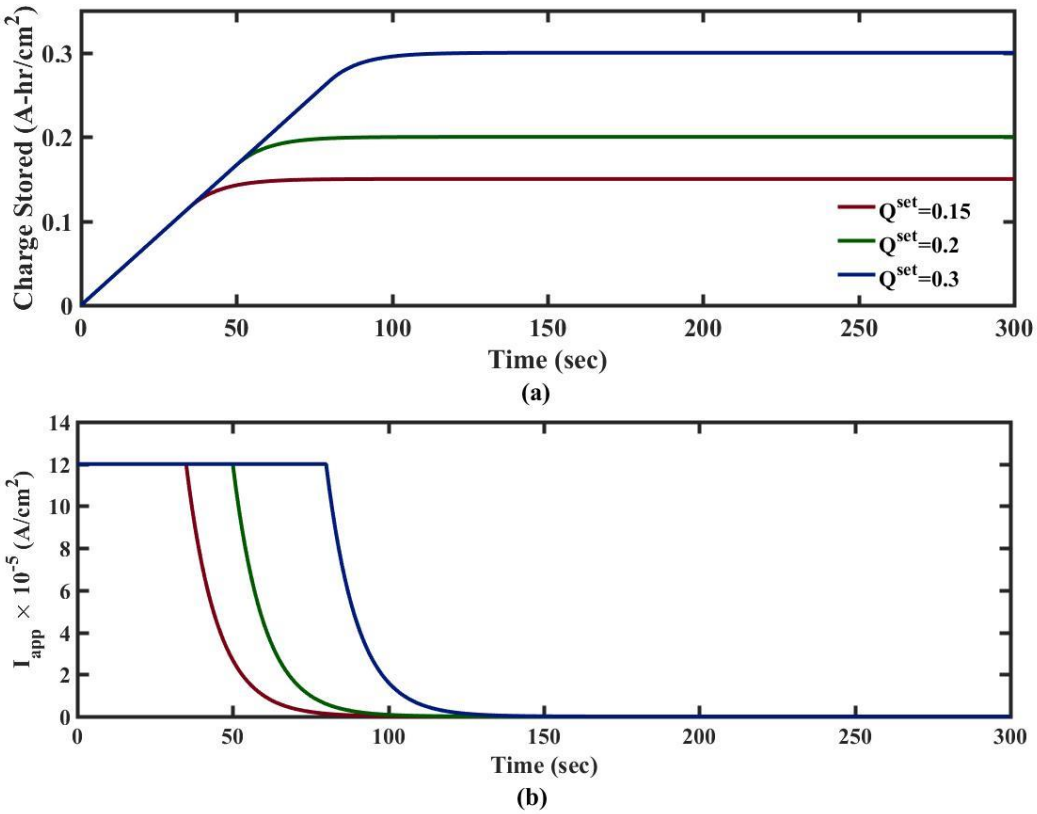

Figure 2-2: Profiles of (a) Charge stored (Q) and (b) Applied current (I_{app}) with time for the Wu and White model

c) In the third objective, the DAE model is solved for potential of the battery, ϕ_1 (which is an algebraic variable in this model) to reach its desired set point ϕ_1^{set}. For this case,

$$Y = \phi_1$$

The full derivative $\left(\frac{d\phi_1}{dt}\right)$ is not given by the model equations and $\frac{\partial g}{\partial u}(y, z, u)$ (in equation (2.9)) is not zero. The GMC formulation for this case is given by equations described earlier for the DAE model. Equations (2.16) and (2.17) can be substituted in (2.14) to get:

$$I_{app}=\left\{\begin{array}{c} i_{0,1}\left[2\left(1-y_1\right)\exp\left(\frac{\left(\phi_1-\phi_{01}\right)F}{2RT}\right)-2y_1\exp\left(-\frac{\left(\phi_1-\phi_{01}\right)F}{2RT}\right)\right]+ \\ i_{0,2}\left[\exp\left(\frac{\left(\phi_1-\phi_{02}\right)F}{RT}\right)-\exp\left(-\frac{\left(\phi_1-\phi_{02}\right)F}{RT}\right)\right] \end{array}\right\} \tag{2.31}$$

Equation (2.31) can now be differentiated to get:

$$\frac{dI_{app}}{dt}=\left[\begin{array}{l} i_{0,1}\left[\begin{array}{l} 2\left(1-y_1\right)\exp\left(a_1\right)\cdot\frac{F}{2RT}\cdot\frac{d\phi_1}{dt}+2\exp\left(a_1\right)\left(-\frac{dy_1}{dt}\right) \\ -2y_1\exp\left(-a_1\right)\cdot\left(-\frac{F}{2RT}\right)\cdot\frac{d\phi_1}{dt}-2\exp\left(-a_1\right)\left(\frac{dy_1}{dt}\right) \end{array}\right]+ \\ i_{0,2}\left[\exp\left(a_2\right)\cdot\frac{F}{RT}\cdot\frac{d\phi_1}{dt}-\exp\left(-a_2\right)\cdot\left(-\frac{F}{RT}\right)\cdot\frac{d\phi_1}{dt}\right] \end{array}\right] \tag{2.32}$$

$$a_1=\frac{\left(\phi_1-\phi_{01}\right)F}{2RT},a_2=\frac{\left(\phi_1-\phi_{02}\right)F}{2RT} \tag{2.33}$$

Equation (2.32) is rewritten for $\frac{d\phi_1}{dt}$ to get:

$$\frac{d\phi_1}{dt}=\frac{\frac{dI_{app}}{dt}+2i_{0,1}\exp\left(a_1\right)\left(\frac{dy_1}{dt}\right)+2i_{0,1}\exp\left(-a_1\right)\left(\frac{dy_1}{dt}\right)}{\left[\begin{array}{l} i_{0,1}\left[2\left(1-y_1\right)\exp\left(a_1\right)\cdot\frac{F}{2RT}-2y_1\exp\left(-a_1\right)\cdot\left(-\frac{F}{2RT}\right)\right]+ \\ i_{0,2}\left[\exp\left(a_2\right)\cdot\frac{F}{RT}-\exp\left(-a_2\right)\cdot\left(-\frac{F}{RT}\right)\right] \end{array}\right]} \tag{2.34}$$

Also, the equations for the GMC formulation is added as:

$$\frac{d\phi_1}{dt}=K\left(\phi_1^{set}-\phi_1\left(t\right)\right)+\frac{K\cdot r\left(t\right)}{\tau_i} \tag{2.35}$$

$$\frac{dr}{dt}=\left(\phi_1^{set}-\phi_1\left(t\right)\right) \tag{2.36}$$

From Equations (2.34) and (2.35), we can get:

$$\frac{\frac{dI_{app}}{dt}+2i_{0,1}\exp\left(a_1\right)\left(\frac{dy_1}{dt}\right)+2i_{0,1}\exp\left(-a_1\right)\left(\frac{dy_1}{dt}\right)}{\left[\begin{array}{l} i_{0,1}\left[\begin{array}{l} 2\left(1-y_1\right)\exp\left(a_1\right)\cdot\frac{F}{2RT}- \\ 2y_1\exp\left(-a_1\right)\cdot\left(-\frac{F}{2RT}\right) \end{array}\right]+ \\ i_{0,2}\left[\exp\left(a_2\right)\cdot\frac{F}{RT}-\exp\left(-a_2\right)\cdot\left(-\frac{F}{RT}\right)\right] \end{array}\right]}=K\left(\phi_1^{set}-\phi_1\left(t\right)\right)+\frac{K\cdot r\left(t\right)}{\tau_i} \tag{2.37}$$

Equations (2.13) – (2.17) are solved together along with equations (2.36) –(2.37) to obtain the control profiles for this case. In order to implement bounds on the applied current, a similar dummy variable $\left(I_1\left(t\right)\right)$, is added in the GMC equation. The final set of model equations solved for this case are summarized in equation (2.38).

$$
\left.
\begin{aligned}
&\frac{dy_1}{dt} = \frac{j_1 \cdot W}{F \rho V} && \text{(a)}\\
&j_1 + j_2 = I_{app} && \text{(b)}\\
&\frac{dQ}{dt} = I_{app} && \text{(c)}\\
&\frac{dr}{dt} = \left(\phi_1^{set} - \phi_1(t)\right) && \text{(d)}\\
&\frac{\dfrac{dI_1}{dt} + 2i_{0,1}\exp\left(a_1\right)\left(\dfrac{dy_1}{dt}\right) + 2i_{0,1}\exp\left(-a_1\right)\left(\dfrac{dy_1}{dt}\right)}{\left[\begin{array}{l} i_{0,1}\left[2\left(1-y_1\right)\exp\left(a_1\right)\cdot\dfrac{F}{2RT} - 2y_1\exp\left(-a_1\right)\cdot\left(-\dfrac{F}{2RT}\right)\right] + \\ i_{0,2}\left[\exp\left(a_2\right)\cdot\dfrac{F}{RT} - \exp\left(-a_2\right)\cdot\left(-\dfrac{F}{RT}\right)\right] \end{array}\right]} = K\left(\phi_1^{set} - \phi_1\left(t\right)\right) + \frac{K\cdot r\left(t\right)}{\tau_i} && \text{(e)}\\
&I_{app} = \min\left(2\times10^{-5}, \max\left(0, I_1\right)\right) && \text{(f)}\\
&j_1 = i_{0,1}\left[2\left(1-y_1\right)\exp\left(\frac{\left(\phi_1-\phi_{01}\right)F}{2RT}\right) - 2y_1\exp\left(-\frac{\left(\phi_1-\phi_{01}\right)F}{2RT}\right)\right] && \text{(g)}\\
&j_2 = i_{0,2}\left[\exp\left(\frac{\left(\phi_1-\phi_{02}\right)F}{RT}\right) - \exp\left(-\frac{\left(\phi_1-\phi_{02}\right)F}{RT}\right)\right] && \text{(h)}
\end{aligned}
\right\}
$$

(2.38)

It can be noted that in this case, equation (2.38)(b) determines the variation of the measured variable with time, and equations (2.38)(e) and (f) govern the control profile. The controller parameters for this case are K = 0.0250 and τ_i = 15. Figure 2-3 shows the results obtained for this case. Figure 2-3(a) and (b) show the potential and current profiles respectively obtained for different set points $\phi_1^{set} = \left[0.4, 0.5, 0.6\right]$.

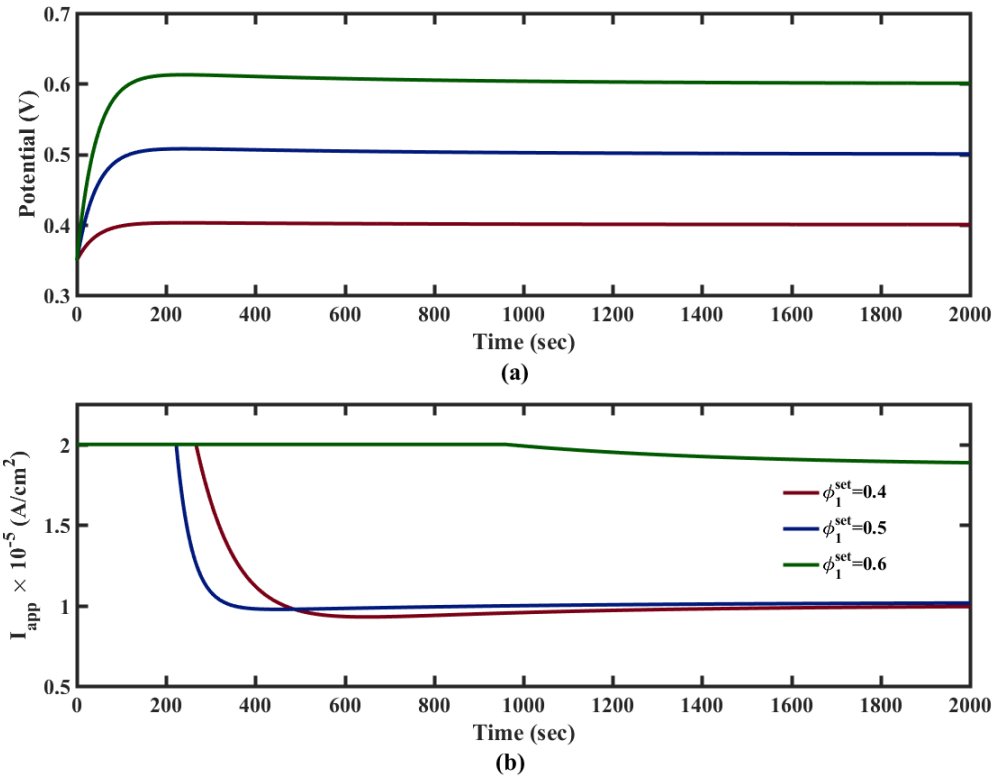

Figure 2-3: Profiles of (a) Potential (V) and (b) Applied current (I_{app}) with time for the Wu and White model

2.3.2 Single Particle Model

A single particle model[23] for an electrode is used to illustrate the concept for a model with multiple algebraic equations in the DAE system. Consider diffusion of a particle inside a spherical electrode. The model equations for this case are given by:

$$\frac{\partial c}{\partial t} = \frac{1}{r^2} \cdot \left(\frac{\partial}{\partial r} \left(r^2 \frac{\partial c}{\partial r} \right) \right) \tag{2.39}$$

With the boundary conditions

$$\text{At } r = 0, \ \frac{\partial c}{\partial r} = 0 \tag{2.40}$$

$$\text{and at } r = 1, \ \frac{\partial c}{\partial r} = j_p \tag{2.41}$$

Where c is the scaled concentration of the particle, r is the scaled radial variable in the spherical coordinate, and j_p is the scaled flux of the particle inside the electrode, which is a function of the applied current density.

The surface concentration (c_s) is given by:

$$c_s = c(r)\big|_{r=1} \tag{2.42}$$

In order to solve the model, a finite difference solution is used. The details of implementing finite difference solution (method of lines approach) can be found elsewhere[37], and is not discussed here. The final set of equations obtained after implementing finite difference for N=19 internal node points are given by:

$$\frac{dC_i}{dt} = \frac{C_{i+1} - 2C_i + C_{i-1}}{h^2} + \frac{2}{i \cdot h}\frac{C_{i+1} - C_{i-1}}{2 \cdot h}, i = 1 \ldots 19 \tag{2.43}$$

$$\frac{C_1 - C_0}{h} = 0 \tag{2.44}$$

$$\frac{C_{N+1} - C_N}{h} = j_p \tag{2.45}$$

$$C_s = c_s = C_{N+1} \tag{2.46}$$

$$h = \frac{1}{N+1} \tag{2.47}$$

where C_i is the concentration of the particle at the i^{th} node point in the radial direction. The manipulated variable for this case, is the dimensionless flux$\left(j_p\right)$. The potential of the electrode $\left(V\right)$ is defined according to a Nernst equation, as given by:

$$V\left(t\right) = E_0 - \frac{RT}{F}\log\left(C_s\left(t\right)\right) \tag{2.48}$$

Where E_0 is the open-circuit potential of the electrode and is assumed to be a function of the surface concentration $\left(C_s\right)$ of the electrode (as is the case in most battery models), *R* is the ideal gas constant. *F* is the Faraday's constant, and *T* is the temperature of the electrode, and is assumed to be 298K. The expression for E_0 used as a function of the surface concentration is shown in Table 2-2. The values of parameters are assumed only for theoretical purposes, and not versus any standard electrode. The initial conditions of all the variables are $C_i(0) = 0.5$, $V(0) = 4.09$ and $j_p(0) = 0$.

Table 2-2: Expression for the open circuit potential used for SPM

$E_0 = \begin{cases} a_1 + a_2 C_s + a_3 C_s^{\,2} + a_4 C_s^{\,3} + \\ a_5 (C_s - a)^2 \left(\frac{1}{2} tanh\left(1000\left(C_s + 1\right)\right) + tanh\left(1000\left(C_s - a\right)\right) \right) + \\ a_6 (C_s - b)^3 \left(1 - \frac{1}{2} tanh\left(1000\left(C_s + 1\right)\right) + tanh\left(1000\left(C_s - b\right)\right) \right) + \\ a_7 (C_s - c)^3 \left(1 - \frac{1}{2} tanh\left(1000\left(C_s + 1\right)\right) + tanh\left(1000\left(C_s - c\right)\right) \right) + \\ a_8 (C_s - d)^3 \left(1 - \frac{1}{2} tanh\left(1000\left(C_s + 1\right)\right) + tanh\left(1000\left(C_s - d\right)\right) \right) + \\ a_9 (C_s - e)^3 \left(1 - \frac{1}{2} tanh\left(1000\left(C_s + 1\right)\right) + tanh\left(1000\left(C_s - e\right)\right) \right); \end{cases}$	$a_1 = 9.41894182550,$ $a_2 = -20.8089294802,$ $a_3 = 26.0321098756,$ $a_4 = -11.2415464828,$ $a_5 = -292.586540767,$ $a_6 = -.212804379260$ $a_7 = 125.437252178,$ $a_8 = -198.413506247,$ $a_9 = 164.029238273$ $a = 0.96, b = 0.733,$ $c = 0.575, d = 0.535,$ $e = 0.466$

The measured variable is assumed to be *V*, and a set points of $V^{set} = \left[3.2V, 3.5V\right]$ are taken.

As in the previous case, the derivative of potential $\left(\frac{dV}{dt} \right)$ is calculated by differentiating equation (2.48). For this case,

$$Y = V$$

$$\frac{dV}{dt} = \frac{dE_0}{dC_s} \cdot \frac{dC_s}{dt} - \frac{RT}{F} \cdot \frac{1}{C_s} \cdot \frac{dC_s}{dt} \tag{2.49}$$

Moreover, $\frac{\partial g}{\partial u}\left(y, z, u\right)$ (equation (2.9)) is not zero for this case.

The GMC formulation is written as follows:

$$\frac{dV}{dt} = K\left(V^{set} - V\left(t\right)\right) + \frac{K}{\tau_i} r(t) \tag{2.50}$$

$$\frac{dr}{dt} = \left(V^{set} - V(t)\right) \tag{2.51}$$

From equations (2.49) and (2.50), we can get:

$$\frac{dE_0}{dC_s} \cdot \frac{dC_s}{dt} - \frac{RT}{F} \cdot \frac{1}{C_s} \cdot \frac{dC_s}{dt} = K\left(V^{set} - V\left(t\right)\right) + \frac{K}{\tau_i} r\left(t\right) \tag{2.52}$$

Equation (2.45) can be differentiated to get the derivative for $\frac{dC_s}{dt}$ (after substituting equation (2.46)) as

$$\frac{dC_s}{dt} = \frac{dC_{N+1}}{dt} = h \cdot \frac{dj_p}{dt} + \frac{dC_N}{dt} \tag{2.53}$$

From equations (2.52) and (2.53), we get:

$$\frac{dE_0}{dC_s} \cdot \left(h \cdot \frac{dj_p}{dt} + \frac{dC_N}{dt} \right) - \frac{RT}{F} \cdot \frac{1}{C_s} \cdot \left(h \cdot \frac{dj_p}{dt} + \frac{dC_N}{dt} \right) = K\left(V^{set} - V\left(t\right)\right) + \frac{K}{\tau_i} r(t) \tag{2.54}$$

Equation (2.54) is solved along with equations (2.43) - (2.48) to obtain the GMC control law. When there is no bound on the scaled flux, the equations to be solved are summarized as:

$$
\left.
\begin{aligned}
&\frac{dC_i}{dt} = \frac{C_{i+1} - 2C_i + C_{i-1}}{h^2} + \frac{2}{i \cdot h}\frac{C_{i+1} - C_{i-1}}{2 \cdot h}, i = 1 \ldots 19 && \text{(a)}\\
&\frac{C_1 - C_0}{h} = 0 && \text{(b)}\\
&\frac{C_{N+1} - C_N}{h} = j_p && \text{(c)}\\
&C_s = c_s = C_{N+1} && \text{(d)}\\
&C_{avg}(t) = \frac{C_0(t) + 2\left(\sum_{i=1}^{N} C_i(t)\right) + C_{N+1}(t)}{2N+2} && \text{(e)}\\
&h = \frac{1}{N+1} && \text{(f)}\\
&V(t) = E_0 - \frac{RT}{F}\log\left(C_s(t)\right) && \text{(g)}\\
&\frac{dr}{dt} = \left(V^{set} - V(t)\right) && \text{(h)}\\
&\frac{dE_0}{dC_s}\cdot\left(h\cdot\frac{dj_p}{dt} + \frac{dC_N}{dt}\right) - \frac{RT}{F}\cdot\frac{1}{C_s}\cdot\left(h\cdot\frac{dj_p}{dt} + \frac{dC_N}{dt}\right) = K\left(V^{set} - V(t)\right) + \frac{K}{\tau_i}r(t) && \text{(i)}
\end{aligned}
\right\} \qquad (2.55)
$$

The controller tuning parameter K is chosen as 1 and τ_i is assumed to be 1000. Figure 2-4(a) shows the profiles of potential with time for two different set points and the corresponding control profiles are shown in Figure 2-4(b). The profiles for surface concentration are shown in Figure 2-4(c).

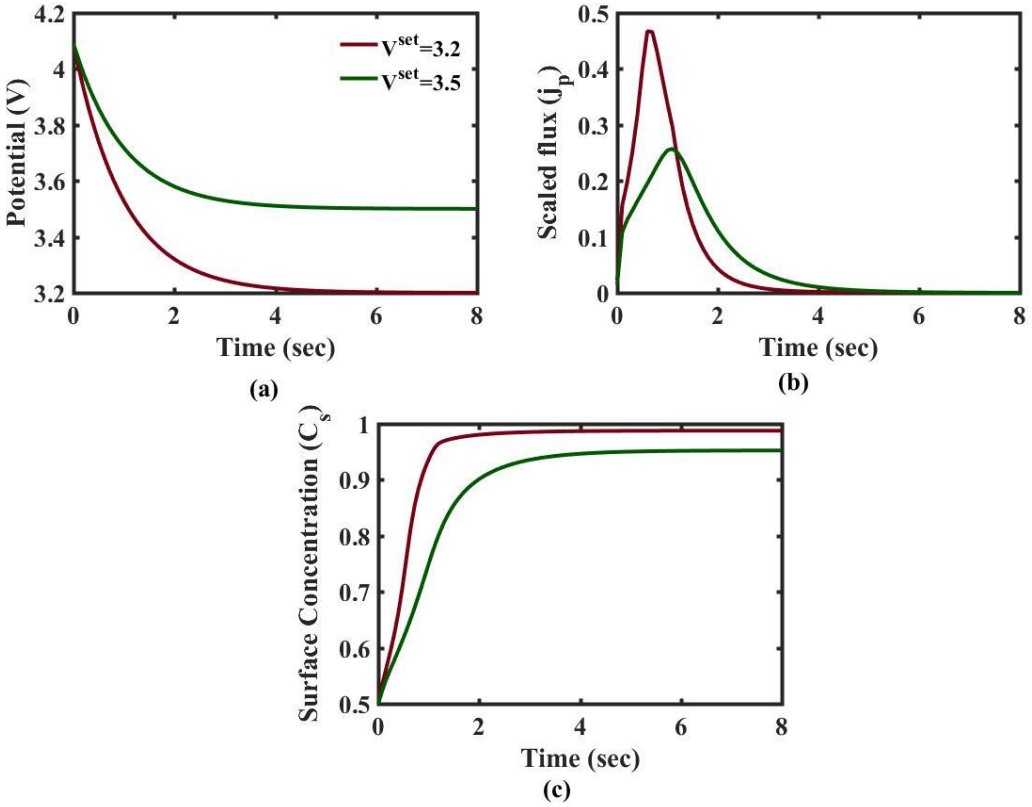

Figure 2-4: Profiles of (a) potential (V) (b) scaled flux (j_p) and (c) surface concentration (C_s) with time for the single particle model

In order to implement bounds, same procedure as discussed for the unbounded case is followed, and the equations are again summarized below but with bounds on the manipulated variable j_p .

$$
\left.
\begin{aligned}
&\frac{dC_i}{dt} = \frac{C_{i+1} - 2C_i + C_{i-1}}{h^2} + \frac{2}{i \cdot h}\frac{C_{i+1} - C_{i-1}}{2 \cdot h}, i = 1 \ldots 19 && \text{(a)}\\
&\frac{C_1 - C_0}{h} = 0 && \text{(b)}\\
&\frac{C_{N+1} - C_N}{h} = j_p && \text{(c)}\\
&C_s = c_s = C_{N+1} && \text{(d)}\\
&h = \frac{1}{N+1} && \text{(e)}\\
&V(t) = E_0 - \frac{RT}{F}\log\left(C_s(t)\right) && \text{(f)}\\
&\frac{dr}{dt} = \left(V^{set} - V(t)\right) && \text{(g)}\\
&\frac{dE_0}{dC_s}\cdot\left(h \cdot \frac{dj_1}{dt} + \frac{dC_N}{dt}\right) - \frac{RT}{F}\cdot\frac{1}{C_s}\cdot\left(h \cdot \frac{dj_1}{dt} + \frac{dC_N}{dt}\right) = K\left(V^{set} - V(t)\right) + \frac{K}{\tau_i}r(t) && \text{(i)}\\
&j_p = \min\left(0.20, \max\left(0, j_1\right)\right) && \text{(j)}
\end{aligned}
\right\} \qquad (2.56)
$$

Figure 2-5 shows the profiles obtained for an upper bound on of 0.2 for different set points on voltage. The control profiles obtained in this case again drive the measured variable to its required set point.

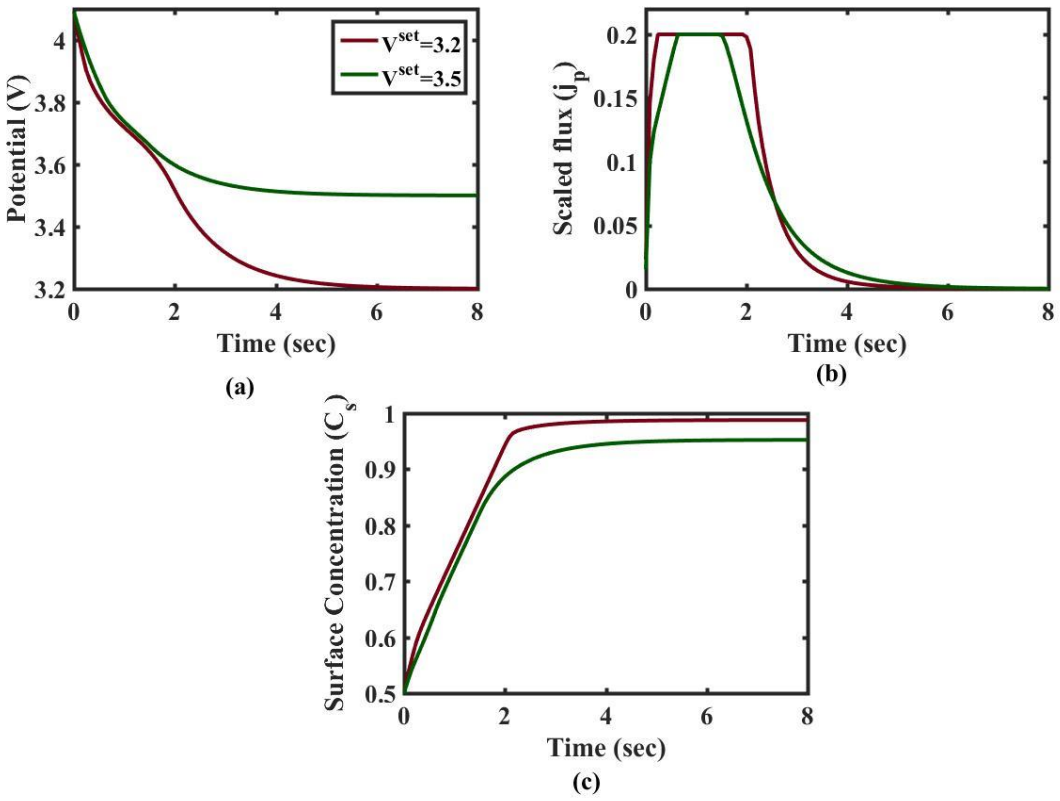

Figure 2-5: Profiles of (a) Potential (*V*) (b) Scaled flux () and (c) Surface concentration (C_s) with time for the single particle model

2.3.3 Reformulated Pseudo 2 Dimensional (P2D) Model

As mentioned previously, the P2D model proposed by Doyle *et al.*[38] is one of the most popular physics-based lithium-ion battery model. Other approaches[39,40] have been proposed for efficient simulation of battery models. Northrop *et al.*[41,42] published a reformulated battery model, based on the original P2D model, and the reformulated model was used in this work to obtain the control profiles after implementing GMC. The set of equations are given in Table 1-2 and Table 1-3. The corresponding parameters of the battery model are listed in Table 2-3.

Table 2-3: List of parameters used for the P2D model

Symbol	Parameter	Positive Electrode	Separator	Negative Electrode	Units
σ_i	Solid phase conductivity	100		100	S/m
$\varepsilon_{f,i}$	Filler fraction	0.025		0.0326	
ε_i	Porosity	0.385	0.724	0.485	
Brugg	Bruggman Coefficient		4		
D	Electrolyte diffusivity	7.5×10^{-10}	7.5×10^{-10}	7.5×10^{-10}	m^2/s
D_i^s	Solid Phase Diffusivity	1.0×10^{-14}		3.9×10^{-14}	m^2/s
k_i	Reaction Rate constant	2.334×10^{-11}		5.031×10^{-11}	$mol/(s\ m^2)/(mol/m^3)^{1+\alpha a,i}$
$c_{i,\max}^s$	Maximum solid phase concentration	51554		30555	mol/m^3
$c_{i,0}^s$	Initial solid phase concentration	25751		26128	mol/m^3
c_0	Initial electrolyte concentration		1000		mol/m^3
$R_{p,i}$	Particle Radius	2.0×10^{-6}		2.0×10^{-6}	M
a_i	Particle Surface Area to Volume	885000		723600	m^2/m^3
l_i	Region thickness	80×10^{-6}	25×10^{-6}	88×10^{-6}	M
t_+	Transference number		0.364		
F	Faraday's Constant		96487		C/mol

R	Gas Constant		8.314		J/(mol K)
T_{ref}	Temperature		298.15		K
ρ	Density	2500	1100	2500	kg/m^3
C_p	Specific Heat	700	700	700	J/(kg K)
Λ	Thermal Conductivity	2.1	0.16	1.7	J/(m K)
$E_a^{D_i^s}$	Activation Energy for Temperature Dependent Solid Phase Diffusion	5000		5000	J/mol
$E_a^{k_i}$	Activation Energy for Temperature Dependent Reaction Constant	5000		5000	J/mol

We present two cases for this model, even though GMC formulation can be applied for more variables.

(a) Set point for the charge stored in the battery

In this case, the objective is to find the current profiles to obtain the final charge stored to reach a desired set point Q^{set}, with a bound on the applied current. Mathematically,

Find $I_{app}(t)$ subject to the model equations given in Table 1-2, and the constraints

$$Q(t_f) = Q^{set} \tag{2.57}$$

$$0 \le I_{app}(t) \le 3C \tag{2.58}$$

where $I_{app}(t)$ is the applied current, $Q(t)$ is the charged stored in the battery, Q^{set} is the set-point for the charge, *C* is the capacity of the battery and t_f is the final time. The value of Q^{set} for this study is taken to be 14 Ahr.

For this problem (comparing with equation (2.9)),

$$Y = Q$$

The full derivative of the measured variable is directly available from the model thereby resulting in a direct equation for I_{app} instead of $\frac{dI_{app}}{dt}$. For this case, in equation (2.9), $\frac{\partial g}{\partial u}(y, z, u)$ is not zero.

The equation for charge stored is given by:

$$\frac{dQ}{dt} = I_{app} \tag{2.59}$$

As in the previous examples, the GMC equation can be written as:

$$\frac{dQ}{dt} = K\left(Q^{set} - Q(t)\right) + \frac{K}{\tau_i} r(t) \tag{2.60}$$

$$\frac{dr}{dt} = Q^{set} - Q(t) \tag{2.61}$$

From Equations (2.59) and (2.60), the equation for applied current can be written as:

$$I_{app} = K\left(Q^{set} - Q(t)\right) + \frac{K}{\tau_i} r(t) \tag{2.62}$$

The bounds in equation (2.58), are applied on the current as:

$$I_{app}(t) = \min\left(54, \max\left(0, K\left(Q^{set} - Q(t)\right) + \frac{K}{\tau_i} r(t)\right)\right) \tag{2.63}$$

where 54 A/m^2 is assumed to be the current equivalent for 3C. The controller tuning parameter is chosen as K = 0.01, and $\tau_i = 1e-4$. Equation (2.63) can be used along with the model equations mentioned in Table 1-2 and Table 1-3, to obtain the GMC control profile.

Figure 2-6*(a)*, shows the profile of charge stored reaching the desired set-point and the corresponding applied current profile is shown in Figure 2-6*(b)*. Since for this case, there is no constraint given on temperature, or voltage, the battery is charged at a constant current of *3C* that is the maximum bound on the current, until the charge stored reaches the desired set-point Q^{set}. After *t* = 934 seconds, the current falls to zero in order to keep the charge stored at the desired set-point Q^{set}. Figure 2-6(*c*) and 2-6(*d*) show the corresponding changes in voltage and temperature of this constant current charging case, respectively. The temperature and voltage both increase steadily as expected until the current is non-zero. After *t* = 934 seconds, when the current becomes zero, the temperature starts to fall, whereas voltage remains constant at the open-circuit value.

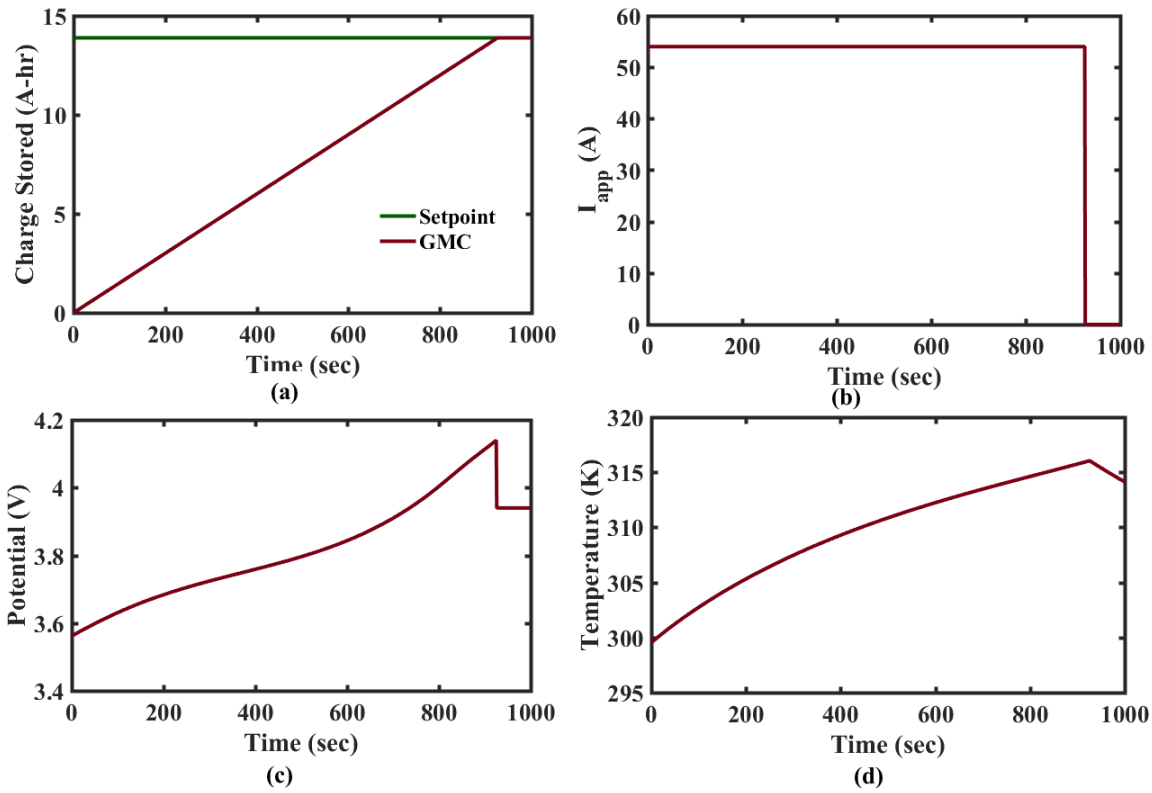

Figure 2-6: Profiles of (a) Charge stored, (b) Applied current, (c) Potential and (d) Temperature with time for the reformulated P2D model

(b) Set point for voltage of the cell.

Consider a cell being charged from a fully discharged state. The set point for the voltage while charging is set to be $V^{set} = 4.2\ V$. In the P2D model, the voltage of the cell (V) is given by the equation:

$$V(t) = \phi_1(t)\big|_{x=0} - \phi_1(t)\big|_{x=L_{pos}+L_{sep}+L_{neg}} \tag{2.64}$$

where $\phi_1(t)$ denotes the potential of the solid phase, and L_{pos}, L_{sep}, L_{neg}, represent the thicknesses of the positive electrode, separator and negative electrode of the cell, respectively.

This case is similar to the case presented in section 2.3.1(*c*), where the explicit derivative for the measured variable (voltage) is not given by the model equations.

For this case,

$$Y = V(t)$$

and $\frac{\partial g}{\partial u}(y, z, u)$ (in equation (2.9)) is not zero.

Through substitution of other model equations, it can be shown that the potential of the cell is directly dependent on the applied current $\left(I_{app}\right)$. Equation (2.64) is differentiated with time to get the derivative of potential. In order to find derivative for other terms occurring in equation (2.64), all the algebraic equations are differentiated with time, to convert the system of differential algebraic equations (DAEs) to a system of ordinary differential equations (ODEs). GMC formulation is then applied for this case as:

$$\frac{dV}{dt} = K\left(4.2 - V\left(t\right)\right) + \frac{K}{\tau_i} r\left(t\right) \tag{2.65}$$

$$\frac{dr}{dt} = 4.2 - V(t) \tag{2.66}$$

The $\frac{dV}{dt}$ term appearing in the differentiation of all the algebraic equations, is eliminated by substituting equation (2.65). The math followed is similar to the set point for potential explained for the nickel hydroxide electrode model in 2.3.1(*c*). The tuning parameter *K* is assumed to be 0.01 and τ_i is taken to be 100. Figure 2-7 (red curve) shows the results when no bound is imposed on the applied current and the potential for the PI case. In this case, the voltage of the battery goes

above 4.2V, ultimately driving the voltage to its desired set point. However, for these sets of tuning parameters, the battery is overcharged before set-point for voltage is reached, which causes an increase in the rate of battery degradation. Figure 2-7 also shows the effect of increasing the τ_i value to 1×10^9 (green curve), which drives the voltage to its set-point without going above the set-point. However, it should be noted that increasing the τ_i value decreases the impact of the integral term.

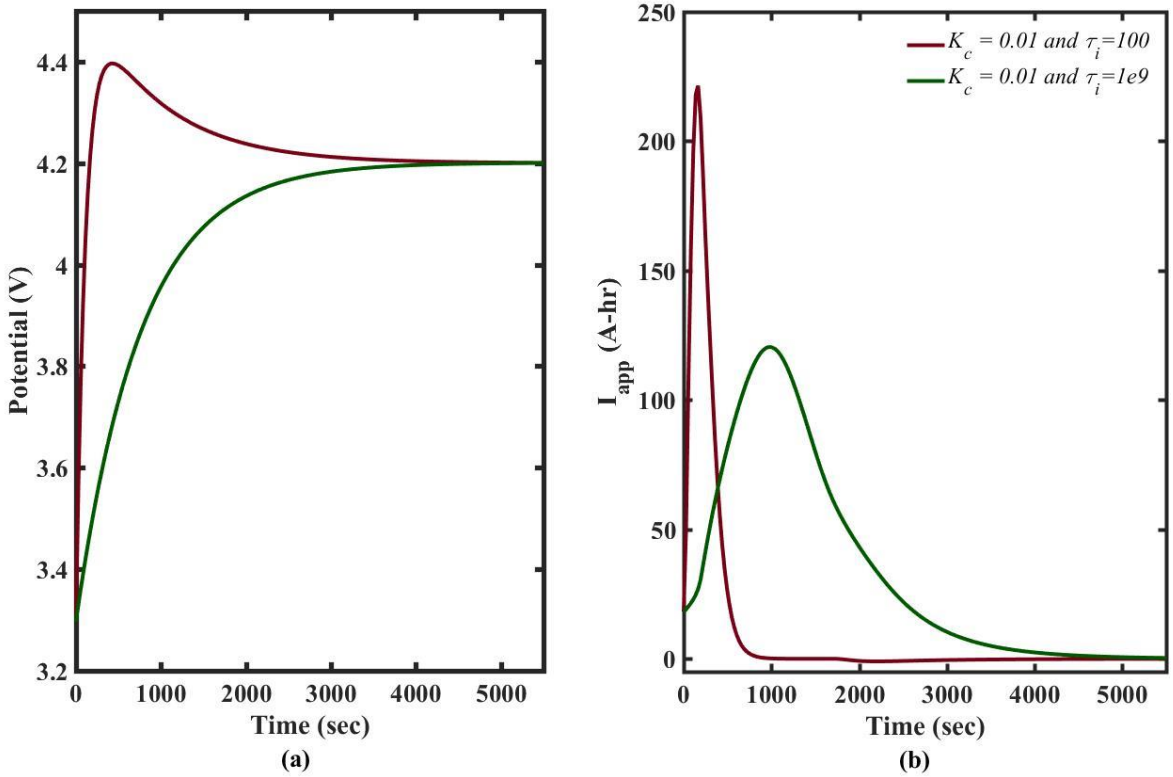

Figure 2-7: Profiles of (a) Potential (b) Applied current vs time for the P2D model obtained using PI controller

Hence, for this case, GMC formulation is applied using only a proportional term (P-Controller), as:

$$\frac{dV}{dt} = K\left(4.2 - V(t)\right) \tag{2.67}$$

For this case, the voltage of the battery reaches its set point of 4.2V, whereas the current increases first until 189s, and decreases thereafter, as shown in Figure 2-8.

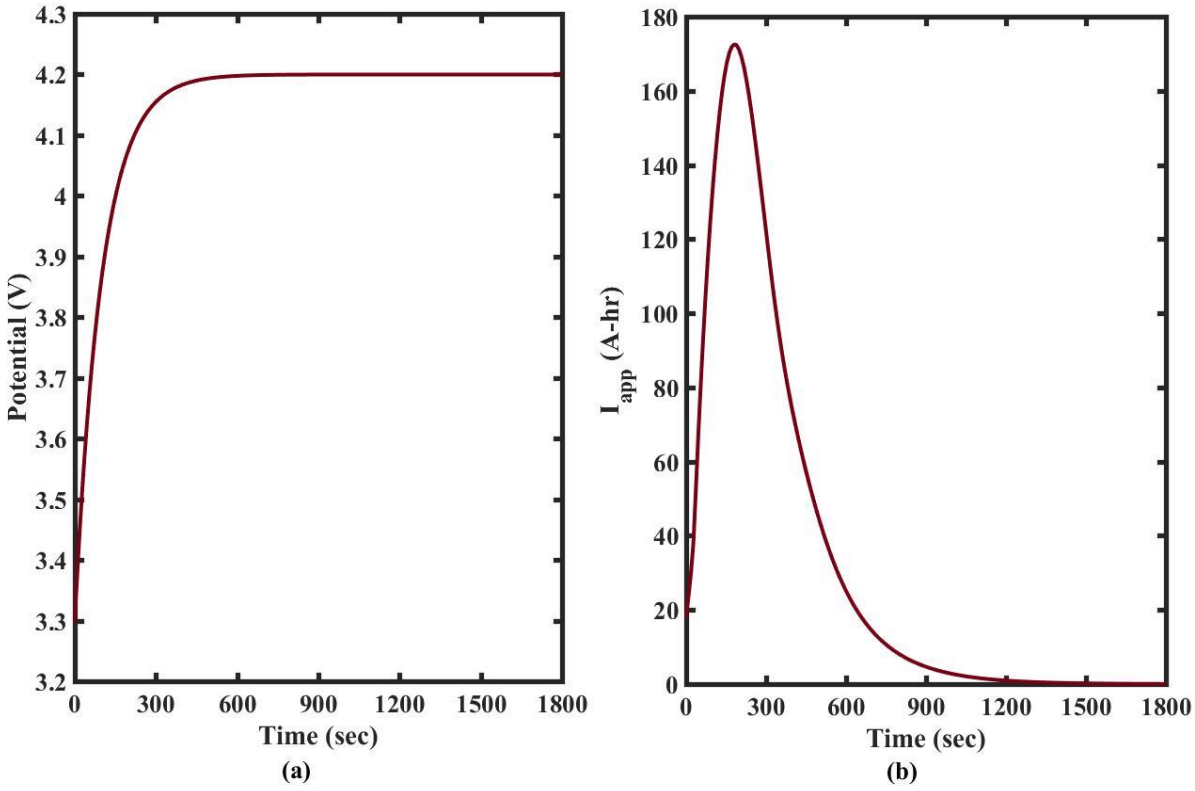

Figure 2-8: Profiles of (a) Potential (b) Applied current density vs time for the reformulated P2D model using P-controller

(c) Set point for voltage with bounds on applied current

In the next case, the set point of 4.2V is applied to the potential as in case (b), but additional bounds are added for applied current as shown below.

$$0 \le I_{app}(t) \le 30\ A/m^2 \tag{2.68}$$

This case is similar to the single particle model case described above. Figure 2-9*(a)* shows the change in voltage vs time for this case, and Figure 2-9*(b)* shows the GMC control profile for current.

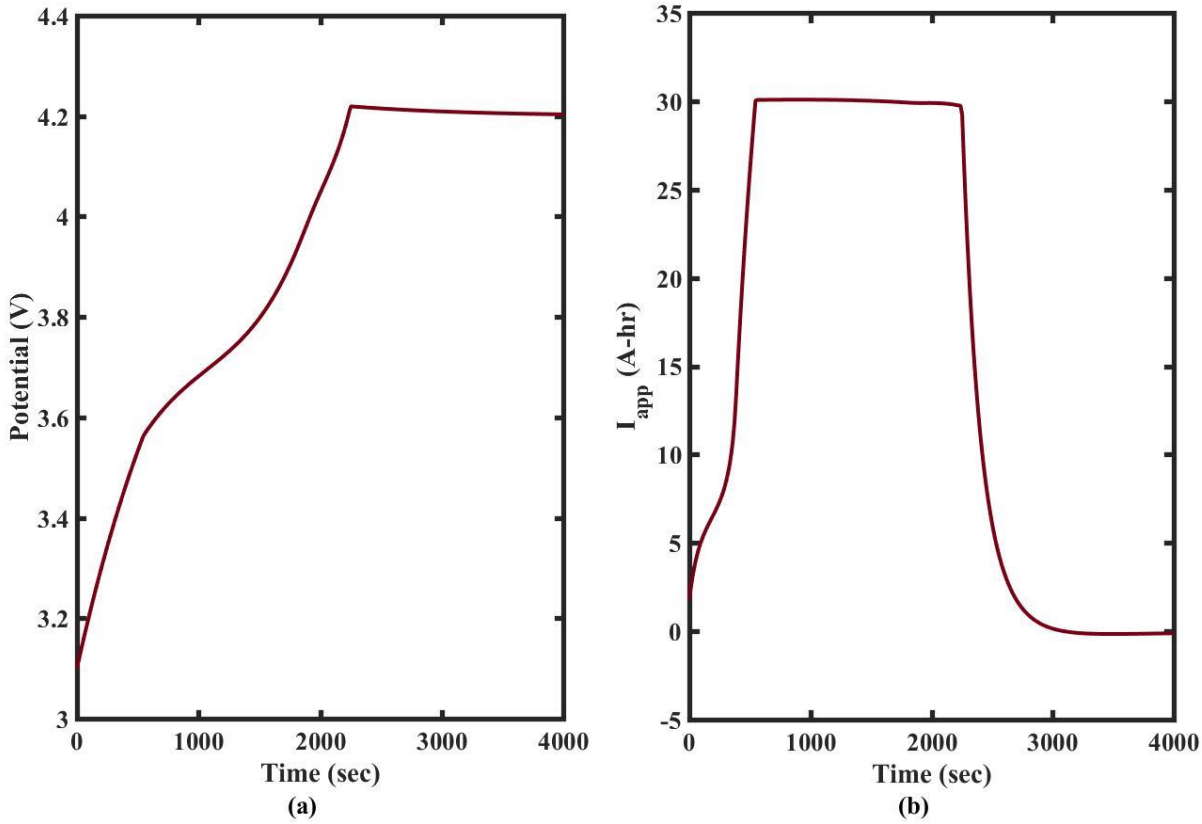

Figure 2-9: Profiles of (a) Potential (b) Applied current density vs time for the reformulated P2D model using P-Controller

Through these examples, it can be seen that the voltage reaches its desired set point for both, the bounded as well as the unbounded current case. The bounded case is closer to the real life scenario, where an upper limit is usually applied on the charging current. The advantage of implementing control through GMC is that the variables are only to be integrated in time. We implemented the control scheme using the direct iteration-free DAE numerical solvers previously reported by

Lawder *et al.*[43] This makes the approach more robust and fail-proof, as standard optimizers fail to find the optimal solution often times because of their inability to find consistent initial conditions for algebraic variables. It should be noted that for simple first order or second order processes, the time constants of the processes can be related to the tuning of the GMC parameters. However, physics-based battery models have multiple dynamics, and we choose an approach to modify the tuning parameters until no effect is seen in the profiles of control and measured variables. The arbitrariness in the tuning parameters is an inherent limitation of the GMC approach.

2.4. Performance of GMC under Model Uncertainty

Lee and Sullivan[27] have discussed the impact of uncertainty in parameters in their original manuscript. In this section, we summarize the same and discuss the uncertainty for the thin-film electrode model in section 2.3.1.

Consider the plant model given by equations (2.7) and (2.8) and the process model containing uncertainty given by:

$$\frac{dy}{dt} = f\left(y, z, u\right) \tag{2.69}$$

$$g\left(y, z, u\right) = 0 \tag{2.70}$$

The GMC formulation for the process model, where set point is given for the algebraic variable is written as:

$$\frac{dg}{dt} = \frac{\partial g}{\partial y}\left(y, z, u\right) \bullet f\left(y, z, u\right) + \frac{\partial g}{\partial y}\left(y, z, u\right) \bullet \left[K\left(z^{set} - z\right) + \frac{K}{\tau_i}\int_0^t \left(z^{set} - z\right) d\tau \right] + \frac{\partial g}{\partial u}\left(y, z, u\right) \bullet \frac{du}{dt} = 0 \tag{2.71}$$

To solve GMC under model uncertainty, equation (2.71) is used to obtain the control profile and solved along with equations (2.7) and (2.8). For the thin-film electrode model, the model

uncertainty is considered by perturbing the parameters $i_{0,1}$, ϕ_{01}, T, W by ±10%. Potential (algebraic variable) is chosen to reach its desired set-point ϕ_1^{set} in the presence of uncertain parameters mentioned above. The potential profiles obtained are shown in Figure 2-10 and it can be observed that the GMC approach gives robust performance under model uncertainty, as the controlled variable reaches its desired set-point in every case.

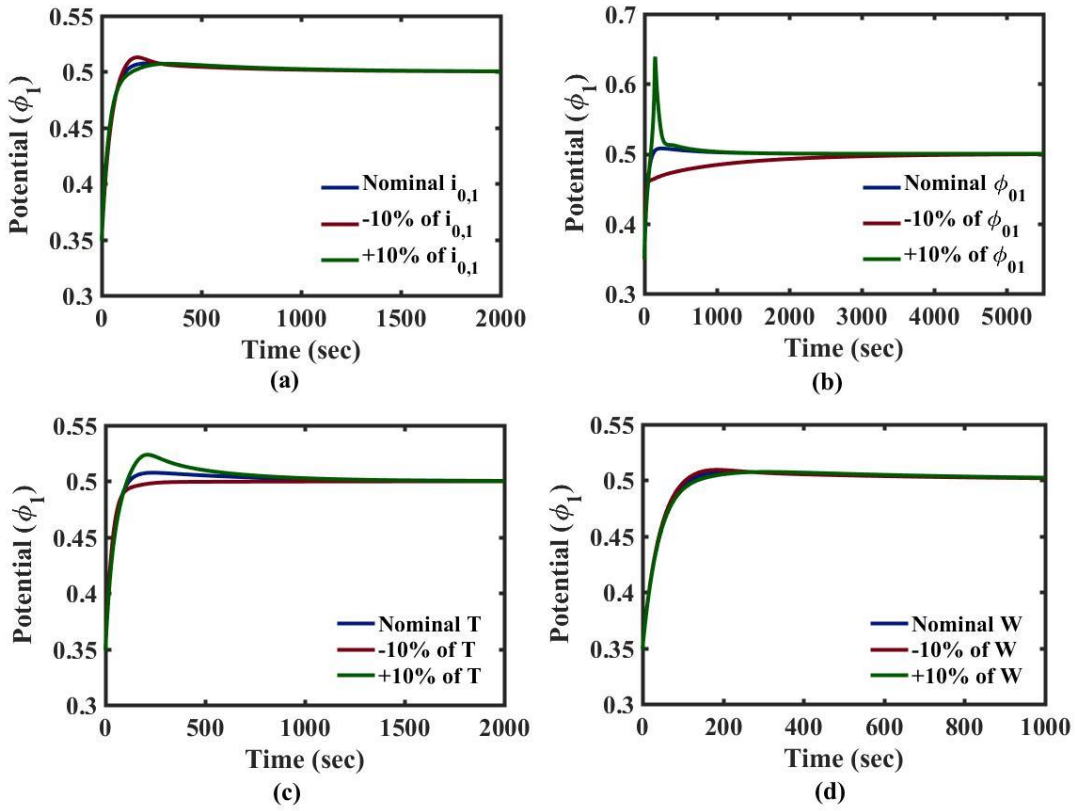

Figure 2-10: Profiles of potential reaching its specified set-point, where parameters (a) Exchange current density, (b) Equilibrium potential, (c) Temperature and (d) Mass of the active material are perturbed by ±10%

2.5. Conclusion

Generic model control is applied for different types of battery models such as thin film nickel hydroxide electrode, single particle model, along with a reformulated pseudo 2D model. The

conventional GMC approach is extended for DAEs as well as for problems involving the direct correlation between the measured and the manipulated variable. The results are presented for various case studies, and the measured variable is shown to reach the desired set point in all cases. The approach is found to be extremely robust and fail-safe. Future work involves the implementation of the GMC control scheme for problems involving constraints on various state variables (for example, bounds on voltage and temperature for the P2D model). In the GMC framework, problems involving constraints or bounds has to be solved as an optimization problem. The constraint handling strategy and the need for performing optimization in the GMC framework will be explored in a future publication. The method will also be extended to explore the control profiles for single input multiple objective case, like minimizing the capacity fade while maximizing the charge stored in the battery, while maintaining the temperature and voltage constraints, and for process and plant models with time delays.

Table 2-4: List of variables used in Chapter 2

c	Electrolyte concentration
c^s	Solid Phase Concentration
D	Liquid phase Diffusion coefficient
D_{eff}	Effective Diffusion coefficient
D^s	Solid phase diffusion coefficient
E_a	Activation Energy
F	Faraday's Constant
I_{app}	Applied Current
j	Pore wall flux
k	Reaction rate constant
l	Length of region
R	Particle Radius, or Residual
t_+	Transference number
T	Temperature
U	Open Circuit Potential
W	Weight Function
ε	Porosity
ε_f	Filling fraction
θ	State of Charge
κ	Liquid phase conductivity
σ	Solid Phase Conductivity
Φ_1	Solid Phase Potential

Φ_2	Liquid Phase Potential
k_c	Proportional Gain
τ_i	Integral Time Constant

Table 2-5: List of subscripts

eff	Effective, as for diffusivity or conductivity
n	Related to the negative electrode—the anode
p	Related to the positive electrode—the cathode
s	Related to the separator or the solid phase
app	Applied

Table 2-6: List of superscripts

avg	Average, as for solid phase average concentration
surf	Surface, as for solid phase surface concentration
s	Related to solid phase

Chapter 3: Experimental Validation of Optimal Model-based Control

3.1. Introduction

Most model-based control approaches for battery operations use empirical[44,45] or single-particle models (SPM).[46,47] The energy maximization problem with constraints on voltage has been solved over fixed time periods,[22] and the optimal charging current has been determined for a Li-ion battery experiencing capacity fade using the SPM.[23] More recently, models with more detailed descriptions of physicochemical phenomena have been used to predict optimal charging profiles for minimizing the intercalation-induced stresses inside the particle.[25] Optimal profiles have been determined for storing a given amount of charge while avoiding lithium plating, using a combination of time-scale separation and pseudo-spectral optimization.[48] Optimal current profiles with constraints on solid- and electrolyte-phase concentration and temperature has been calculated.[49] The minimum-time charging problem with constraints on the voltage and temperature has been solved.[50] A method has been proposed to minimize the cost of vehicle battery charging also accounting for the battery degradation with variable electricity costs using the single-particle model.[26]

However, none of the past papers have validated optimal model-based control strategies in a detailed experimental study. One of the main reasons for the lack of validation is that, for the coin cells typically tested in university laboratories, the cycle lives are bad because of precision issues. For long-life cycle testing, large-format cells are needed. Large-format cells need large currents, which are difficult to provide in small laboratory settings. In this work, model-based control algorithms were derived in a university environment, and laboratory testing was performed at the

National Renewables Energy Laboratory (NREL). This study is the first to experimentally demonstrate that the improved extra knowledge obtained by sophisticated physics-based models results in significant improvements in battery performance when employed in a real time control algorithm. Of course, the closed-loop performance is positively related to the accuracy of the model used in the control algorithm. This work employs the Pseudo 2-Dimensional (P2D)[38] model which captures spatial variations within particles and across the electrode, while modeling the electrochemical transport and kinetics within a cell. Using an SPM or lower level model would result in a reduction in the performance improvement obtained from model-based control. The identification of parameters for the P2D model that fits the experimental data is a separate research topic, and has been investigated in detail for different parameters in the past from various research groups,[51-55] and so is not explored in this study.

Here, we present the experimental results obtained using optimal control strategies derived using a reformulated P2D model developed earlier, for minimizing the capacity fade caused by Solid Electrolyte Interface (SEI) layer formation in graphite anodes. The derived profiles are tested at NREL on 16 Ah NMC based pouch cells. The capacity vs. cycle life data are compared with a baseline case of 2C CC-CV charge for 30 min/5C discharge at the same temperature, which shows an improvement in battery life of more than 100% for this particular charge/discharge/battery chemistry. The mathematical model for the battery, model-based control profiles, the experimental procedures, and the results are detailed in the next sections.

3.2. Model Description

As mentioned earlier, the reformulated P2D model[41] is used in this work. The model accounts for the electrochemical, transport, and thermodynamic processes in a battery to predict its internal

states. The model and approach are general enough to be integrated with any capacity fade mechanism including plating side reactions and intercalation-induced particle stress fracture, as discussed below.

Capacity Fade: SEI layer formation is considered as one of the important side reactions responsible for capacity loss of Li-ion batteries with repeated cycles. This study uses the model of Ramadass *et al.*[56] integrated with a reformulated model to predict the battery performance and to derive the optimal control profile. The model is based on the assumption of a continuous and very slow solvent diffusion followed by reduction side reaction at the surface of the anode while charging the cell. The loss of active material is assumed to be due to this side reaction, which is also responsible for the SEI layer formation, on the surface of the anode, during continuous cycling of the cell. SEI layer formation is assumed to occur only while charging the cell. Since the ratio of charging capacity remains almost equal to the discharged capacity across every cycle, the capacity fade or any other side reaction is neglected during discharge, as in Ramadass *et al.*[29]

Butler-Volmer (BV) kinetics are assumed to describe the Li-ion intercalation reaction in the anode, as well as the formation of SEI layer side reaction. The local volumetric charge transfer current density is given by

$$J = J_n + J_{SEI} \tag{3.1}$$

where the volumetric current density for the anodic intercalation reaction is

$$J_n = a_n i_{0,n}\left[\exp\left(\frac{\alpha_{a,n}F}{RT}\eta_n\right) - \exp\left(-\frac{\alpha_{c,n}F}{RT}\eta_n\right)\right], \tag{3.2}$$

the equilibrium exchange current density of the anodic intercalation reaction is

$$i_{0,n} = k_n\left(c_{1,n}^{\max} - c_{1,n}^{s}\right)^{\alpha_{a,n}}\left(c_{1,n}^{s}\right)^{\alpha_{c,n}}\left(c_2\right)^{\alpha_{a,n}}, \tag{3.3}$$

the overpotential is

$$\eta_n = \phi_1 - \phi_2 - U_{n,\text{ref}} - \frac{J_n}{a_n} R_{\text{film}}, \tag{3.4}$$

the reference $U_{n,\text{ref}}$ is a function of the state of charge (θ) of the electrode, the volumetric current density for the SEI layer side reaction is

$$J_{\text{SEI}} = -i_{0,\text{SEI}} a_n \exp\left(-\frac{\alpha_c n F}{RT}\eta_{\text{SEI}}\right), \tag{3.5}$$

the SEI overpotential is

$$\eta_{\text{SEI}} = \phi_1 - \phi_2 - U_{\text{ref,SEI}} - \frac{J}{a_n} R_{\text{film}}, \tag{3.6}$$

the SEI reference $U_{ref,SEI}$ is assumed to be 0.4 V vs. Li/Li$^+$, the film resistance for the first cycle is

$$R_{\text{film}} = R_{\text{SEI}} + R_p(t), \tag{3.7}$$

and

$$R_p(t) = \frac{\delta_{\text{film}}}{\kappa_p}, \tag{3.8}$$

$$\frac{\partial \delta_{\text{film}}}{\partial t} = -\frac{J_{\text{SEI}} M_p}{a_n \rho_p F}. \tag{3.9}$$

The film resistance for subsequent cycles is given by

$$R_{\text{film}}\big|_N = R_{\text{film}}\big|_{N-1} + R_p(t)\big|_N. \tag{3.10}$$

The capacity lost due to the side reaction is given by

$$Q_{\text{SEI}} = -\int_0^{t_f} i_{\text{SEI}} dt \tag{3.11}$$

where

$$i_{\text{SEI}} = \int_0^{L_n} J_{\text{SEI}} dx \,. \tag{3.12}$$

Model equations for the P2D model are listed in Table 1-2 and Table 1-3. Representative values for the parameter set obtained from the literature are given in Table 2-3.

3.3. Optimal Model-based Control Formulations

Since the growth of the SEI layer is a function of the applied current and overpotential, optimal charging profiles can be developed that minimize the SEI layer growth, while ensuring the same capacity in a given time. Minimizing the SEI layer growth reduces the lost capacity, which in turn increases the cycle life. Various control strategies ranging from indirect methods to simultaneous discretization can be used to obtain the optimal profiles for Li-ion battery models. We implemented model-based optimal control to minimize the capacity fade for Li-ion batteries. To obtain the control profiles, a modified version of Control Vector Parameterization (CVP) was implemented and verified with simultaneous optimization strategies which are straightforward to apply for path-constrained problems. The mathematical formulation for minimizing the capacity fade due to SEI layer growth is

$$\min_{i_{\text{app}}(t)} Q_{\text{SEI}} = -A^* \int_0^{t_f} \left(\int_0^{L_n} J_{\text{SEI}} dx \right) dt \tag{3.13}$$

$$0 \le i_{\text{app}}(t) \le 54 \text{ A/m}^2 \tag{3.14}$$

$$2.8 \text{ V} \le V(t) \le 4.2 \text{ V} \tag{3.15}$$

$$Q_{\text{stored}} \ge 16 \text{ Ahr} \tag{3.16}$$

subject to the model equations in Table 1-2.

This optimal control formulation and calculation is the exactly same as one step of model predictive control (MPC), which is the most commonly implemented advanced process control method implemented in industry and has been explored for application to lithium-ion battery operations.[20,22,16,57,58] In MPC, the optimal control problem is solved at multiple sampling instances, based on the most recent measurements (for batteries, the measurements are voltage and temperature). The main advantage of MPC is that the online calculations account for the effects of model uncertainties and disturbances on the computed optimal control profiles; the main disadvantage is the online computational cost. A drawback of MPC is that the online computations expend energy, which reduces the amount of energy from the battery available for the use. As such, the appropriateness of online optimal control calculations for a particular battery application depends on the quantity of energy incurred by online calculations compared to the energy and battery lifetime savings that would be incurred by the online calculations and the total energy used for intended purpose of the battery. For example, the extra cost of online optimal control calculations would not be justifiable for an implantable cardiac pacer application, in which online calculations would cause the battery to drain too quickly. Motivated by such small battery applications, the optimal control profile in this study computed for cycle 1 was repeated for later cycles, rather than recomputed. For large battery applications, the optimal control profiles can be updated online based on new parameter values during each cycle, or once after each cycle or after many cycles.

The implemented control profile was obtained after trying to implement different profiles experimentally for a given cycle. We performed simultaneous discretization, conventional CVP, and a modified version of CVP to finally arrive at the optimal profile. Each of these approaches for calculating the optimal profiles is described below for the reformulated P2D model.

1) *Simultaneous Discretization*: In this approach, the governing partial differential equations are discretized in the spatial direction to generate ordinary differential equations (ODEs) in time. The ODEs are further discretized in time using Euler backward discretization to create a system of nonlinear algebraic equations. Although only first-order accurate, Euler backward was chosen due to its unconditional numerical stability and ease of demonstration. In this approach, both the control and state variables are discretized in temporal space. During optimization, this set of nonlinear equations acts as constraints. The objective function to be minimized was then defined as $Q_{SEI}(t_f)$, with the maximum charging current as 54 A/m^2, and the bounds on the voltage to be between 2.8 V and 4.2 V. The constraint on the total charge stored to be greater than 16 Ah was also implemented as defined in equation (3.13)-(3.16) above. Note that the bounds on the manipulated variable (applied current in this case) and voltage of the cell were implemented by providing a bound on the resulting discretized variables for current and voltage at each discretized time point. The resulting nonlinear optimization was solved in IPOPT,[59] which is based on an interior-point algorithm implemented in the C programming language, with the optimized current and voltage profiles shown in Figure 3-1(a) and Figure 3-1(b).

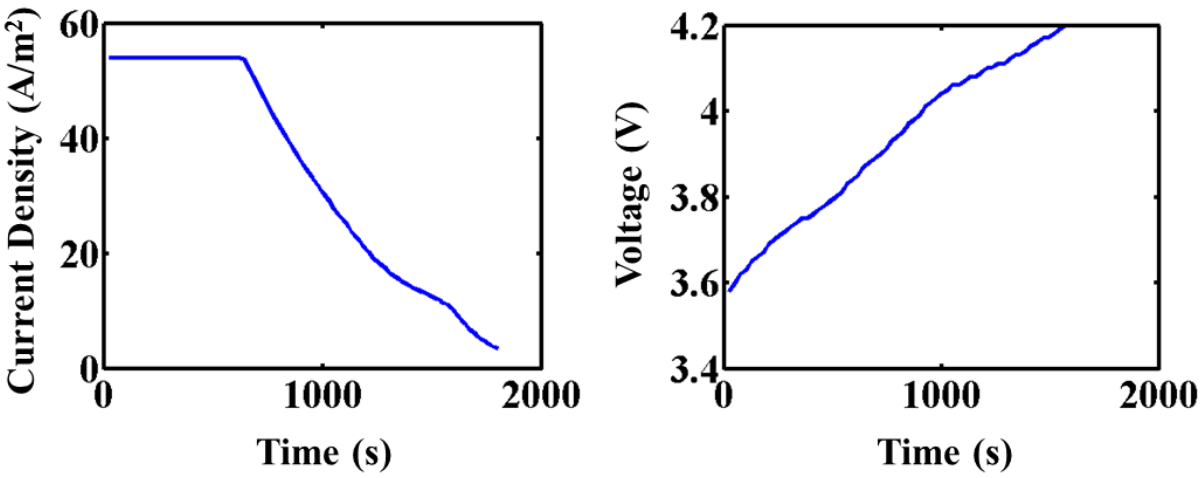

Figure 3-1: (a) Current density vs. time and (b) Voltage vs. time profiles computed for the simultaneous discretization approach

2) *Control Vector Parameterization*: In this approach, the total time horizon is divided into a finite number of time intervals. The manipulated variable (applied current) is assumed to be constant in each time interval, and the resulting optimization is solved for the discrete manipulated variables in each time interval. To explain further for this optimization, the total 1800 s time interval was divided into six time intervals, and the current was assumed to be constant in the first four regions, until 1200 s. For example, the currents at the times 0, 300, 600, 900, 1200 s are given by i_1, i_2, i_3, i_4, i_5, respectively. The current as a function of time is given by

$$i_{\text{app}}(t) = \begin{cases} i_1, & \text{for } 0 \le t \le 300 \\ i_2, & \text{for } 300 < t \le 600 \\ i_3, & \text{for } 600 < t \le 900 \\ i_4, & \text{for } 900 < t \le 1200 \\ i_5, & \text{for } 1200 < t \le T_{V=4.2\text{V}} \end{cases} \tag{3.17}$$

For the latter time period, the battery is charged with a constant current i_5 until the voltage reaches 4.2 V, after which the battery is charged at a constant voltage of 4.2 V for a total time of 30 minutes.

For the control implementation, the optimization was solved for maximizing the charge stored in 1800 s, with a penalty on the capacity fade of the battery, that is,

$$\max_{i_{app}(t)} Q_{t_f} = A * \int_0^{t_f} i_{app}(t)dt \tag{3.18}$$

$$0 \leq i_{app}(t) \leq 54 \text{ A/m}^2 \tag{3.19}$$

$$2.8 \text{ V} \leq V(t) \leq 4.2 \text{ V} \tag{3.20}$$

$$Q_{SEI} \leq 0.5 Q_{SEI,max} \tag{3.21}$$

subject to model equations in Table 1-2, where Q_{t_f} is the total capacity of the battery or the amount of charge stored in the battery, t_f is 30 minutes, and $Q_{SEI,max}$ is the maximum capacity lost to the SEI layer side reaction in a single cycle, which also means the capacity fade of the battery in a single cycle. This value was obtained from the experimental data after repeatedly cycling the battery at C/2 charge/1C discharge (Case A) as explained more in the next section.

The resulting optimization is solved using *NLPSolve* optimizer in *Maple 14*, to find the optimal values of i_1, i_2, i_3, i_4, i_5 in the specified time intervals, with the current and voltage profiles shown in Figure 3-2(a) and Figure 3-2(b).

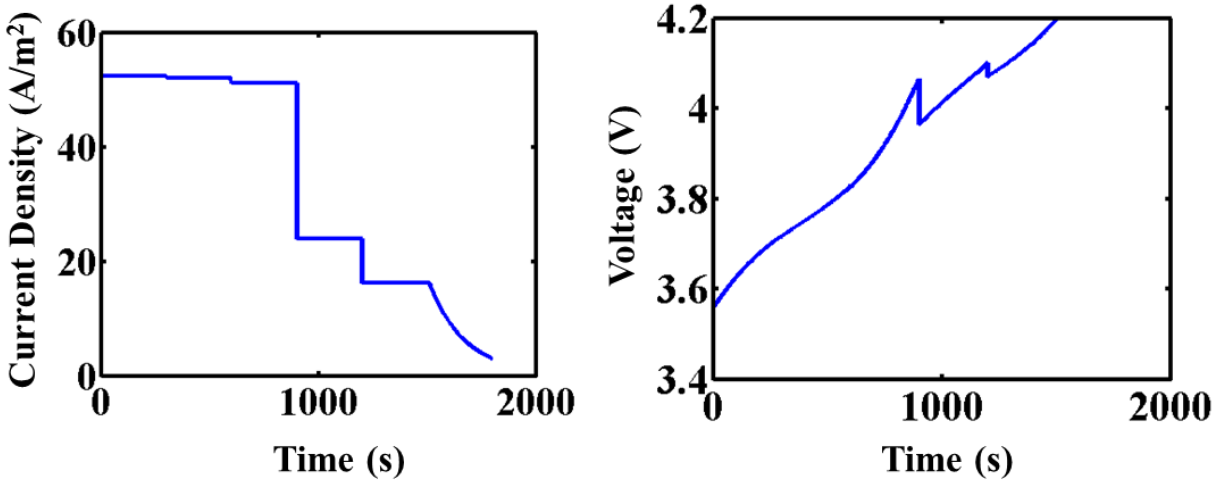

Figure 3-2: (a) Current density vs. time and (b) Voltage vs. time profiles computed for the CVP approach

3) *Modified CVP*: This approach is a slight variation of the above CVP. The total 1800 s time interval was divided again into six time intervals, but in this case, the current was assumed to be varying linearly in the first four regions, until 1200 s. For example, the currents at the times 0, 300, 600, 900, 1200 s are given by i_1, i_2, i_3, i_4, i_5, respectively. The current in each of the time regions is assumed to vary linearly, and is given by

$$i_{\text{app}}(t) = \begin{cases} i_1 + \left(\dfrac{i_2 - i_1}{300 - 0}\right)t, & \text{for } 0 \le t \le 300 \\ i_2 + \left(\dfrac{i_3 - i_2}{600 - 300}\right)(t - 300), & \text{for } 300 \le t \le 600 \\ i_3 + \left(\dfrac{i_4 - i_3}{900 - 600}\right)(t - 600), & \text{for } 600 \le t \le 900 \\ i_4 + \left(\dfrac{i_5 - i_4}{1200 - 900}\right)(t - 900), & \text{for } 900 \le t \le 1200 \\ i_5, & \text{for } 1200 \le t \le T_{V=4.2\text{V}} \end{cases} \tag{3.22}$$

After time t = 1200 s, the current i_5 is assumed to be constant until the voltage reaches 4.2 V. Charging is at constant voltage after that until the total time is 1800 s. The optimization formulation is the same as in equations (3.18) to (3.21). The optimal control problem is solved in each of the regions using the *NLPSolve* optimizer in *Maple 14*, to obtain the optimal values for i_1, i_2, i_3, i_4, and i_5, with the optimal current and voltage profiles shown in Figure 3-3(a) and Figure 3-3(b)

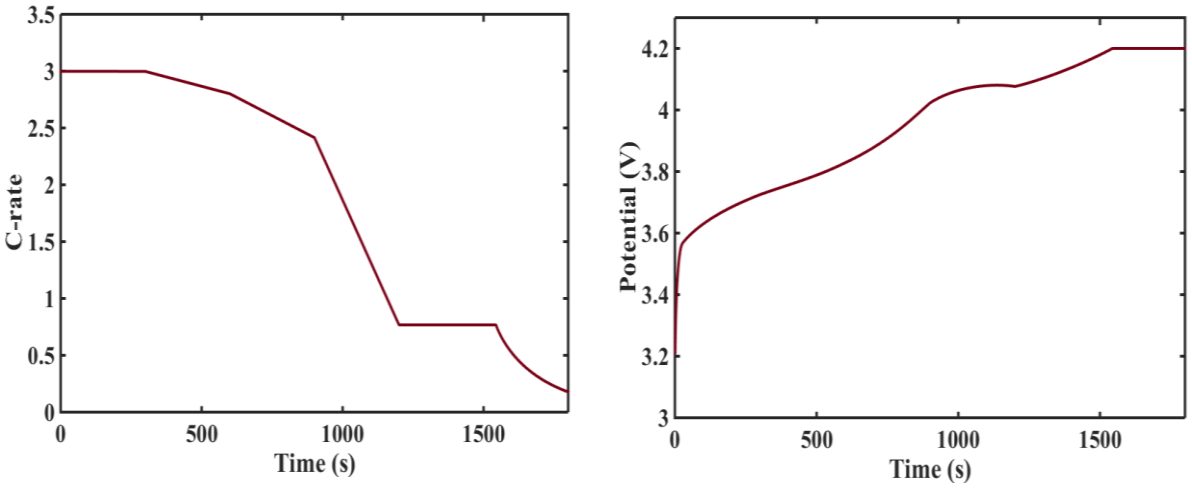

Figure 3-3: (a) Current density vs. time and (b) Voltage vs. time profiles computed for the modified CVP approach

From Figure 3-1(a)(b), it can be seen that finally towards the end of charge in the simultaneous approach, the charging profile mimics the constant potential mode. In the implementation of the CVP and modified CVP approaches, assuming constant potential at the end decreased the optimization time and the number of stages, and provided a better objective function value. The total number of stages was chosen as 6, because increasing the number of stages any further did not have significant impact on the optimal value for the cell capacity. Since the current is continuous, there is no jump in potential as in the previous case.

The current and voltage profiles obtained from experiments have good agreement with the model predictions for the simultaneous discretization, CVP, and modified CVP approaches (see Figure 3-4 to Figure 3-6). The best agreement was for the modified CVP approach. The implementation of the conventional CVP and the modified CVP approach requires robust solvers to integrate highly stiff nonlinear equations in time. In the modified CVP approach, the assumption of a linear current profile in each time interval results in a continuous profile that avoids initialization issues for DAEs,[43] whereas the conventional CVP approach leads to discontinuities and hence have DAEs that are harder to solve. As such, the modified CVP approach has lower computational cost and preferred for experimental implementation.

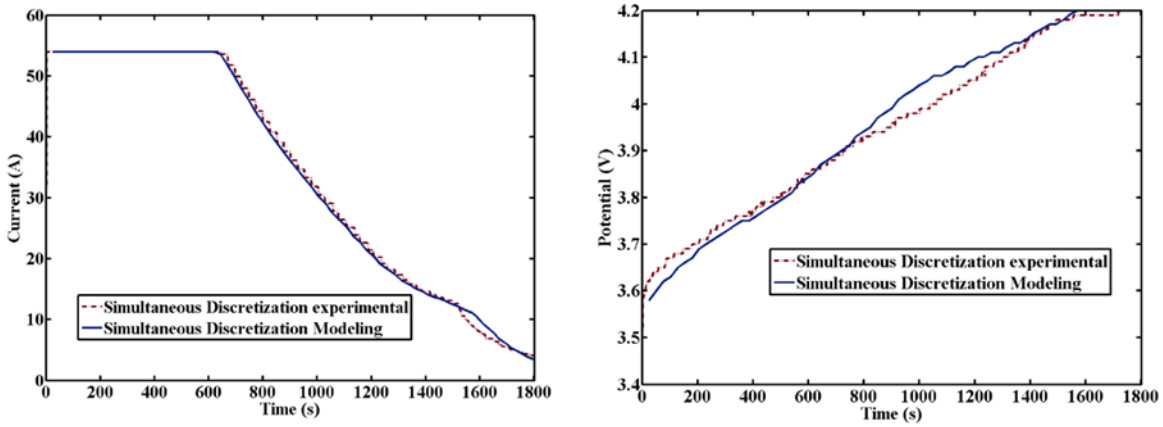

Figure 3-4: Comparison of experimental and predicted (a) Current vs. time and (b) Voltage vs. time profiles obtained using simultaneous discretization

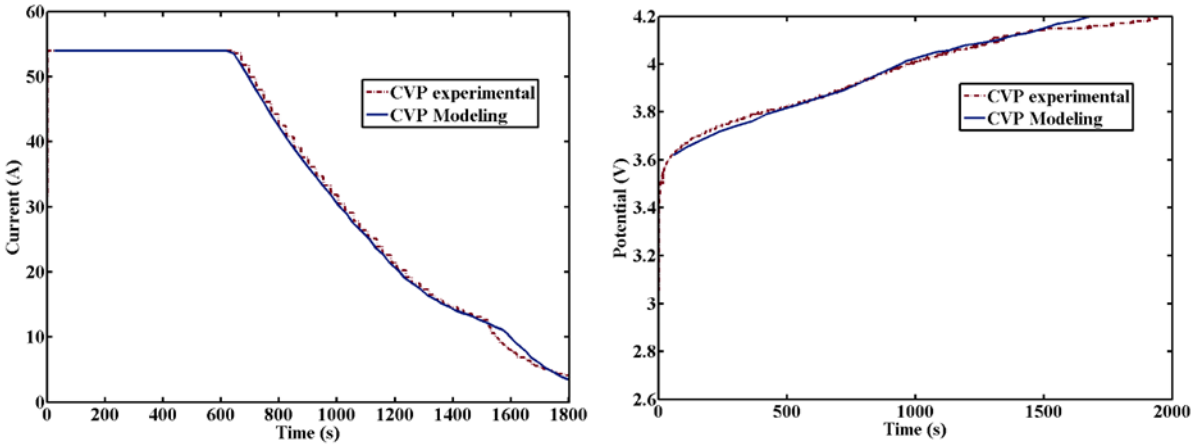

Figure 3-5: Comparison of experimental and predicted (a) Current vs. time and (b) Voltage vs. time profiles for CVP approach

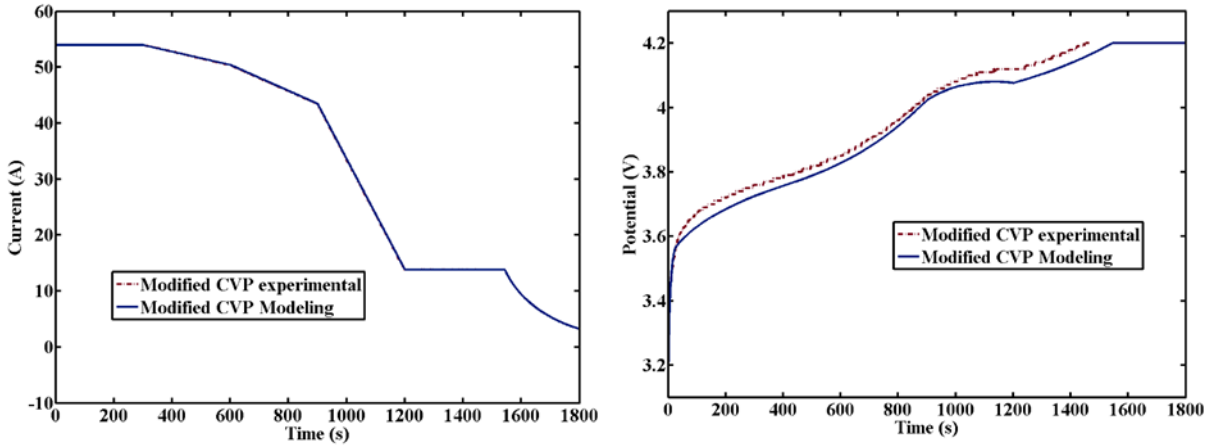

Figure 3-6: Comparison of experimental and predicted (a) Current vs. time and (b) Voltage vs. time profiles for the modified CVP approach

3.4. Experimental Validation

To quantify the benefits obtained from these control profiles, 16Ahr NMC pouch cells were cycled with the obtained charging profiles. In Case A, the cells were cycled under mild currents to obtain a baseline for the best-case performance of the cells. The cells were charged at a C/2 rate to 4.2 V, followed by a CV charge at 4.2 V until the charge current tapered off to C/10 (1.6 A) or less and

then discharged at 1C rate to 2.8 V. In another set of cycling experiments, the cells were charged at the 2C rate until the cutoff voltage of 4.2 V was reached followed by a CV charge such that the total charge time was 30 minutes, followed by a 5C discharge to 2.8 V. This set of experiments is referred to as Case B. A third set of cells were charged with the optimal control profile for the same duration as Case B (i.e., 30 minutes) and discharged under identical conditions (i.e., 5C currents to 2.8 V), which is referred to as Case C. All the cycling experiments were performed in a controlled environmental chamber at 30ºC. The optimization was formulated using:

(1) Life estimates based on the cycling conditions from Case A. This case provides the values for $Q_{\mathrm{SEI,max}}$ as mentioned above.

(2) Charge and life behavior from Case B.

(3) The Case C objective, minimize fade while charging in 30 minutes (with SEI layer growth at all the points less than 50% of Case B, making sure full charge was stored). This number needs to be as low as possible. If only 10% is indicated, please note that battery might not charge at all. The idea of this approach is to store the same charge while keeping the fade minimal. While strictly speaking, this is a pareto-optimal problem, only the best possible fade minimization with guaranteed charge stored was used.

3.5. Results and Discussion

The profile in Figure 3-3(a) was used to charge the cells, which is referred to as “MPC” as discussed in the mathematical formulation. Figure 3-7 shows the experimentally determined reduction in capacity vs. number of cycles for the CC-CV case and the MPC case. While the battery charged with the CC-CV profile reaches end of life after around 900 cycles, the battery with the

MPC profile cycles more than 1800 cycles before reaching end of life, which is a gain of more than 100% in cycle life.

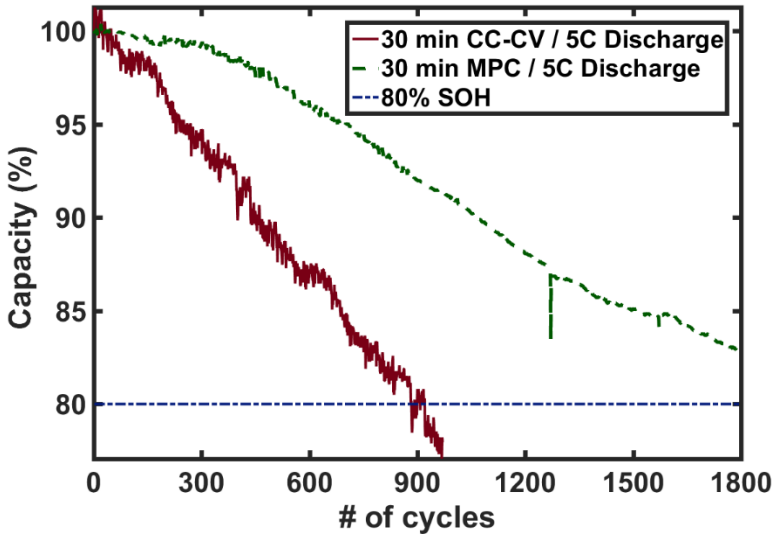

Figure 3-7: Capacity vs. number of cycles for 2C CC-CV and the MPC profiles, where "MPC" refers to the optimal charging profile obtained by the modified CVP approach

Figure 3-8 to Figure 3-10 compare the concentration of lithium ions in the electrolyte solution at the cathode-current collector interface, cathode-separator interface, and the anode-separator interface respectively, for the CC-CV and the optimal control cases. As the battery charges, the concentration varies minimally with time in any of the regions. The shape of the concentration profiles mimics that of the current profile in the cathode as the concentration of lithium in the electrolyte decreases with time (compare Figure 3-8 and Figure 3-9 with Figure 3-3(a)), whereas the reverse happens in the anode (compare Figure 3-10 with Figure 3-3(a)).

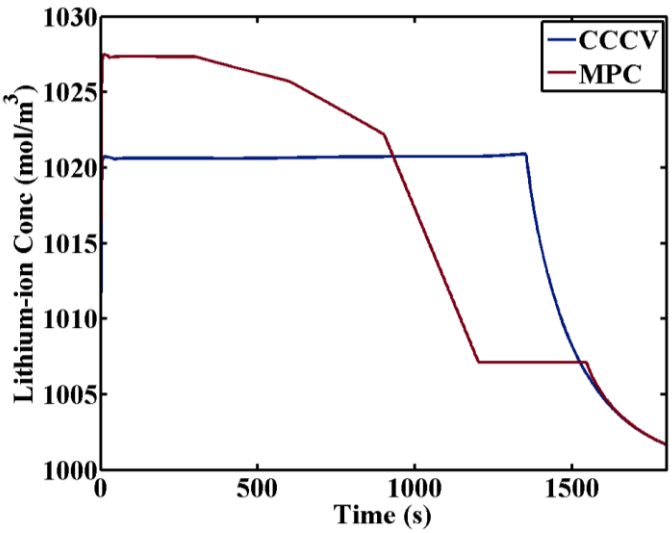

Figure 3-8: Lithium-ion concentration at the cathode-current collector interface

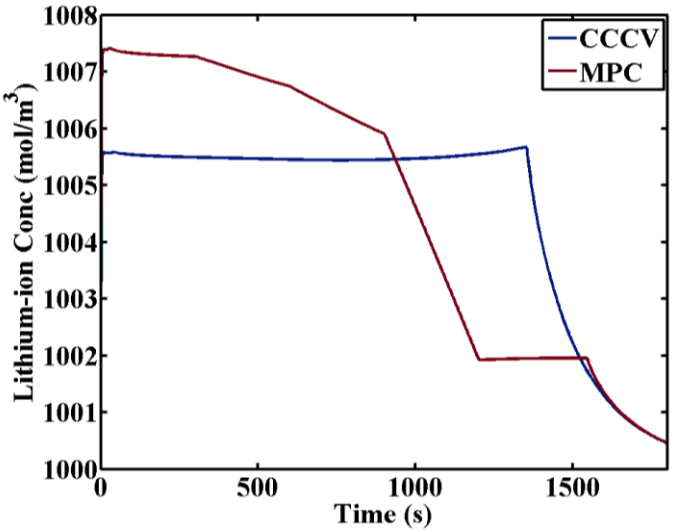

Figure 3-9: Lithium-ion concentration at the cathode-separator interface

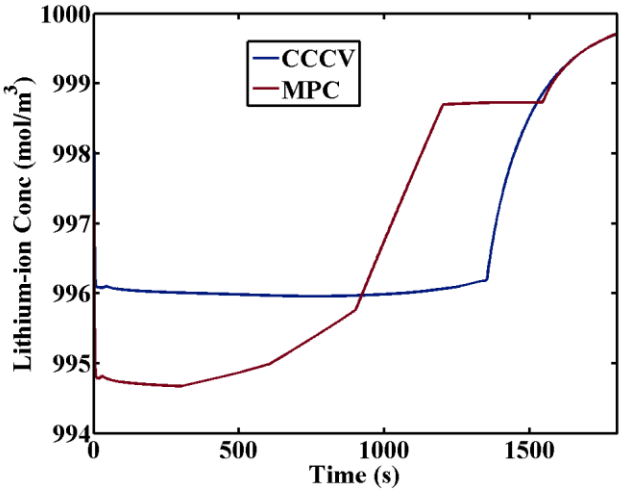

Figure 3-10: Lithium-ion concentration at the anode-separator interface

Figure 3-11 compares the battery capacity (charge stored) with time for the CC-CV and MPC cases. For the MPC case, more charge is stored at short times, compared to longer times when the battery undergoes higher fade. The CV charging phase is also shorter in the MPC case, compared to the CC-CV case. The final capacity in both cases is observed to be the same.

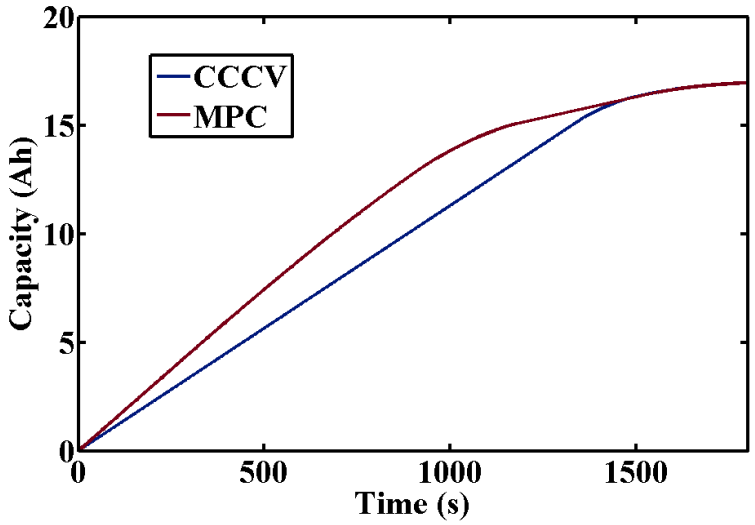

Figure 3-11: Capacity of the battery vs. time for the CC-CV and MPC profiles

Figure 3-12 and Figure 3-13 compare the overpotential vs. time, at the cathode-separator and the separator-anode interface, for the CC-CV and MPC cases. The overpotential at the cathode-separator interface are similar for both cases at most times, with the largest difference occurring between 1200 and 1400 s (Figure 3-12). In contrast, the overpotential at the anode-separator interface are quite different for most of the time, with MPC being lower than the CC-CV case at short times and towards the end (Figure 3-13). A lower overpotential leads to a decreased rate of the SEI-layer side reaction at the end, which reduces the capacity fade of the battery.

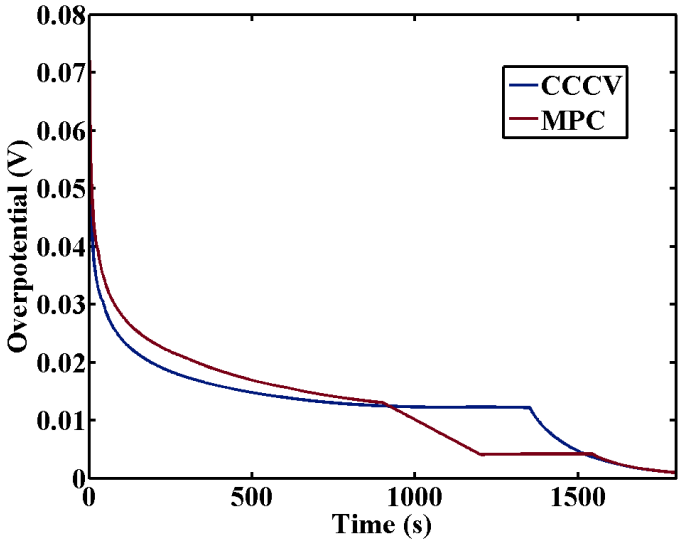

Figure 3-12: Overpotential at the cathode-separator interface for the CC-CV and MPC profiles

Figure 3-14 compares the capacity lost (Q_{SEI}) for the CC-CV and the MPC cases based on the profile of the first cycle. While the total capacity of the battery after charging remains same (Figure 3-11), the capacity lost during the charging is lower at the end of the charging for MPC than the

CC-CV case (Figure 3-14). With repeated cycling, the MPC profile continues to do a better job, resulting in a gain as is evident in Figure 3-7.

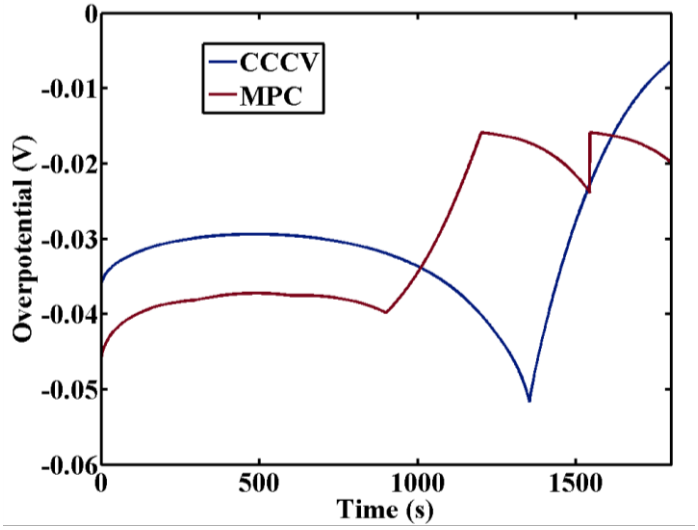

Figure 3-13: Overpotential at the anode-separator interface for the CC-CV and MPC profiles.

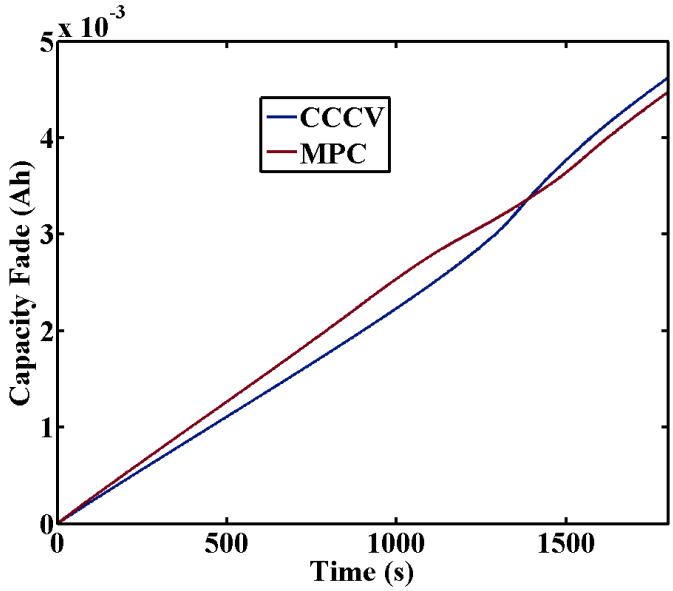

Figure 3-14: Capacity fade of the battery vs time for the first cycle for the CC-CV and MPC profiles.

The optimal profile based on the first cycle using base parameters was implemented until the battery reached its end of life. The end of life is defined as the number of cycles after which the battery reaches 80% of its initial capacity. This definition of end of life is consistent with many battery applications, including for most EV/PHEV batteries, so this definition was used to be consistent with an industry-prevalent standard practice. Without updating the control profile, we obtained in excess of 100% gain in cycle life of the cells as compared to the 2C CC-CV case (Figure 3-7). As the parameters of the battery change with aging, updating the model parameters or model with use would likely produce an even higher benefit. The relative improvement would be a function of the materials and chemistry of the battery, along with the temperature and the charging/discharging conditions in which the battery is used. Whether this benefit would be worth the extra energy costs of online optimal control calculations would depend on the specifics of the application, as discussed in the section on Optimal Model-based Control Formulations.

3.6. Conclusions

This chapter presents strategies for determining optimal charging profiles for lithium-ion batteries, to maximize their cycle life, while storing a given amount of charge in 30 minutes. Although not the main focus of this article, the modified-CVP approach implemented with the reformulated battery model is not computationally prohibitive, and could be used in real-time control. The optimal profile calculated for the first cycle of use was implemented on 16 Ah NMC cells at NREL. The optimal charging profiles were compared to the standard CC-CV charging method used for Li-ion batteries, with the CC charge rate of 2C. A gain of more than 100% in cycle life was observed using the predicted optimal charging profile.

Chapter 4: Second Derivative Methods for Optimal Control Problems

4.1. Introduction and Background

Optimal control problems defined by ordinary differential equations arise in wide range of engineering applications. Numerical methods used to discretize optimal control problems are classified as indirect methods and direct methods. In the indirect methods, the calculus of variations[60] and Pontryagin's minimum principle[61] are used to form the first order optimality conditions and then the resulting Hamiltonian boundary-value problem (HBVP) is solved to obtain an optimal solution. On the other hand, in the direct methods, the infinite dimensional optimal control problem is converted to the finite dimensional non-linear programming problem (NLP) by discretizing the governing state equations and objective functional.[62] Within direct methods, the three main methods are control vector parameterization, multiple shooting and simultaneous discretization.[63,64]

In the simultaneous approach, numerical discretization of state equations is combined with optimization; the method of discretization can include multistep or single step Runge-Kutta methods.[65] To evaluate the efficiency of discretization methods used in numerical optimization, it is necessary to study the rate of convergence of the discretized solution to the continuous solution of the optimal control problems. As far as convergence rates are concerned, previously Budak[66] and Cullum[67] studied the convergence for the solution of a discrete approximation of unconstrained optimal control problems. In these papers, authors have analyzed the rate of convergence using standard one-step and multi-step integration schemes. Using explicit Runge-Kutta schemes, William Hager[68] proved the second order convergence of controls for unconstrained optimal control

problems using both one step and multi-step discretization methods. Dontchev[69] presented Euler discretization of optimal control problems; it was the first attempt to prove the convergence of constrained optimization. Numerical results given by Hager[65] demonstrates that for the range of Runge-Kutta discretization methods even for simple optimal control problems, the convergence rate of controls are often found to be lower than states and adjoint variables. Several other notable research contributions were made in the area of order of convergence of numerical discretization methods and their implications to optical control problems. The reader is urged to refer the related work of previous researchers[70-74] in this direction. It is important to note that multistep methods cannot provide more than third order of convergence for states irrespective of the method used.[68] This means that while backward difference formulas[75] are very good for the simulation of stiff ordinary differential equations (ODEs) and differential-algebraic equations (DAEs), they are not necessarily good for direct transcription of optimal control problems. As proved by Hager[68], multistep methods perform very poorly in particular, near the boundaries where the order of convergence can be reduced to one.

Single step methods provide good convergence properties. In fact, an *s-stage* Gauss method will provide an order of *2s* for optimal control problems for the state variables at the terminal nodes. However, Gauss RK is only A-stable not L-stable and might fail for stiff problems. RadauIIA methods with *s-stages* can provide *2s-1* accuracy for the state variables at the terminal nodes, they can handle stiff problems as well. LobattoIIIA methods are A-stable and provide *2s-2* order of convergence at the terminal nodes.

A-stability: As explained by Hairer *et al.*[76], A *k-step* method is a A-stable, if all its solution tend to zero as , when the method is applied to any ODE of the form ; where is a complex constant with negative real part and its stability domain covers the entire left half of plane.

L-stability: A method is L-stable if it is A-stable and as where is the stability function of the method. It is important to note that the theory of Superconvergence gives *2s*, *2s-1* and *2s-2* order of accuracy[77] at the terminal nodes for s-stage implicit RK methods defined by Gauss, RadauIIA and LobattoIIIA methods. This is a great advantage for these methods when implemented from simulation of stiff ODEs and DAEs point of view. However, at the internal stage points (collocation points), the order of accuracy is only <=*s* and is similarly observed when applied to optimal control problems. The SDM method on the other hand avoids any internal collocation point, but needs the second derivative of the dependent variables.

To our knowledge, the application of SDM for optimal control problems has not been reported in the literature. This paper studies the convergence rates of SDM[78] and its applicability for general optimal control problems. Numerical results demonstrate that, it is possible to achieve third or fourth order convergence for states and second order convergence for controls without post-computing an estimate of controls with lesser number of discretization variables compared to implicit Runge-Kutta methods. Though the improvement of sparse solvers and optimizers help to address large number of optimization variables, SDM methods reduce the number of discretized variables, thereby reducing the RAM requirement and providing improved computational efficiency when standard non-sparse solvers are used for optimization.

4.2. Optimal Control Problem

Optimal control problems governed by differential state variables and control variables arise in a wide range of applications. If there are no path constraints on the states or control variables, and if the initial and final times are fixed, a general continuous time optimal control problem in Mayer form is defined as

$$\min_{u(t)} \phi\left(y\left(t_f\right)\right) \tag{4.1}$$

s.t.

$$\frac{dy}{dt}(t) = f\left(y(t), u(t)\right), y\left(t_0\right) = \tilde{y}_0 \tag{4.2}$$

where, $y : [t_0, t_f] \mapsto \mathbb{R}^{n_y}$ are the state variables, $u : [t_0, t_f] \mapsto \mathbb{R}^{n_u}$ are the control variables to be determined, $\phi : \mathbb{R}^{n_y} \times \mathbb{R} \mapsto \mathbb{R}^{n_y}$ is a cost functional, $f : \mathbb{R}^{n_y} \times \mathbb{R}^{n_u} \mapsto \mathbb{R}^{n_y}$ is vector form of given function, assumed to be continuously differentiable and $\tilde{y}_0 \in \mathbb{R}^{n_y}$ is the given initial condition. Equation (4.1) represents the cost functional to be minimized and equation (4.2) represents the system dynamics and initial state conditions.

Let $(y^*(t), u^*(t))$ be the continuous-time solution of the optimal control problem (4.1)-(4.2) that satisfies the following set of necessary optimality conditions.

$$\frac{dy^*}{dt}(t) = f\left(y^*(t), u^*(t)\right), y^*\left(t_0\right) = \tilde{y}_0 \tag{4.3}$$

$$\frac{d\lambda^*}{dt}(t) = -f_y\left(y^*(t), u^*(t)\right)\lambda^*(t), \lambda^*\left(t_f\right) = -\phi_y\left(y^*\left(t_f\right)\right) \tag{4.4}$$

$$0 = f_u\ y^*\ t\ , u^*\ t\ \ \lambda^*\ t \tag{4.5}$$

where, equation (4.4) is called an adjoint equation and equation (4.5) is called a gradient equation.

4.3. Direct Transcription with Second Derivative Method

With direct transcriptional approach, optimal control problems are typically first *discretized* using Euler, Trapezoidal or a range of Runge-Kutta methods on a uniform grid of *N* points covering the time interval $t \in [t_0, t_f]$ and then the resulting NLP problem is *optimized*. Such direct transcription methods, especially the range of Runge-Kutta methods have received significant attention recently.[79-81] One reason for this is the fast convergence of the solutions of discretized optimal control problem to the solution of the underlying continuous time optimal control problem. Though

IRK methods have proved to be more popular, the SDM gives an advantage over the number of discretized variables which will help to reduce RAM size and CPU time for non-sparse type of optimizers. For certain optimal control problems where system dynamics are described by stiff ODEs, IRK methods result in oscillations for the state variables at internal node points because of lower stage accuracy; in such cases SDM is competitive.

To describe the SDM method, the fourth order single step formula is given as:

$$y_{n+1} = y_n + \frac{h}{2}(f_n + f_{n+1}) + \frac{h^2}{12}(g_n - g_{n+1}); n = 1...N-1 \tag{4.6}$$

where, f_n and f_{n+1}, are the discrete approximations of states, g_n and g_{n+1}, represent the analytical differentiation of f at grid points t_n and t_{n+1} respectively. Equation (4.6) provides a fourth order accurate integration scheme. The scheme is A-stable and not L-stable in a region ϕ of the $z-$plane with the stability function given by $\phi(z) = \frac{(1+z/2+z^2/12)}{(1-z/2+z^2/12)}$. The third order SDM formula[78] is written as

$$y_{n+1} = y_n + \frac{h}{3}(2f_{n+1} + f_n) - \frac{h^2}{6}(g_{n+1}); n = 1...N-1 \tag{4.7}$$

Equation (4.7) is accurate to the third order and is both A-stable and L-stable.

For the direct transcription of optimal control problem, we discretized the optimal control problem (4.1)-(4.2) using SDM over a finite horizon $t \in [t_o, t_f]$ with a uniform grid of $N-1$ intervals and initial conditions. Using SDM, the state equation (4.2) is approximated by equation (4.6); it will also involve the derivative of u, the control variable. This cannot be left as an additional optimization variable as it will lead to oscillations. For the SDM method, the differentiation of control vector u

is approximated by its finite difference approximation i.e. $\frac{du}{dt} = up_i = (u_{i+1} - u_i)/h; h = t_f/(N-1)$ which leads to the following SDM discretization of (4.1)-(4.2).

$$\min_{u_n, y_n, y_f} \phi(y_f) \tag{4.8}$$

$$\begin{aligned} &s.t. \\ &y_{n+1} - y_n - \frac{h}{2}\left[f_n + f_{n+1}\right] + \frac{h^2}{12}\left[g_n - g_{n+1}\right] = 0; n = 1....N-1 \end{aligned} \tag{4.9}$$

The optimality conditions for control problem (4.8)-(4.9) are obtained by forming the Lagrangian function, where we assumed $\frac{du}{dt} = up$ as a free variable.

$$L\left(y_n, u_n, y_f, \lambda_n, \nu_n, up_n\right) = \phi\left(y_f\right) + \sum_{n=1}^{N-1} \lambda_n^T \left\{ \begin{array}{l} y_{n+1} - y_n - \frac{h}{2}\left[f\left(y_n, u_n\right) + f\left(y_{n+1}, u_{n+1}\right)\right] \\ -\frac{h^2}{12}\left[g\left(y_n, u_n, up_n\right) - g\left(y_{n+1}, u_{n+1}, up_{n+1}\right)\right] \end{array} \right\} + \sum_{n=1}^{N-1} \nu_n^T \left(y_n - y_0\right) \tag{4.10}$$

The necessary conditions of optimality can be written as:

$$\begin{aligned} &\nabla_{\lambda_n} L = \left[y_{n+1} - y_n - \frac{h}{2}\left[f\left(y_n, u_n\right) + f\left(y_{n+1}, u_{n+1}\right)\right] - \frac{h^2}{12}\left[g\left(y_n, u_n, up_n\right) - g\left(y_{n+1}, u_{n+1}, up_{n+1}\right)\right]\right] \\ &= 0; n = 1...N-1; \end{aligned} \tag{4.11}$$

$$\begin{aligned} &\nabla_{u_n} L = \lambda_n \left\{-\frac{h}{2} f_u\left(y_n, u_n\right) - \frac{h^2}{12} g_u\left(y_n, u_n, up_n\right)\right\} + \lambda_{n-1}\left\{-\frac{h}{2} f_u\left(y_{n+1}, u_{n+1}\right) + \frac{h^2}{12} g_u\left(y_{n+1}, u_{n+1}, up_{n+1}\right)\right\} \\ &= 0; n = 1...N-1; \end{aligned} \tag{4.12}$$

$$\begin{aligned} &\nabla_{y_n} L = \lambda_n \left\{-1 - \frac{h}{2} f_y\left(y_n, u_n\right) - \frac{h^2}{12} g_y\left(y_n, u_n, up_n\right)\right\} + \\ &\lambda_{n-1}\left\{1 - \frac{h}{2} f_y\left(y_{n+1}, u_{n+1}\right) + \frac{h^2}{12} g_y\left(y_{n+1}, u_{n+1}, up_{n+1}\right)\right\} = 0; n = 1...N-1; \end{aligned} \tag{4.13}$$

$$\nabla_{\nu_n} L = \left(y_n - y_0\right) = 0; n = 1....N-1 \tag{4.14}$$

$$\nabla_{up_n} L = \lambda_n \left\{-\frac{h^2}{12} g_{up}\left(y_n, u_n, up_n\right)\right\} + \lambda_{n-1}\left\{\frac{h^2}{12} g_{up}\left(y_{n+1}, u_{n+1}, up_{n+1}\right)\right\} = 0; n = 1..N-1 \tag{4.15}$$

$$\nabla_{y_f} L = \phi_y\left(y_f\right) + \lambda_{N-1}\left\{1 - \frac{h}{2} f_y\left(y_f, u_f\right) + \frac{h^2}{12} g_y\left(y_f, u_f\right)\right\} = 0 \tag{4.16}$$

$$\nabla_{u_f} L = \lambda_{N-1}\left\{-\frac{h}{2} f_u\left(y_f, u_f\right) + \frac{h^2}{12} g_u\left(y_f, u_f\right)\right\} = 0 \tag{4.17}$$

After the earlier attempts in the seventies, SDM methods lost out to IRK based on Gauss, Lobatto, and Radau type families for simulation of stiff ODEs and DAEs because of the need to find second derivatives. This manuscript suggests for direct transcription of optimal control problems; SDM methods can be competitive. To make our discussion more concrete, we have discussed some optimal control examples and the order of convergence obtained using SDM in the next section, and it is compared with fourth order 3-stage LobattoIIIA and third order 2-stage RadauIIA as implicit Runge-Kutta methods.[79,80] In this study, we refer Second Derivative Method as SDM, fourth order, 3-stage LobattoIIIA method as LobattoIIIA, fourth order, 3-stage LobattoIIIA with midpoint approximation for control $Uint = \left(u_1 + u_2\right)/2$ as LobattoIIIA*, third order, 2-stage RadauIIA as RadauIIA and third order, 2-stage RadauIIA with midpoint approximation for control $Uint = \left(2/3u_1 + 1/3u_2\right)$ as RadauIIA*.

4.4. Numerical examples and results

This section describes the order of convergence obtained using SDM on some of the typical optimal control examples illustrated in literature. The order of convergence obtained using SDM is compared with LobattoIIIA, RadauIIA, LobattoIIIA* and RadauIIA* implicit Runge-Kutta discretization methods.

Problem 1- P1: The first problem considered is

$$\begin{aligned} &\min_u -y\left(t_f\right) \\ &\dot{y}\left(t\right) = -y\left(t\right) + y\left(t\right)u\left(t\right) - u\left(t\right)^2; t \in \left[0,5\right], y\left(0\right) = 1. \end{aligned} \tag{4.18}$$

The analytical solution of state and control is given as

$$y^*\left(t\right) = \frac{4}{\left(1+3e^t\right)}; u^*\left(t\right) = \frac{y^*\left(t\right)}{2} \tag{4.19}$$

The value of optimal cost can be computed as -0.008963796.

We solved this problem using direct transcription approach on uniform grids of N points with $N-1$ intervals. A discrete solution of P1 is obtained using 4th order SDM (equation (4.6)), LobattoIIIA and RadauIIA discretization methods. The discrete solutions obtained using SDM with $N=11$ for state and control is compared with the analytical solution. Figure 4-1(a-b) shows the optimal solution y^* and u^* of problem P1.

From Figure 4-1, it is observed that, for problem P1 the discrete optimal solution obtained using SDM for state and controls is much closer to that of analytical solution, LobattoIIIA and RadauIIA discretization methods also reveals the same nature and no oscillations are observed for internal collocation points.

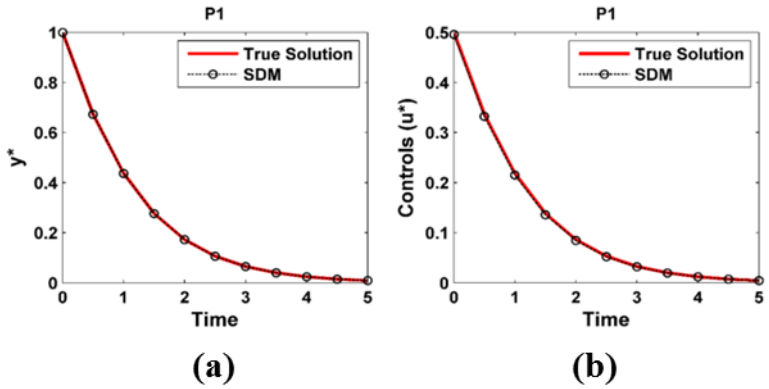

Figure 4-1: Graph of y* and u* for P1 with N=11

The error, in numerical analysis is generally measured in supremum (sup) norm which is computed as $-\log_2$ of the infinity norm error. Even for simple linear control problems, the controls are often found to be less accurate than the states and objective functional. To observe and compare the order of convergence of discretization methods under study, the sup norm error for optimal discrete control is plotted versus $-\log_2(h)$ with h being the step length, for the values of $h=1/5,1/10,1/20,1/40..$ as shown in Figure 4-2. The slope of the line in Figure 4-2 is the convergence

rate. The numerical results for sup norm error and maximum error for problem P1 are given in Table 4-1 and Table 4-2.

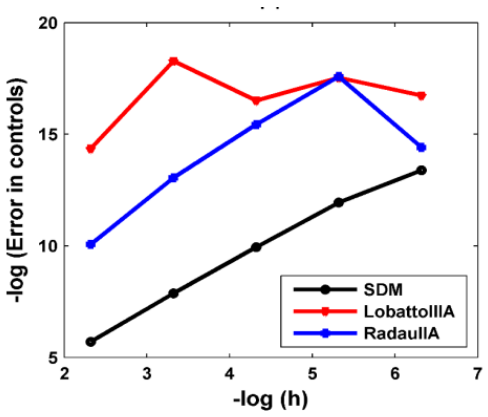

Figure 4-2: Maximum norm error in controls (u*) for P1

From numerical results, we observed for SDM 4th order convergence for states and 2nd order convergence for controls for LobattoIIIA 4th order convergence in states as well as in controls while, RadauIIA gives 3rd order convergence in state and controls.

Table 4-1: $-\log_2$ of Infinity Norm error in P1

N	$\|y^* - y_N\|$			$\|u^* - u_N\|$		
	SDM	LobattoIIIA	Radau IIA	SDM	Lobatto IIIA	Radau IIA
6	11.810	13.3537	9.0657	5.700	14.351	10.066
11	15.914	17.3600	11.9822	7.867	18.282	13.046
21	19.937	21.3447	14.9193	9.940	16.509	15.434
41	23.922	25.3343	17.8924	11.92	17.536	17.581
81	27.914	29.3214	20.9021	13.36	16.733	14.411
Order	4	4	3	2	4	3

Table 4-2: Maximum error in outputs of P1

N	$\|y^* - y_N\|$			$\|u^* - u_N\|$		
	SDM	Lobatto IIIA	Radau IIA	SDM	LobattoIIIA	Radau IIA
6	2.77e-4	9.55e-5	1.86e-3	1.92e-2	4.78e-5	9.32e-4
11	1.61e-5	5.94e-6	2.47e-4	4.28e-3	3.13e-6	1.18e-4
21	9.97e-7	3.75e-7	3.22e-5	1.01e-3	1.05e-5	2.25e-5
41	6.29e-8	2.36e-8	4.10e-6	2.54e-4	5.26e-6	5.09e-6

Problem 2- P2: This example is adapted from Anna Engelsone *et. al.*,[70]

$$\begin{aligned} &\min_u \int_0^1 \left[\frac{5}{4} y(t)^2 + y(t)u(t) + u(t)^2 \right] dt \\ &\dot{y}(t) = \frac{1}{2} y(t) + u(t); t \in [0,1], y(0) = 1. \end{aligned} \tag{4.20}$$

The analytical solution of state and control is given as

$$y^*(t) = \frac{\cosh(1-t)}{\cosh(1)}; u^*(t) = \frac{-(\tanh(1-t) + 0.5)\cosh(1-t)}{\cosh(1)} \tag{4.21}$$

The value of optimal cost is 0.7615941557. This example was chosen as most direct transcription approaches based on multistep methods exhibit order reduction and oscillations in the optimal solution. As explained in [9], IRK methods prove to be better compared to multistep methods (but still exhibit order reduction and oscillation for the control variable). We have attempted this problem using 4th order SDM (equation (4.6)) and obtained the optimal solution by discretizing on niform grids of N points with $N-1$intervals. The discrete solution obtained with $N=11$ for state and control is compared with the analytical solution. Figure 4-3(a-b) shows the optimal solution of P2. From Figure 4-3, it is observed that, the discrete optimal solution obtained using SDM for state and

controls closely match with the analytical solution. The optimal solution obtained using LobattoIIIA and RadauIIA discretization methods also appear very similar.

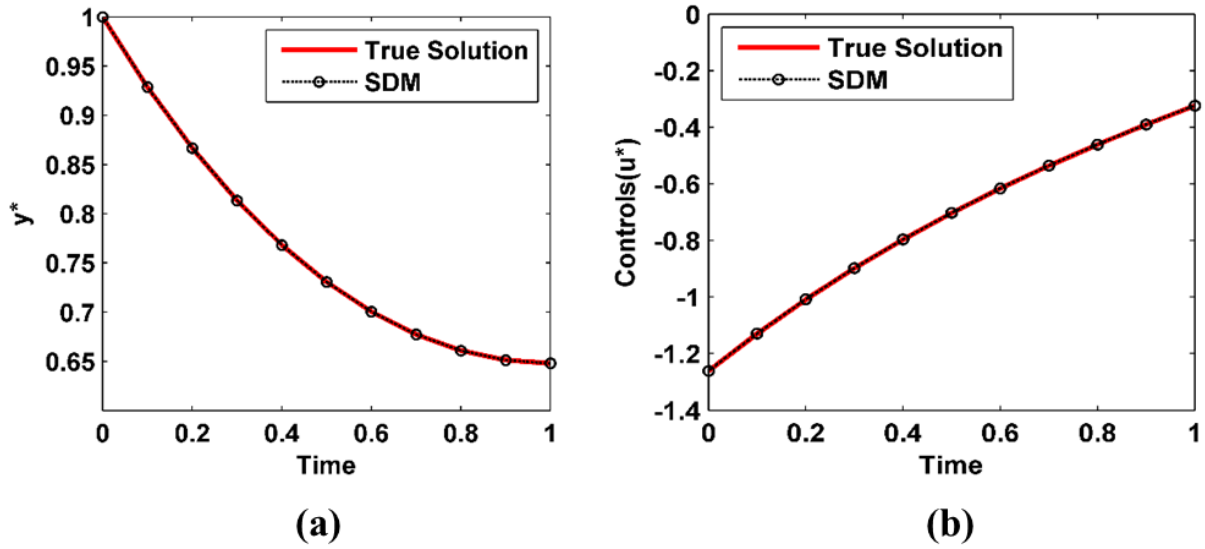

Figure 4-3: Graph of (a) y* and (b) u* for P2

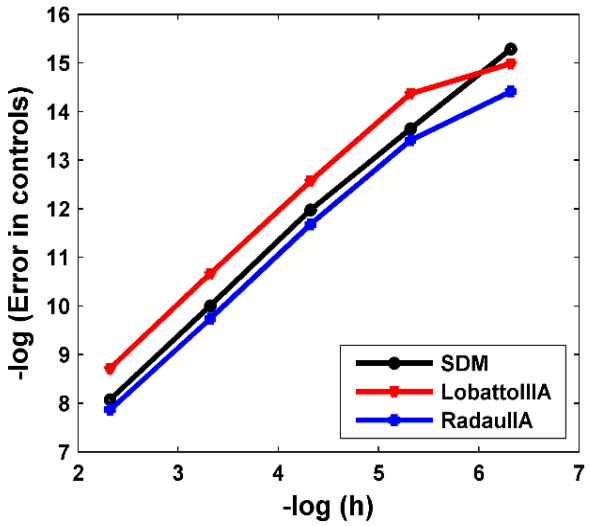

Figure 4-4: Maximum norm error in controls (u*) for P2

The sup norm error for optimal discrete control is plotted versus $-\log_2(h)$ as shown in Figure 4-4 and the numerical results for sup norm error and maximum error for P2 are tabulated in Table 4-3 and Table 4-4.

Table 4-3: -$\log_2$ of Infinity Norm error in P2

N	$\|y^* - y_N\|$			$\|u^* - u_N\|$		
	SDM	LobattoIIIA	Radau IIA	SDM	LobattoIIIA	RadauIIA
6	14.9523	17.6910	14.1420	8.0753	8.7187	7.8667
11	18.6012	21.5501	17.1526	10.006	10.6698	9.7413
21	20.4297	22.2099	20.2914	11.979	12.5704	11.680
41	20.8025	22.4036	21.1629	13.651	14.3704	13.409
81	21.0389	21.0949	20.1710	15.283	14.9897	14.413
Order	4	4	3	2	2	2

Table 4-4: Maximum error in outputs of P2

N	$\|y^* - y_N\|$			$\|u^* - u_N\|$		
	SDM	LobattoIIIA	RadauIIA	SDM	LobattoIIA	RadauIIA
6	3.15e-5	4.72e-6	5.53e-5	3.70e-3	2.37e-3	4.28e-3
11	2.51e-6	3.25e-7	6.86e-6	9.72e-4	6.13e-4	1.16e-3
21	7.08e-7	2.06e-7	7.79e-7	2.38e-4	1.63e-4	3.04e-4
41	5.46e-7	1.80e-7	4.25e-7	7.77e-5	4.70e-5	9.19e-5

From numerical results of problem P2, we observed 4^{th} order convergence for states and 2^{nd} order convergence for controls with SDM and LobattoIIIA methods, while, RadauIIA gives 3^{rd} order

convergence in state and 2nd order convergence in controls. But, even though the order of convergence of controls is the same for all three methods, SDM gives an advantage over the other two discretization methods, as it uses a lesser number of optimization variables and all the variables are of same accuracy unlike IRK methods in which internal collocation/stage variables are less accurate. This example confirms the effectiveness and benefit of the SDM approach of numerical discretization over IRK methods for optimal control problems.

Problem 3- P3: A control problem is formulated from a stiff BVP. The second order problem is converted to a first order problem (by integration) with an arbitrary constant of integration, *k*.

$$\begin{aligned} &\min_{u} \int_{0}^{1} (u) dt \\ &s.t. \\ &\dot{y}_1(t) = u(t)\, y_1(t) + k; t \in [0,1] \\ &0 \ll u \ll Pe(=100) \;\; \& \;\; y_1(0) = 1 \end{aligned} \tag{4.22}$$

The analytical solution for problem P3 is given by:

$$\begin{aligned} &y_1^*(t) = \frac{e^{Pe}}{-1+e^{Pe}} - \frac{e^{(Pe*t)}}{-1+e^{Pe}} \\ &u^*(t) = Pe(const.) \end{aligned} \tag{4.23}$$

The value of optimal cost is Pe (Peclet number) over a time. The optimal solution of P3 for state and controls is obtained with $N = 21$ using 4th order SDM, LobattoIIIA* and RadauIIA methods. For discrete controls, we observed the same nature and order of convergence for all three discretization methods but for optimal state, we witnessed oscillations at mesh points for LobattoIIIA* and sustained oscillations at internal collocation points with RadauIIA methods, whereas RadauIIA* did not converge. The optimal solution for state y_1^* is plotted versus time as shown in Figure 4-5. The sup norm error and order of convergence for optimal state is given in Table 4-5.

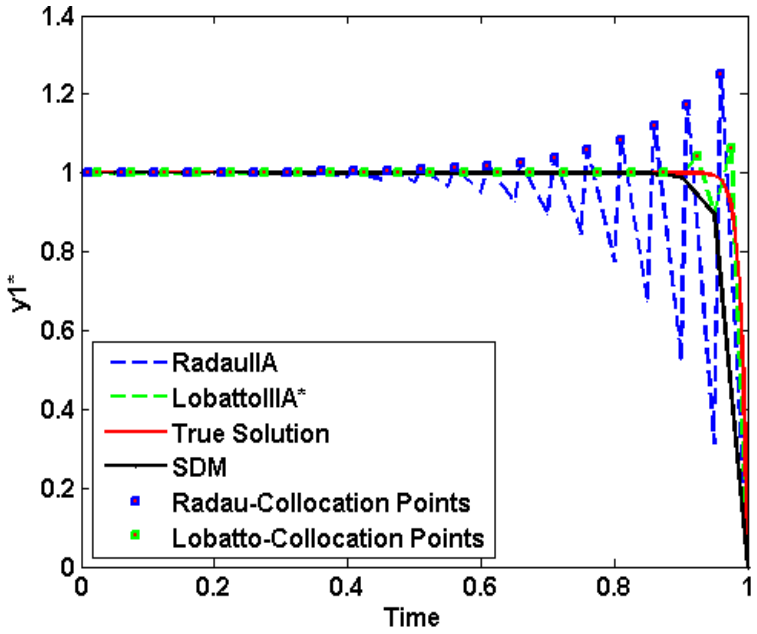

Figure 4-5: Graph of optimal state for test problem P3 for Pe=100, N=21

Table 4-5: -$\log_2$ of Infinity Norm error in optimal discrete state of P3

N	$\|y^* - y_N\|$		
	SDM	LobattoIIIA*	RadauIIA
11	1.7260	1.7262	0.0026
21	3.3549	3.3550	0.5551
41	5.9968	5.9968	3.0296
81	9.5554	9.5556	6.0621
161	13.6522	13.6520	9.4046
Order	4	4	3

It is important to note that if bounds of 0...1 (physically meaningful bound) were provided for this problem, only SDM method works and other methods fail because of the observed oscillations for internal stages. In addition, for complicated large scale DAE system, one might encounter 'square root' or other terms which make the equation undefined outside a meaningful range for concentration or mole fraction. In these cases, SDM guarantees same order of accuracy for all the discretized state variables, and converges. For example, in P3 if there was an additional variable defined as $\frac{dz}{dt} = \left(\sqrt{1 - y_1(t)}\right) u(t)$, then SDM will work and other methods may fail.

The aim of this work is to examine the performance of SDM for order of convergence applied to optimal control problems. From computational results, we have seen that for the optimal control problems that are easily solved SDM and LobattoIIIA give fourth order convergence for states and second order convergence for controls, whereas RadauIIA gives third order convergence in states and second order convergence in controls as expected. Though the order of convergence of controls is same for LobattoIIIA, SDM and RadauIIA methods, SDM gives an advantage over the number of discretized variables which will help to reduce RAM size and CPU time for non-sparse type of optimizers.

In the case of models that are known to cause order reduction in typical IRK methods; with SDM, it is possible to achieve fourth or third order convergence in states and second order convergence in controls. For certain optimal control problems where system dynamics are described by stiff ODEs, IRK methods have state variables oscillate at internal node points because of lower stage accuracy; in such cases SDM is competitive. For stiff BVP type problems with terminal constraints requiring exhibiting boundary layers (requiring large number of nodes), LobattoIIIA and RadauIIA oscillate for state variables while SDM has no oscillations and gives fourth order convergence for states for the same number of node points.

In particular, for regular non-sparse optimizers, SDM is more useful and efficient because of the lower number of optimization variables.

Current work includes applying these methods for index-1 and higher orders DAEs optimal control problems. For index-1 DAEs, without differentiating algebraic constraints, by using approximations as used for control variable in this paper, one can obtain second order accuracy for the algebraic variables. By adding derivatives of algebraic constraints as additional equations, and including time derivatives for algebraic variables as additional decision variables, one can obtain 4th order accuracy for algebraic variables.

Chapter 5: A Look at the Battery Impedance

5.1. Introduction

Electrochemical impedance spectroscopy (EIS) has been widely used to study the linear dynamics of many electrochemical systems, including Li-ion batteries.[82-85] Most physical and chemical processes in an electrochemical system possess distinct characteristic time constants, enabling EIS to distinguish these processes by their frequency response. The dynamics of the porous electrodes used inside most commercially available Li-ion batteries are governed by the conduction and mass transfer in the solid and the electrolyte phase, and electro-chemical kinetics at the solid-electrolyte interface. Because EIS is able to separate processes by their time-scales, it is often possible to see changes in each battery electrode as well as the degradation that leads to capacity fade of the batteries.[86-89]

Equivalent circuits are the most commonly used models to study the impedance response of batteries; however, the use of networks of circuit elements can suffer from a lack of physical interpretability and model degeneracy.[90] Though much less used, physics-based models can provide more direct insight into the impedance response of a battery. Mathematically, physics-based impedance models are transformed from the time-domain to the frequency-domain by assuming a steady-periodic response, thereby eliminating time as an independent variable.[91] Most rigorous physics-based models for the impedance of a Li-ion battery employ a numerical scheme to solve the resulting equations.[91-93] The resulting equations are computationally expensive to solve, and this reduces their usefulness for multi-parameter optimization and analysis of different mechanisms from experimental impedance data.

Part of the computational complexity in solving these models arises from the coupling between mass transfer, kinetics, and thermodynamics across the thickness of the electrode to the solid phase diffusion inside the solid particles. Though never explored with frequency-domain physics-based model formulations, there have been significant advances to accelerate time-domain computations of discharge-charge curves using physics-based battery models.[39,41,53,94-96] One strategy for reducing the simulation time has been approximating solid phase diffusion using various polynomial approximations.[97-100] Approximations were typically applied that reduced the number of state variables, along with the computational time. While Duhamel's superposition method reduces the number of state variables (for example, it removes the radial coordinate '*r*' from the model simulation), it is not ideal for reducing the computational time, as adaptive solvers for integrating the discretized system of differential algebraic equations (DAEs) $\left(\frac{dy}{dt} = f\left(y,z\right), 0 = g\left(y,z\right)\right)$ cannot be used. Even though we have applied polynomial approximations for concentration in the solid phase for our past work,[97] these approximations are not needed for AC impedance simulation as the radial dependence can be removed by solving analytically for the solid phase impedance response.

Closed-form analytical solutions of the impedance have been derived for certain cases, but these are only valid under specific design considerations or limited operating conditions. For example, an analytical solution for the impedance response of porous intercalation electrodes in the absence of solid-phase diffusion limitations has been presented. [101] Similarly, analytical solutions have been derived for estimating physical properties of non-insertion porous electrodes in symmetric cells, and of electrodes without electrolyte-phase diffusion limitations.[102,103] Symbolic closed-form solutions have also been developed for predicting the impedance response in planar

electrodes, due to diffusion process.[104] Moreover, a general analytical expression for the impedance response for Li-ion cells, accounting for the reaction kinetics at the interface, along with potential distribution and mass transport in the solid and electrolyte phase has also been proposed. [105,106] However, most of these methods do not account for the entire battery physics, and others numerically fail for high frequencies, unless very high numbers of polynomial coefficient terms are used. Also, using the analytical solution requires operation in complex domain and separating the real and imaginary parts of impedance in parametric form is challenging, which limits its use for real-time simulation and estimation.

Here, we propose a computationally efficient way to solve the impedance equations for the pseudo-2 dimensional (P2D) model by first applying a coordinate transformation, then orthogonal collocation to represent the model equations. After applying a time periodic solution form,[91] the governing equations for the original P2D model are converted to partial differential equations in the frequency domain, where the independent variables are *x* (transverse spatial coordinate across the cell), and *r* (local radial coordinate for the spherical electrode particles). The radial dependence of the solid phase concentrations can be solved analytically, even for the cases in which solid phase diffusion coefficient is dependent on the concentration inside the solid particle, as only the linear terms are considered for the linear AC impedance models. Once the analytical solution is available, the dependency in radial coordinate '*r*' is removed and the model just becomes a boundary value problem (BVP) in the spatial coordinate '*x'*, with corresponding boundary conditions for each variable. Solutions to the dependent variables such as the complex oscillating concentrations and potentials in the system are parameterized in frequency domain, along with the physicochemical and geometric properties and electrodes, electrolyte, and cell configuration. The details for obtaining the analytical solution for the solid-phase concentration equations, are given in the

appendix. The resulting equations can be solved using finite difference method, or using finite element method, in a computational platform such as COMSOL Multiphysics. [107]

To simplify the computation of the BVPs, we apply a coordinate transformation, to rescale the spatial coordinate, as described in more detail below.

5.2. Coordinate Transformation

A Li-ion battery consists of cathode, separator and anode. The model equations must be solved in each region simultaneously, with the boundary conditions at the interfaces coupling the variables in each region. As proposed earlier by Northrop *et al.*, to reduce the required computation, each region is rescaled to be solved within a spatial domain from .[41] The spatial coordinate is rescaled as:

$$X = \frac{x}{l_p}, \quad 0 \le x \le l_p \tag{5.1}$$

$$X = \frac{x - l_p}{l_s}, \quad l_p \le x \le l_p + l_s \tag{5.2}$$

$$X = \frac{x - l_p - l_s}{l_n}, \quad l_p + l_s \le x \le l_p + l_s + l_n \tag{5.3}$$

The resulting transformed governing equations for the model along with boundary conditions, are given in Table 5-1 and Table 5-2.

(*u'* represents the real-part of the variable *u*, and *u''* represents the imaginary part of the variable *u*)

Table 5-1: Equations for the P2D impedance model for the full cell

Governing Equation	Boundary Conditions
Negative Electrode	
$-\varepsilon_n c''_n \omega = \frac{1}{l_n}\frac{\partial}{\partial X}\left[\frac{D_{\text{eff,n}}}{l_n}\frac{\partial c'_n}{\partial X}\right] + a_n(1-t_+)\left(j'_n + j'_{\text{dl,n}}\right)$ $\varepsilon_n c'_n \omega = \frac{1}{l_n}\frac{\partial}{\partial X}\left[\frac{D_{\text{eff,n}}}{l_n}\frac{\partial c''_n}{\partial X}\right] + a_n(1-t_+)\left(j''_n + j''_{\text{dl,n}}\right)$	$\frac{\partial c'_n}{\partial X}\Big\|_{X=0} = 0$ $\frac{\partial c''_n}{\partial X}\Big\|_{X=0} = 0$ $\frac{-D_{\text{eff,n}}}{l_n}\frac{\partial c'_n}{\partial X}\Big\|_{X=1} = \frac{-D_{\text{eff,s}}}{l_s}\frac{\partial c'_s}{\partial X}\Big\|_{X=0}$ $\frac{-D_{\text{eff,n}}}{l_n}\frac{\partial c''_n}{\partial X}\Big\|_{X=1} = \frac{-D_{\text{eff,s}}}{l_s}\frac{\partial c''_s}{\partial X}\Big\|_{X=0}$
$\frac{1}{l_n}\frac{\partial}{\partial X}\left[\frac{-\sigma_{\text{eff,n}}}{l_n}\left(\frac{\partial \Phi'_{1,n}}{\partial X}\right)\right] - \frac{1}{l_n}\frac{\partial}{\partial X}\left[\frac{\kappa_{\text{eff,n}}}{l_n}\left(\frac{\partial \Phi'_{2,n}}{\partial X}\right)\right]$ $+\frac{1}{l_n}\frac{\partial}{\partial X}\left[\frac{2\kappa_{\text{eff,n}}RT}{Fc_0}\frac{(1-t_+)}{l_n}\left(\frac{\partial c'_n}{\partial X}\right)\right] = 0$ $\frac{1}{l_n}\frac{\partial}{\partial X}\left[\frac{-\sigma_{\text{eff,n}}}{l_n}\left(\frac{\partial \Phi''_{1,n}}{\partial X}\right)\right] - \frac{1}{l_n}\frac{\partial}{\partial X}\left[\frac{\kappa_{\text{eff,n}}}{l_n}\left(\frac{\partial \Phi''_{2,n}}{\partial X}\right)\right]$ $+\frac{1}{l_n}\frac{\partial}{\partial X}\left[\frac{2\kappa_{\text{eff,n}}RT}{Fc_0}\frac{(1-t_+)}{l_n}\left(\frac{\partial c''_n}{\partial X}\right)\right] = 0$	$\Phi'_{2,n}\Big\|_{X=0} = 0$ $\Phi''_{2,n}\Big\|_{X=0} = 0$ $\frac{-\kappa_{\text{eff,n}}}{l_n}\frac{\partial \Phi'_{2,n}}{\partial X}\Big\|_{X=1} = \frac{-\kappa_{\text{eff,s}}}{l_s}\frac{\partial \Phi'_{2,s}}{\partial X}\Big\|_{X=0}$ $\frac{-\kappa_{\text{eff,n}}}{l_n}\frac{\partial \Phi''_{2,n}}{\partial X}\Big\|_{X=1} = \frac{-\kappa_{\text{eff,s}}}{l_s}\frac{\partial \Phi''_{2,s}}{\partial X}\Big\|_{X=0}$

$\frac{1}{l_n}\frac{\partial}{\partial X}\left[\frac{\sigma_{\text{eff,n}}}{l_n}\frac{\partial}{\partial X}\Phi'_{1,n}\right]=a_nF\left(j'_n+j'_{dl,n}\right)$ $\frac{1}{l_n}\frac{\partial}{\partial X}\left[\frac{\sigma_{\text{eff,n}}}{l_n}\frac{\partial}{\partial X}\Phi''_{1,n}\right]=a_nF\left(j''_n+j''_{dl,n}\right)$	$\left(\frac{1}{l_n}\frac{\partial\Phi'_{1,n}}{\partial X}\right)\Big\|_{X=0}=-\frac{I}{\sigma_{eff,n}}$ $\left(\frac{1}{l_n}\frac{\partial\Phi''_{1,n}}{\partial X}\right)\Big\|_{X=0}=0$ $\frac{\partial\Phi'_{1,n}}{\partial X}\|_{X=1}=0$ $\frac{\partial\Phi''_{1,n}}{\partial X}\|_{X=1}=0$
$-\omega c_n^{s}{}'' = \frac{1}{r^2}\frac{\partial}{\partial r}\left[r^2D_n^s\frac{\partial c_n^{s}{}'}{\partial r}\right]$ $\omega c_n^{s}{}' = \frac{1}{r^2}\frac{\partial}{\partial r}\left[r^2D_n^s\frac{\partial c_n^{s}{}''}{\partial r}\right]$	$\left.\frac{\partial c_n^{s}{}'}{\partial r}\right\|_{r=0}=0$ $\left.\frac{\partial c_n^{s}{}''}{\partial r}\right\|_{r=0}=0$ $\left.-D_n^s\frac{\partial c_n^{s}{}'}{\partial r}\right\|_{r=R_n}=j'_n$ $\left.-D_n^s\frac{\partial c_n^{s}{}''}{\partial r}\right\|_{r=R_n}=j''_n$
Separator	
$-\varepsilon_s c''_s\,\omega=\frac{1}{l_s}\frac{\partial}{\partial X}\left[\frac{D_{\text{eff,s}}}{l_s}\frac{\partial c'_s}{\partial X}\right]$ $\varepsilon_s c'_s\,\omega=\frac{1}{l_s}\frac{\partial}{\partial X}\left[\frac{D_{\text{eff,s}}}{l_s}\frac{\partial c''_s}{\partial X}\right]$	$c'_n\|_{X=1}=c'_s\|_{X=0}$ $c''_n\|_{X=1}=c''_s\|_{X=0}$ $c'_s\|_{X=1}=c'_p\|_{X=0}$ $c''_s\|_{X=1}=c''_p\|_{X=0}$
$-\frac{1}{l_s}\frac{\partial}{\partial X}\left[\frac{\kappa_{\text{eff,s}}}{l_s}\left(\frac{\partial\Phi'_{2,s}}{\partial X}\right)\right]+\frac{1}{l_s}\frac{\partial}{\partial X}\left[\frac{2\kappa_{\text{eff,s}}RT}{Fc_0}\frac{(1-t_+)}{l_s}\left(\frac{\partial c'_s}{\partial X}\right)\right]=0$ $-\frac{1}{l_s}\frac{\partial}{\partial X}\left[\frac{\kappa_{\text{eff,s}}}{l_s}\left(\frac{\partial\Phi''_{2,s}}{\partial X}\right)\right]+\frac{1}{l_s}\frac{\partial}{\partial X}\left[\frac{2\kappa_{\text{eff,s}}RT}{Fc_0}\frac{(1-t_+)}{l_s}\left(\frac{\partial c''_s}{\partial X}\right)\right]=0$	$\Phi'_{2,n}\|_{X=1}=\Phi'_{2,s}\|_{X=0}$ $\Phi''_{2,n}\|_{X=1}=\Phi''_{2,s}\|_{X=0}$ $\Phi'_{2,s}\|_{X=1}=\Phi'_{2,p}\|_{X=0}$ $\Phi''_{2,s}\|_{X=1}=\Phi''_{2,p}\|_{X=0}$
Positive Electrode	

$$-\varepsilon_p c''_p\,\omega = \frac{1}{l_p}\frac{\partial}{\partial X}\left[\frac{D_{\text{eff,p}}}{l_p}\frac{\partial c'_p}{\partial X}\right] + a_p\left(1-t_+\right)\left(j'_p + j'_{\text{dl,p}}\right)$$ $$\varepsilon_p c'_p\,\omega = \frac{1}{l_p}\frac{\partial}{\partial X}\left[\frac{D_{\text{eff,p}}}{l_p}\frac{\partial c''_p}{\partial X}\right] + a_p\left(1-t_+\right)\left(j''_p + j''_{\text{dl,p}}\right)$$	$$\frac{-D_{\text{eff,s}}}{l_s}\frac{\partial c'_s}{\partial X}\Big|_{X=1} = \frac{-D_{\text{eff,p}}}{l_p}\frac{\partial c'_p}{\partial X}\Big|_{X=0}$$ $$\frac{-D_{\text{eff,s}}}{l_s}\frac{\partial c''_s}{\partial X}\Big|_{X=1} = \frac{-D_{\text{eff,p}}}{l_p}\frac{\partial c''_p}{\partial X}\Big|_{X=0}$$ $$\frac{\partial c'_p}{\partial X}\Big|_{X=1} = 0$$ $$\frac{\partial c''_p}{\partial X}\Big|_{X=1} = 0$$
$$\frac{1}{l_p}\frac{\partial}{\partial X}\left[\frac{-\sigma_{\text{eff,p}}}{l_p}\left(\frac{\partial \Phi'_{1,p}}{\partial X}\right)\right] - \frac{1}{l_p}\frac{\partial}{\partial X}\left[\frac{\kappa_{\text{eff,p}}}{l_p}\left(\frac{\partial \Phi'_{2,p}}{\partial X}\right)\right]$$ $$+\frac{1}{l_p}\frac{\partial}{\partial X}\left[\frac{2\kappa_{\text{eff,p}}RT}{Fc_0}\frac{\left(1-t_+\right)}{l_p}\left(\frac{\partial c'_p}{\partial X}\right)\right] = 0$$ $$\frac{1}{l_p}\frac{\partial}{\partial X}\left[\frac{-\sigma_{\text{eff,p}}}{l_p}\left(\frac{\partial \Phi''_{1,p}}{\partial X}\right)\right] - \frac{1}{l_p}\frac{\partial}{\partial X}\left[\frac{\kappa_{\text{eff,p}}}{l_p}\left(\frac{\partial \Phi''_{2,p}}{\partial X}\right)\right]$$ $$+\frac{1}{l_p}\frac{\partial}{\partial X}\left[\frac{2\kappa_{\text{eff,p}}RT}{Fc_0}\frac{\left(1-t_+\right)}{l_p}\left(\frac{\partial c''_p}{\partial X}\right)\right] = 0$$	$$\frac{-\kappa_{\text{eff,s}}}{l_s}\frac{\partial \Phi'_{2,s}}{\partial X}\Big|_{X=1} = \frac{-\kappa_{\text{eff,p}}}{l_p}\frac{\partial \Phi'_{2,p}}{\partial X}\Big|_{X=0}$$ $$\frac{-\kappa_{\text{eff,s}}}{l_s}\frac{\partial \Phi''_{2,s}}{\partial X}\Big|_{X=1} = \frac{-\kappa_{\text{eff,p}}}{l_p}\frac{\partial \Phi''_{2,p}}{\partial X}\Big|_{X=0}$$ $$\frac{\partial \Phi'_{2,p}}{\partial X}\Big|_{X=1} = 0$$ $$\frac{\partial \Phi''_{2,p}}{\partial X}\Big|_{X=1} = 0$$
$$\frac{1}{l_p}\frac{\partial}{\partial X}\left[\frac{\sigma_{\text{eff,p}}}{l_p}\frac{\partial}{\partial X}\Phi'_{1,p}\right] = a_p F\left(j'_p + j'_{\text{dl,p}}\right)$$ $$\frac{1}{l_p}\frac{\partial}{\partial X}\left[\frac{\sigma_{\text{eff,p}}}{l_p}\frac{\partial}{\partial X}\Phi''_{1,p}\right] = a_p F\left(j''_p + j''_{\text{dl,p}}\right)$$	$$\frac{\partial \Phi'_{1,p}}{\partial X}\Big|_{X=0} = 0$$ $$\frac{\partial \Phi''_{1,p}}{\partial X}\Big|_{X=0} = 0$$ $$\left(\frac{1}{l_p}\frac{\partial \Phi'_{1,p}}{\partial X}\right)\Bigg|_{X=1} = -\frac{I}{\sigma_{eff,p}}$$ $$\left(\frac{1}{l_p}\frac{\partial \Phi''_{1,p}}{\partial X}\right)\Bigg|_{X=1} = 0$$

$-\omega c_p^s{}'' = \frac{1}{r^2}\frac{\partial}{\partial r}\left[r^2 D_p^s \frac{\partial c_p^s{}'}{\partial r} \right]$ $\omega c_p^s{}' = \frac{1}{r^2}\frac{\partial}{\partial r}\left[r^2 D_p^s \frac{\partial c_p^s{}''}{\partial r} \right]$	$\left.\frac{\partial c_p^s{}'}{\partial r}\right\|_{r=0} = 0$ $\left.\frac{\partial c_p^s{}''}{\partial r}\right\|_{r=0} = 0$ $\left. -D_p^s \frac{\partial c_p^s{}'}{\partial r}\right\|_{r=R_p} = j'_p$ $\left. -D_p^s \frac{\partial c_p^s{}''}{\partial r}\right\|_{r=R_p} = j''_p$

Table 5-2: Additional Equations in the P2D impedance model

$\eta'_p = \Phi'_{1,p} - \Phi'_{2,p} - dUdC_p * cps'$ $\eta''_p = \Phi''_{1,p} - \Phi''_{2,p} - dUdC_p * cps''$
$cps' = c_p^s{}'\Big\|_{r=R_p}$ $cps'' = c_p^s{}''\Big\|_{r=R_p}$
$j'_p = \frac{i0_p(\alpha_A + \alpha_C)}{RT}\eta'_p$ $j''_p = \frac{i0_p(\alpha_A + \alpha_C)}{RT}\eta''_p$
$j'_{dl,p} = -\frac{\omega Cdl_p}{F}\left(\Phi''_{1,p} - \Phi''_{2,p}\right)$ $j''_{dl,p} = \frac{\omega Cdl_p}{F}\left(\Phi'_{1,p} - \Phi'_{2,p}\right)$

$$\eta'_n = \Phi'_{1,n} - \Phi'_{2,n} - dUdC_n * cns'$$
$$\eta''_n = \Phi''_{1,n} - \Phi''_{2,n} - dUdC_n * cns''$$

$$cns' = c_n^s \Big|_{r=R_n}$$
$$cns'' = c_n^s \Big|_{r=R_n}$$

$$j'_n = \frac{i0_n\left(\alpha_A + \alpha_C\right)}{RT}\eta'_n$$
$$j''_n = \frac{i0_n\left(\alpha_A + \alpha_C\right)}{RT}\eta''_n$$

$$j'_{dl,n} = -\frac{\omega Cdl_n}{F}\left(\Phi''_{1,n} - \Phi''_{2,n}\right)$$
$$j''_{dl,n} = \frac{\omega Cdl_n}{F}\left(\Phi'_{1,n} - \Phi'_{2,n}\right)$$

$$D_{eff,p} = D\varepsilon_p^{Brugg}$$
$$D_{eff,s} = D\varepsilon_s^{Brugg}$$
$$D_{eff,n} = D\varepsilon_n^{Brugg}$$

$$\kappa_{eff,p} = \kappa\varepsilon_p^{Brugg}$$
$$\kappa_{eff,s} = \kappa\varepsilon_s^{Brugg}$$
$$\kappa_{eff,n} = \kappa\varepsilon_n^{Brugg}$$

$$\sigma_{eff,p} = \sigma_p\left(1 - \varepsilon_p - \varepsilon_{f,p}\right)^{Brugg}$$
$$\sigma_{eff,n} = \sigma_n\left(1 - \varepsilon_n - \varepsilon_{f,n}\right)^{Brugg}$$

5.3. Applying orthogonal collocation

The theory behind orthogonal collocation has been extensively developed, and the stability has been studied.[108-110] In order to solve the equations, a certain number of node points are chosen in each region. The variables to be solved in each region, are assumed to be represented by a polynomial function,

$$u_k(X) = \sum_{i=0}^{N+1} f_i^k X^i = f_0^k + f_1^k X + f_2^k X^2 + ... + f_N^k X^N + f_{N+1}^k X^{N+1} \tag{5.4}$$

where u_k represents the variable to be solved, f_i^k represents the coefficient of X^i, and the superscript '*k*' represents the particular region where the equation is solved (*p, s, n* for the positive electrode, separator, and negative electrode respectively).

The governing equations of the model are then solved at the internal node points, whereas the boundary conditions govern the dynamics at the boundary points. The node points are chosen as the roots of the N^{th} order Jacobi polynomial. We describe the process of collocation for $N=1$ internal node point in each region in appendix. For illustration purposes, arbitrary constants are used for approximating all variables using a polynomial profile. An alternate Lagrangian polynomial form offers the ability to write the polynomial representation for a variable by simply using the dependent variable at the internal collocation points and the boundary points. For example, for $N=1$, a polynomial for a variable *V*, can be written using V_0, V_1 *and* V_2 as

$$V(X) = \frac{V_0(X-0.5)(X-1)}{(0-0.5)(0-1)} + \frac{V_1(X-0)(X-1)}{(0.5-0)(0.5-1)} + \frac{V_2(X-0)(X-0.5)}{(1-0)(1-0.5)}$$

where $V_0, V_1 \; and \; V_2$ are the variables at $X = 0$, $X = 0.5$ (first and only collocation point) and $X = 1$.

It should be noted that after applying orthogonal collocation, the resulting equations are linear equations in the unknown variables and can be solved using any linear solver. This approach can easily be extended to higher number of collocation points until convergence is achieved. As discussed later, higher frequencies necessitate a larger number of collocation points.

5.4. Results

The parameter values used for this work are listed in Table 5-5. The resulting set of equations from the collocation approach is solved in the *Maple* 17 classic worksheet environment and is solved for a range of 70 different frequencies, ranging from 0.5 *mHz* to 10 *kHz* and were also independently solved in C. The results were independently compared with ones obtained by solving the governing equations in COMSOL 4.4, which uses finite element method for the simulation.[107] While solving in COMSOL, a physics-controlled '*extremely fine*' mesh was selected in both the radial and the spatial direction, and the equations were solved using the *MUMPS* solver with a relative tolerance of 1e-4, to ensure convergence. The total computational time required to solve the equations on an Intel(R) Xeon(R) E5-2687W 0 @ 3.1*GHz* CPU with a 32 GB RAM for internal collocation node points was about 4.3 seconds in *Maple* 17, as opposed to over 8 minutes required to solve in COMSOL for the same set of frequencies. The memory required for *Maple* 17 was about 180 MB, as opposed to COMSOL which required in excess of 2 GB. The computational time is even faster (in milliseconds time frame) when moved to a C-based environment.

Figure 5-1 shows the Nyquist plot, plotting the imaginary component versus the real component of the linear impedance, for a range of frequencies, obtained for internal collocation node points. The plot shows the qualitative experimental response observed for Li-ion batteries, with the mass transfer effects (in the solid phase) governing the dynamics at low frequencies, and the interfacial and kinetic effects governing the response at medium frequencies, before a purely ohmic response at very high frequencies.

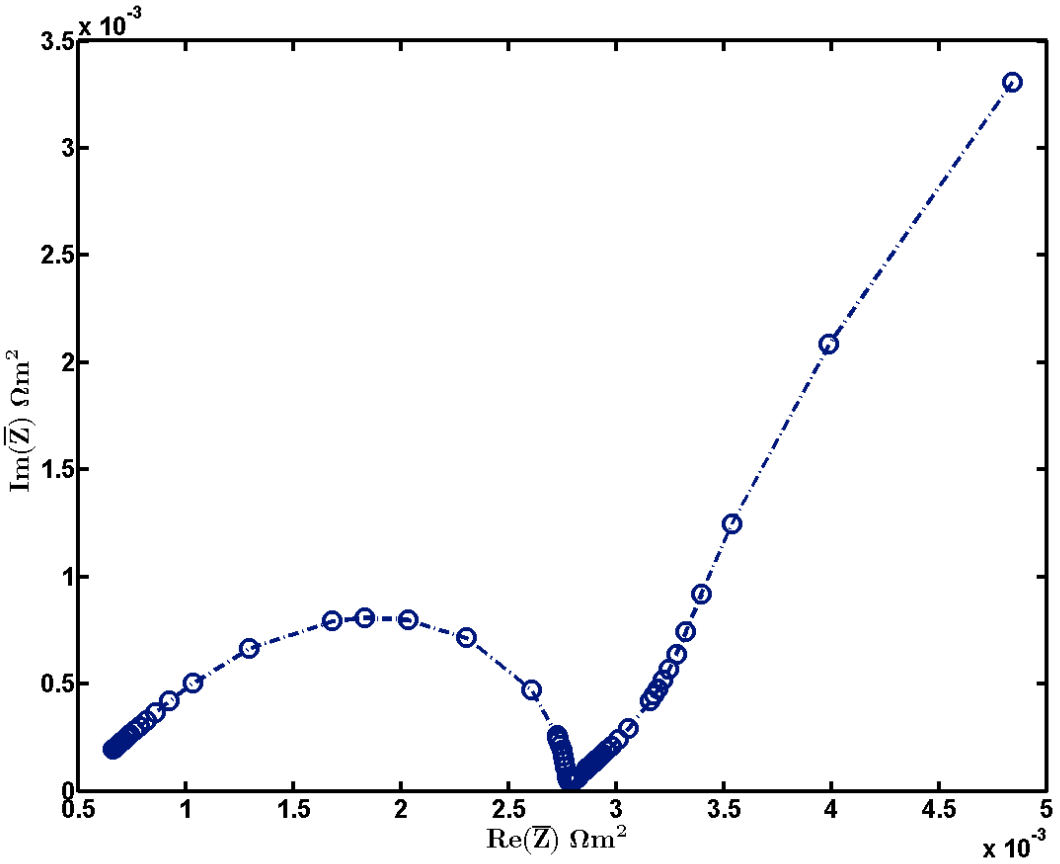

Figure 5-1: Nyquist plot of the imaginary part of impedance vs the real part of impedance

Figure 5-2 (a)-(h) represents the comparison of spatial variation of various variables vs X (thickness of the battery), in each region from the current collector at the negative electrode to the

current collector at the positive electrode , for COMSOL, and the results obtained using for the collocation approach at a frequency of 10 *mHz*. The profiles match exactly.

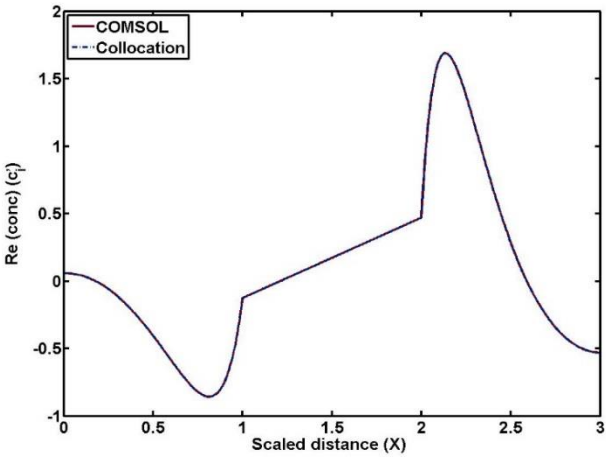

(a)

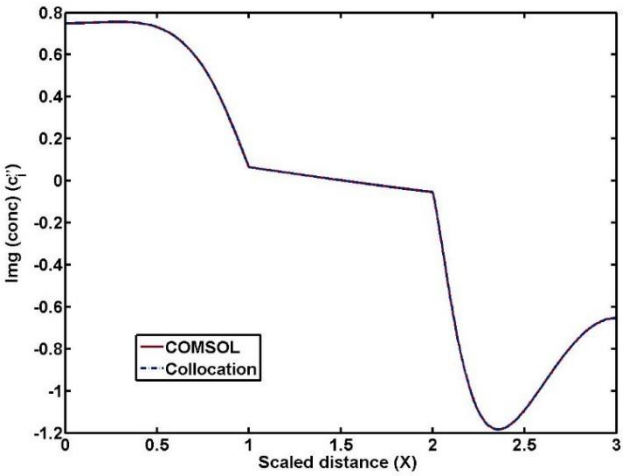

(b)

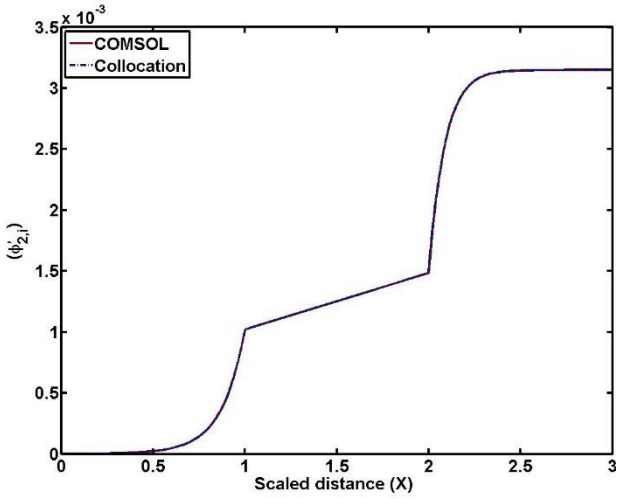

(c)

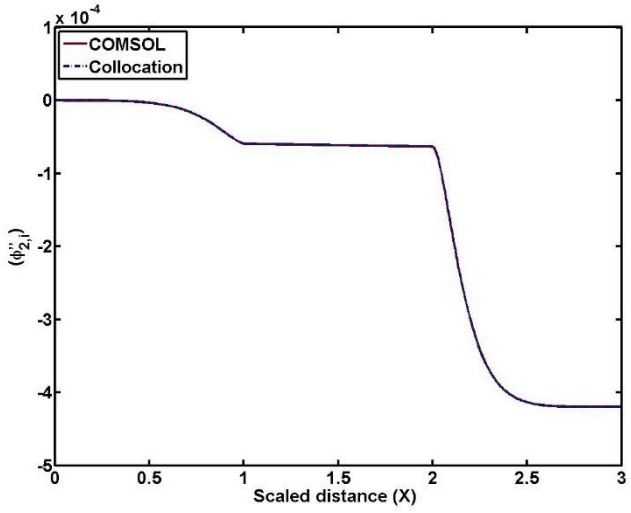

(d)

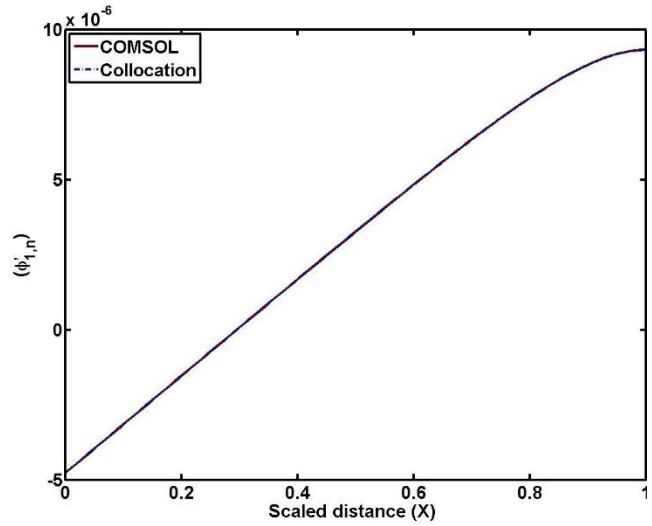

(e)

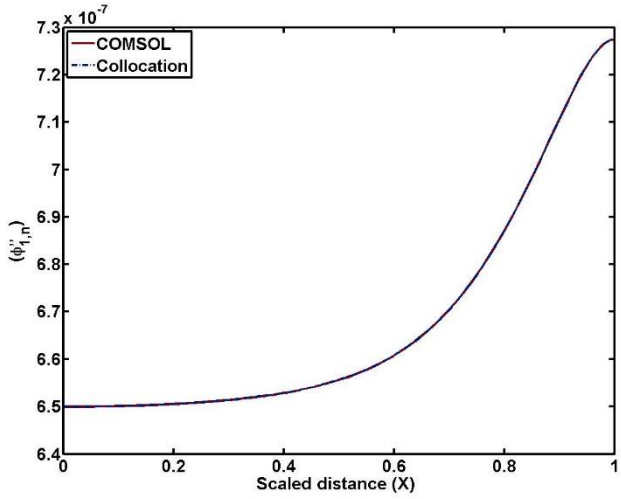

(f)

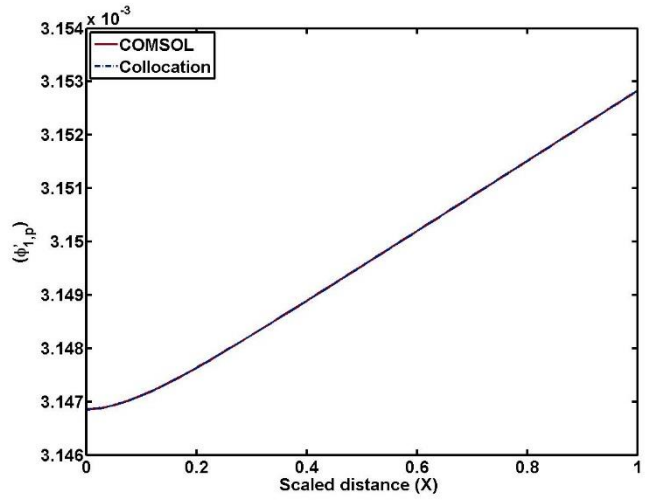

(g)

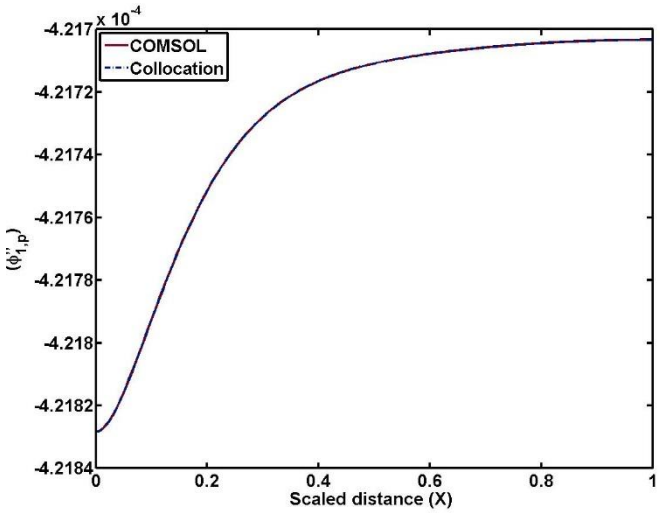

(h)

Figure 5-2: Comparison of variation of internal variables with scaled distance (X) for orthogonal collocation and COMSOL for $\omega = 10$ mHz for (a) Real part of concentration (b) Imaginary part of concentration (c) Real part of liquid phase potential (d) Imaginary part of liquid phase potential (e) Real part of solid phase potential in the negative electrode (f) Imaginary part of solid phase potential in the negative electrode (g) Real part of solid phase potential in the positive electrode (h) Imaginary part of solid phase potential in the positive electrode

At high frequencies, oscillations are observed in the collocation solution. Figure 5-3(a) shows the comparison of the variation of the real part of concentration vs X in the negative electrode at a frequency of 3000 *Hz*, obtained in COMSOL, and collocation using internal node points. Due to high frequency, extremely steep gradients are developed near the anode-separator interface, and the separator-cathode interface, resulting in a significant boundary layer. To capture this phenomenon effectively, a very high number of collocation points are needed to exactly match the continuous profile in the spatial direction. However, the accuracy of the solution is maintained at the collocation node points, without any oscillations. Figure 5-3(b) shows the comparison of the values of the real part of concentration in the negative electrode obtained in COMSOL, and obtained through collocation, plotted only at the discrete collocation points. At points away from the interface, the solution matches well. However, the error is slightly higher close to the boundary at the interface, which needs even larger collocation points.

While using a continuous solution in the spatial coordinate 'x' (*independent variable*) in applying orthogonal collocation, accuracy and stability are guaranteed only at the collocation points, and a linear interpolation between two collocation points will give a more stable solution, compared to the continuous polynomial solution, which might oscillate at high frequencies. Use of alternate collocation approaches such as Chebyshev collocation, reduces the oscillations for the continuous polynomial solution (i.e., continuous polynomial as in equation (5.4)), however the resulting accuracy at the collocation points is lower. The accuracy is highest for Gauss collocation, for rectangular coordinates.[77] Accuracy at the boundary points can be increased by using a higher number of collocation points throughout the region, or by using orthogonal collocation on finite elements (OCFE). OCFE involves dividing the entire spatial domain into smaller finite elements and applying orthogonal collocation in each finite element. The number of collocation points can

be varied in each element, based on the physics of the particular problem. For example, for this problem, higher collocation points can be chosen in elements closer to the interfaces, as compared to the current collectors, since the gradients are steeper closer to the interface. However, the proposed collocation approach already guarantees the desired accuracy in linear impedance (as the accuracy is higher closer to the current collector), and hence other collocation approaches are not explored in this work.

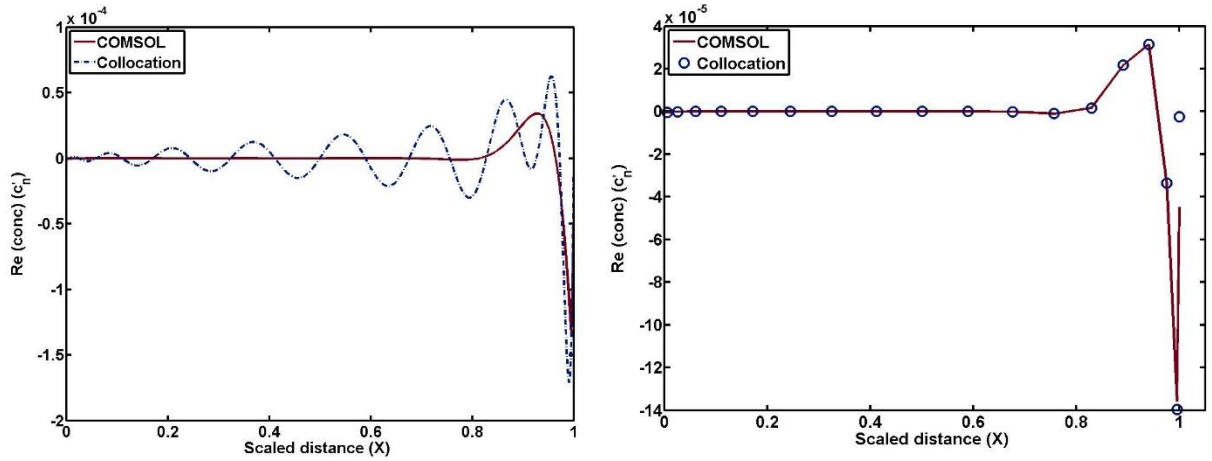

(a) **(b)**

Figure 5-3: Comparison of Real part of concentration vs x in the negative electrode for $\boldsymbol{\omega = 3000}$ Hz (a) plotted for the continuous polynomial solution (b) plotted only at discrete collocation points

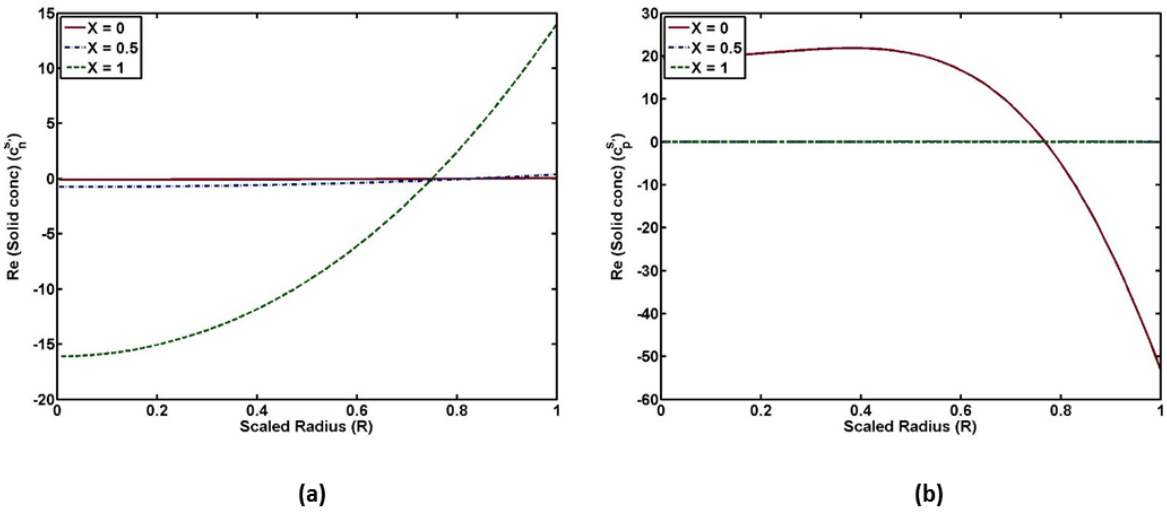

Figure 5-4: Plot of real part of the solid phase concentration in the (a) negative and (b) positive electrode vs scaled radius (R) at ***X = 0, 0.5 and 1*** for ***ω = 10*** mHz

Figure 5-4 (a)(b) shows the real part of the concentration in the solid phase in the negative and positive electrode respectively, vs the radial coordinate *r* at a frequency of 10 *mHz*, at . The concentration gradient is higher closer to the interface than, near the current-collector. Figure 5-5 (a)(b) shows the real part of the concentration in the solid phase in the negative and positive electrode respectively, vs the radial coordinate *r* at a frequency of 1 *Hz*, at . As the frequency increases, very steep gradients are developed closer to the surface of the particle.

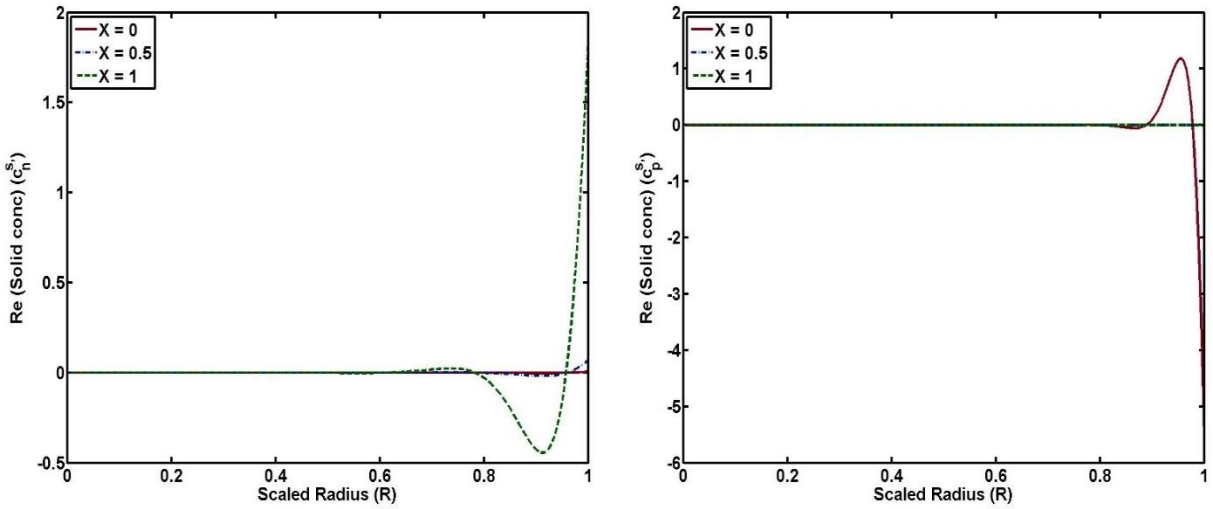

(a) **(b)**

Figure 5-5: Plot of (a) Real part of solid phase concentration in the negative and (b) Real part of solid phase concentration in the positive electrode vs scaled radius (R) at ***X = 0, 0.5 and 1*** for ***ω = 1*** Hz

This approach of orthogonal collocation can easily be extended for higher order terms in the polynomial representation, which are needed for higher frequencies. Figure 5-6 shows the plot for number of node points required for various frequencies, for 6-digit accuracy, when compared to the COMSOL solution. As discussed above, the required number of points increase with increasing frequency as expected.

Table 5-3 shows the values of the real and imaginary part of impedance up to 7 decimal digits obtained after choosing and *17* internal node points along with values obtained in COMSOL at specific frequencies. A frequency of 10 *mHz* requires internal node points, to match with the values obtained in COMSOL for 6-digits accuracy.

Table 5-3: Values of Real and Imaginary part of impedance for various number of collocation points along with COMSOL values

Frequency (*Hz*)	***N = 3***		***N = 7***		***N = 15***		***N = 17***		COMSOL	
	$\mathrm{Re}(\bar{Z})$ (Ωm^2)	$\mathrm{Im}\, g(\bar{Z})$ (Ωm^2)	$\mathrm{Re}(\bar{Z})$ (Ωm^2)	$\mathrm{Im}\, g(\bar{Z})$ (Ωm^2)	$\mathrm{Re}(\bar{Z})$ (Ωm^2)	$\mathrm{Im}\, g(\bar{Z})$ (Ωm^2)	$\mathrm{Re}(\bar{Z})$ (Ωm^2)	$\mathrm{Im}\, g(\bar{Z})$ (Ωm^2)	$\mathrm{Re}(\bar{Z})$ (Ωm^2)	$\mathrm{Im}\, g(\bar{Z})$ (Ωm^2)
0.01	0.0036412	0.0003119	0.0031576	0.00422005	0.0031576	0.0004223	0.0031576	0.0004223	0.0031576	0.0004223
0.1	0.0034421	0.0001167	0.0028985	0.0001365	0.0028978	0.0001369	0.0028978	0.0001369	0.0028978	0.0001369
1	0.0033643	0.0000331	0.0028029	0.0000475	0.0028013	0.0000475	0.0028013	0.0000475	0.0028013	0.0000475
10	0.0033468	0.0000449	0.0027737	0.0000655	0.0027727	0.0000656	0.0027727	0.0000656	0.0027727	0.0000656
100	0.0032124	0.0003164	0.0026064	0.0004714	0.0026058	0.0004728	0.0026058	0.0004728	0.0026058	0.0004728
1000	0.0024953	0.0002098	0.0012766	0.00061305	0.0012916	0.0006642	0.0012916	0.0006642	0.0012916	0.0006642
3000	0.0024487	0.0000739	0.0009827	0.0002832	0.0009198	0.0004208	0.0009195	0.0004205	0.0009195	0.0004206

As mentioned above, the required number of node points increase with increasing frequency with $N = 15$ internal node points required for high frequency of 3000 *Hz*. The table also shows values obtained for internal node points $N = 17$, which match with the values obtained for $N = 15$, up to 6 digits, that proves the self-convergence and consistency of the approach. Typically, COMSOL uses a weak form of the original set of PDEs, but in the collocation approach, the original form (strong form) of the model is simulated. Because of the linearity of the impedance equations in this case, collocation in the spatial dimension '*x*' gives good accuracy. It is possible to apply spectral methods in weak form as well, but the application of that is beyond the scope of this paper.

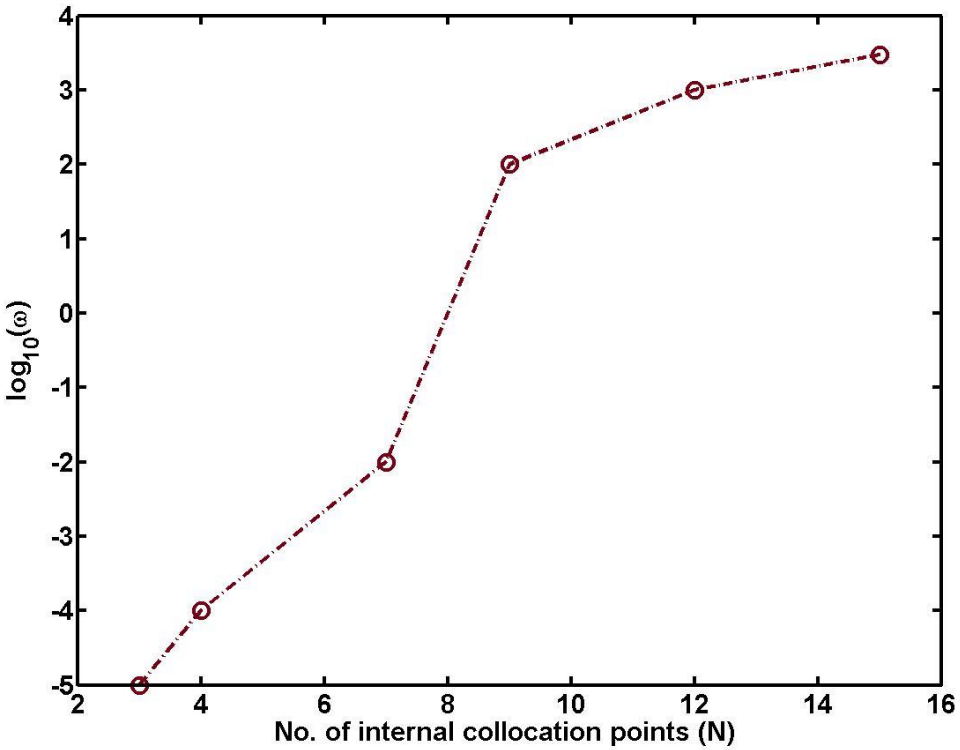

Figure 5-6: Plot of $\boldsymbol{log_{10}(\omega)}$ vs Number of internal collocation points (N) required for 6-digits accuracy

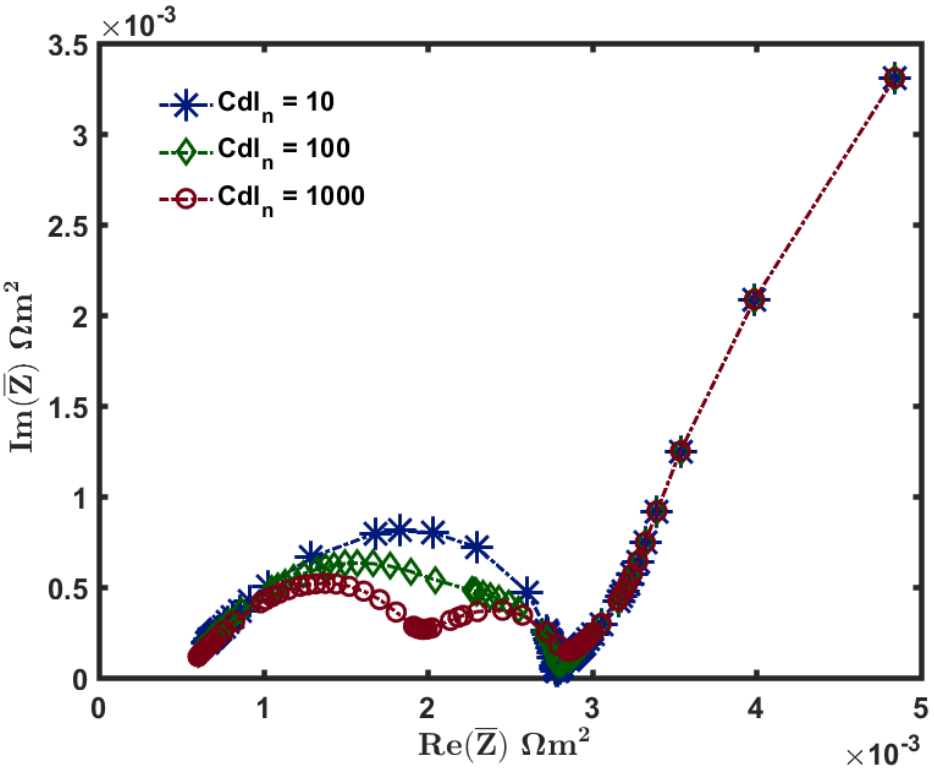

Figure 5-7: Nyquist plot for linear impedance for Cdl_n=10, 100 and 1000 $\mu F/cm^2$

It is important to note that the number of node points needed for the desired accuracy also depends on the set of parameters being used for the system, as the classification of *low/high frequency* is determined entirely by the time constants of various physical processes, which are dictated by the geometric and physicochemical parameters of the battery. For example, the time constant of the electrode for the kinetic processes depend on the charge transfer resistance and the double layer capacitance of the electrode. To illustrate this, Figure 5-7 shows the Nyquist plot comparison for different values of the double layer capacitance for the anode. The distinction in the two arcs of the individual electrodes gets more pronounced as the capacitance of the double layer increases. Table 5-4 shows the comparison between the real and imaginary part of linear impedance values

for different values of the double layer capacitance of anode, for $N=15$ and $N=17$. While the solution matches until 6 decimal digits for $Cdl_n=10$, it only matches until 5 decimal digits for $Cdl_n=100$ and $Cdl_n=1000$. This shows that even higher points than 17 might be required to get convergence for such high values of the anode double layer capacitance, for the same characteristic frequency of 3000 *Hz*. Similar analysis can be done for other sets of parameter values. Since the analysis in this work is only done for one set of parameter values, Figure 5-6 shows the requirement of the number of collocation points in a qualitative sense.

Table 5-4: Values of Real and Imaginary part of impedance for different anode double layer capacitance $(\boldsymbol{Cdl_n})$ for various number of collocation points for a frequency of 3000 Hz

$\boldsymbol{Cdl_n}$ $(\frac{\mu F}{cm^2})$	***N = 15***		***N = 17***	
	$\mathrm{Re}(\bar{Z})$ (Ωm^2)	$\mathrm{Im}\, g(\bar{Z})$ (Ωm^2)	$\mathrm{Re}(\bar{Z})$ (Ωm^2)	$\mathrm{Im}\, g(\bar{Z})$ (Ωm^2)
10	0.0009198	0.0004208	0.0009195	0.0004205
100	0.0007877	0.0003025	0.0007898	0.0003049
1000	0.0007672	0.00002546	0.0007602	0.0002561

In this work, the same number of collocation points were used in each region, namely cathode, separator and anode. However, depending on the problem, different number of collocation points can be used in different regions to get the desired accuracy. As there is no solid-phase in the separator, a lower number of collocation points in that region could still ensure an overall 6-digits accuracy of linear impedance. This kind of variable collocation approach will reduce the resulting number of equations to be solved, which will in turn make the algorithm even faster. In this way, a robust, fail-proof and fast solving code for calculating linear impedance for a full cell has been

obtained that can be used for various goals, including parameter estimation for physics-based models using the EIS data.

5.5. Half Cell Impedance Simulation

In order to improve the performance of lithium-ion batteries, a lot of efforts have been devoted to the development of materials for each component in the battery system. When testing new cathode or anode material, a half-cell configuration with the new material being one electrode and lithium metal being the counter electrode is commonly used by material scientists.[111,112] To broaden the range of application of the proposed impedance simulation approach and to meet the demand of analyzing half-cell impedance data, simulation of the impedance for such a half-cell system is also reported here. Cathode-lithium half-cell is used as an example, but anode-lithium half-cell system can also be simulated using the same approach.

The governing equations for the separator and the cathode in the half cell are the same as in the full cell. The interface between the separator and the anode now becomes the interface between the separator and the lithium metal, which is active in electrochemical reactions. For the Lithium-separator boundary, Butler-Volmer kinetic expression is assumed and determines the potential drop across the interface.[113] The equations and modified boundary conditions are listed in Table 5-6 for clarity. This half-cell model can also be viewed as a base model for fresh lithium metal batteries before cycling.

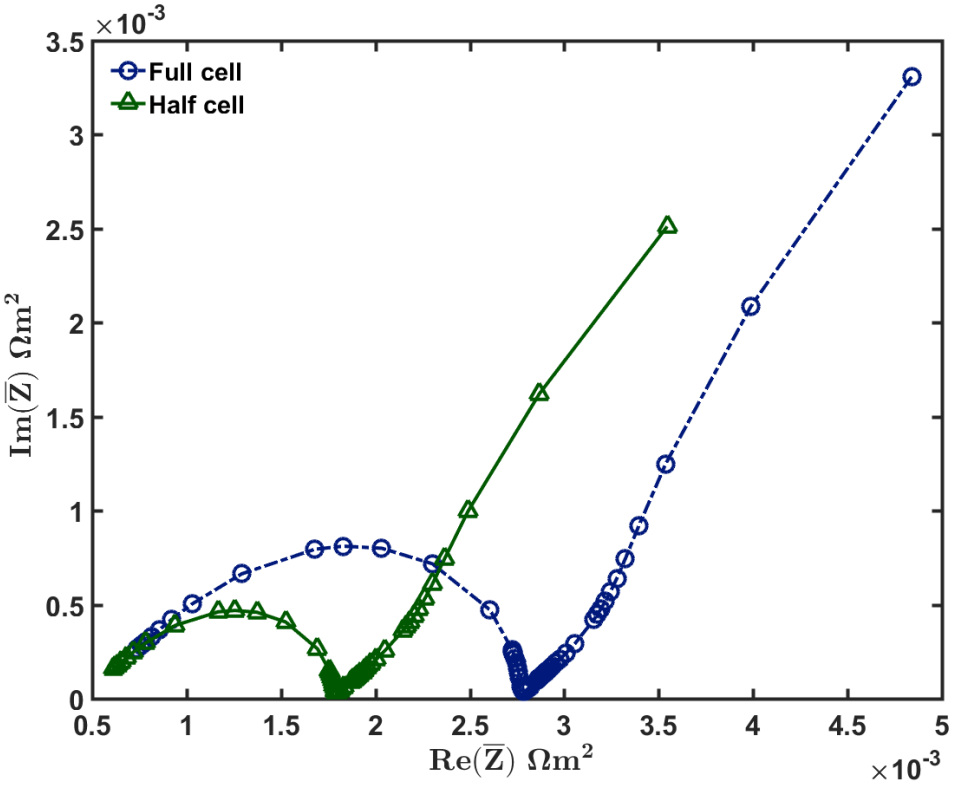

Figure 5-8: Nyquist plot for linear impedance of a full cell and a half cell

A Nyquist plot for a half cell using $N = 17$ collocation node points with the parameters listed in Table 5-5 is shown in Figure 5-8. Compared with the full-cell impedance curve, the half-cell impedance curve has the same shape with an overall reduced value, as expected. The ohmic resistance decreases slightly when removing the graphite electrode while the reduction in charge-transfer resistance is more noticeable.

To test the robustness of this approach, a different set of parameters were used in the half-cell impedance simulation to represent a different chemistry with a different cell design. The new set of parameters are listed in Table 5-7.[114] The impedance of the new half-cell compared to the base-case half-cell is plotted in Figure 5-9. The proposed hybrid analytical-collocation approach is very

stable over the physically reasonable range of the parameter values. The difference in chemistry and cell design can be well captured by this impedance model and is reflected in the Nyquist plot.

Code Dissemination: An executable freeware code for both full- cell and half-cell simulations is hosted at http://depts.washington.edu/maple/EIS.html that can be downloaded to calculate the linear impedance for given frequency with $N = 21$ and $N = 23$ internal node points to check for self-convergence, and gives the real and imaginary part of impedance. The parameters and frequency are read from an external text file. The instructions for running the code are also given on the website. These codes are provided without any restrictions for academic use and not for commercial use. More details about using the codes are provided at the website. Current implementation in C (converted to exe codes) is not the final optimized version, and CPU time and memory requirements are expected to be even better when we continue to optimize the algorithms.

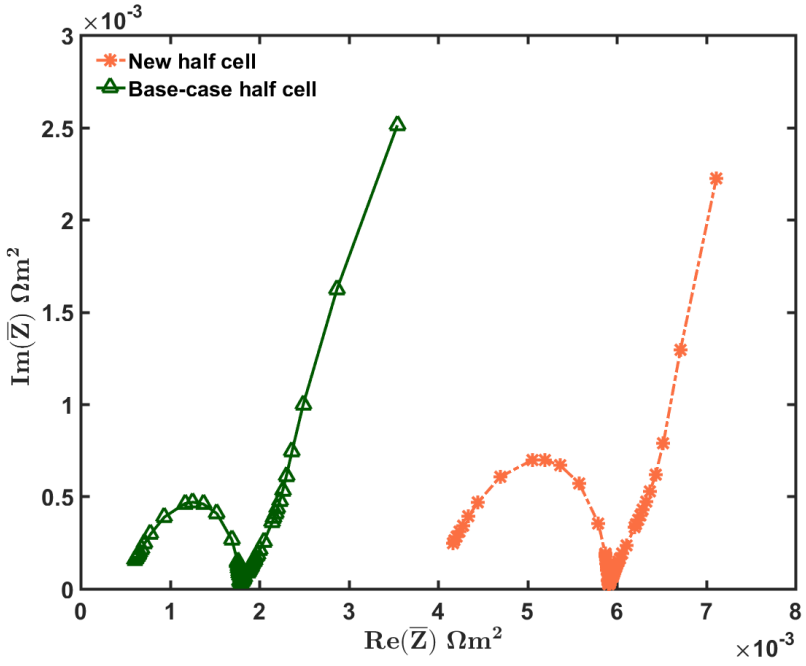

Figure 5-9: Nyquist plot for linear impedance of the base-case half-cell, and new half-cell with different chemistry and design

5.6. Conclusion

A hybrid method of orthogonal collocation across the electrodes coupled with the analytical solution in the solid-phase, for solving the impedance equations for the P2D models that is extremely fast, robust and fail-proof, is presented. Such a model can be used for parameter estimation based on experimental data in real-time, i.e. the impedance equipment can display P2D model predictions before the experiment is completed. Future work involves adding more physics such as the SEI layer dynamics to the existing model, extending the technique to second and higher order harmonics, and estimating the material, transport and kinetic properties using the first and second harmonics signals, which could lead to more insight into battery dynamics that is not captured by EIS.

Table 5-5: List of parameters used for the P2D impedance model

Symbol	Parameter	Positive Electrode	Separator	Negative Electrode	Units
σ_i	Solid phase conductivity	100	-	100	S/m
$\varepsilon_{f,i}$	Filler fraction	0.025	-	0.0326	
ε_i	Porosity	0.385	0.724	0.485	
Brugg	Bruggman Coefficient	4	4	4	

D	Electrolyte diffusivity	7.5×10^{-10}	7.5×10^{-10}	7.5×10^{-10}	m^2/s
κ	Electrolyte conductivity	0.204737	0.204737	0.204737	
D_i^s	Solid Phase Diffusivity	1.0×10^{-14}	-	3.9×10^{-14}	m^2/s
$i0_i$	Reaction Rate constant	3.67	-	3.30	A/m^2
c_0	Initial electrolyte concentration	1000	1000	1000	mol/m^3
$R_{p,i}$	Particle Radius	2.0×10^{-6}	-	2.0×10^{-6}	m
a_i	Particle Surface Area to Volume	885000	-	723600	m^2/m^3
l_i	Region thickness	80×10^{-6}	25×10^{-6}	88×10^{-6}	m
t_+	Transference number	0.364	0.364	0.364	
α_i	Charge transfer coefficient	0.5	-	0.5	

$dUdC_i$	First derivative of open-circuit potential	-11.6724×10^{-6}		-3.21038×10^{-6}	V.m^3/mol
Cdl_i	Double-layer capacitance	10		10	μF/cm^2
F	Faraday's Constant		96487		C/mol
T	Temperature	298	298	298	K
R	Gas Constant		8.314		J/mol/ K
I	Applied Current	1	1	1	A/m^2

Table 5-6: Governing Equations and Boundary conditions for a cathode-lithium half cell

Region	Governing Equations/Boundary Conditions
Lithium-Separator interface	$\frac{-D_{\text{eff,s}}}{l_s}\frac{\partial c'_s}{\partial X}\|_{X=0}=\frac{-I(1-t_+)}{F}$ $\frac{-D_{\text{eff,s}}}{l_s}\frac{\partial c''_s}{\partial X}\|_{X=0}=0$ $\Phi'_{2,n}\|_{X=0}=0$ $\Phi''_{2,n}\|_{X=0}=0$

Separator	$-\varepsilon_s c''_s \omega = \frac{1}{l_s}\frac{\partial}{\partial X}\left[\frac{D_{\text{eff,s}}}{l_s}\frac{\partial c'_s}{\partial X}\right]$ $\varepsilon_s c'_s \omega = \frac{1}{l_s}\frac{\partial}{\partial X}\left[\frac{D_{\text{eff,s}}}{l_s}\frac{\partial c''_s}{\partial X}\right]$ $-\frac{1}{l_s}\frac{\partial}{\partial X}\left[\frac{\kappa_{\text{eff,s}}}{l_s}\left(\frac{\partial \Phi'_{2,s}}{\partial X}\right)\right]+\frac{1}{l_s}\frac{\partial}{\partial X}\left[\frac{2\kappa_{\text{eff,s}}RT}{Fc_0}\frac{(1-t_+)}{l_s}\left(\frac{\partial c'_s}{\partial X}\right)\right]=0$ $-\frac{1}{l_s}\frac{\partial}{\partial X}\left[\frac{\kappa_{\text{eff,s}}}{l_s}\left(\frac{\partial \Phi''_{2,s}}{\partial X}\right)\right]+\frac{1}{l_s}\frac{\partial}{\partial X}\left[\frac{2\kappa_{\text{eff,s}}RT}{Fc_0}\frac{(1-t_+)}{l_s}\left(\frac{\partial c''_s}{\partial X}\right)\right]=0$
Separator-Cathode interface	$\frac{-D_{\text{eff,s}}}{l_s}\frac{\partial c'_s}{\partial X}\Big\|_{X=1}=\frac{-D_{\text{eff,p}}}{l_p}\frac{\partial c'_p}{\partial X}\Big\|_{X=0}$ $\frac{-D_{\text{eff,s}}}{l_s}\frac{\partial c''_s}{\partial X}\Big\|_{X=1}=\frac{-D_{\text{eff,p}}}{l_p}\frac{\partial c''_p}{\partial X}\Big\|_{X=0}$ $\frac{-\kappa_{\text{eff,s}}}{l_s}\frac{\partial \Phi'_{2,s}}{\partial X}\Big\|_{X=1}=\frac{-\kappa_{\text{eff,p}}}{l_p}\frac{\partial \Phi'_{2,p}}{\partial X}\Big\|_{X=0}$ $\frac{-\kappa_{\text{eff,s}}}{l_s}\frac{\partial \Phi''_{2,s}}{\partial X}\Big\|_{X=1}=\frac{-\kappa_{\text{eff,p}}}{l_p}\frac{\partial \Phi''_{2,p}}{\partial X}\Big\|_{X=0}$ $\frac{\partial \Phi'_{1,p}}{\partial X}\Big\|_{X=0}=0$ $\frac{\partial \Phi''_{1,p}}{\partial X}\Big\|_{X=0}=0$ $c'_s\|_{X=1}=c'_p\|_{X=0}$ $c''_s\|_{X=1}=c''_p\|_{X=0}$ $\Phi'_{2,s}\|_{X=1}=\Phi'_{2,p}\|_{X=0}$ $\Phi''_{2,s}\|_{X=1}=\Phi''_{2,p}\|_{X=0}$

Cathode	$$-\varepsilon_p c''_p\,\omega = \frac{1}{l_p}\frac{\partial}{\partial X}\left[\frac{D_{\mathrm{eff,p}}}{l_p}\frac{\partial c'_p}{\partial X}\right] + a_p\left(1-t_+\right)\left(j'_p + j'_{\mathrm{dl,p}}\right)$$ $$\varepsilon_p c'_p\,\omega = \frac{1}{l_p}\frac{\partial}{\partial X}\left[\frac{D_{\mathrm{eff,p}}}{l_p}\frac{\partial c''_p}{\partial X}\right] + a_p\left(1-t_+\right)\left(j''_p + j''_{\mathrm{dl,p}}\right)$$ $$\frac{1}{l_p}\frac{\partial}{\partial X}\left[\frac{-\sigma_{\mathrm{eff,p}}}{l_p}\left(\frac{\partial \Phi'_{1,p}}{\partial X}\right)\right] - \frac{1}{l_p}\frac{\partial}{\partial X}\left[\frac{\kappa_{\mathrm{eff,p}}}{l_p}\left(\frac{\partial \Phi'_{2,p}}{\partial X}\right)\right] + \frac{1}{l_p}\frac{\partial}{\partial X}\left[\frac{2\kappa_{\mathrm{eff,p}}RT}{Fc_0}\frac{\left(1-t_+\right)}{l_p}\left(\frac{\partial c'_p}{\partial X}\right)\right] = 0$$ $$\frac{1}{l_p}\frac{\partial}{\partial X}\left[\frac{-\sigma_{\mathrm{eff,p}}}{l_p}\left(\frac{\partial \Phi''_{1,p}}{\partial X}\right)\right] - \frac{1}{l_p}\frac{\partial}{\partial X}\left[\frac{\kappa_{\mathrm{eff,p}}}{l_p}\left(\frac{\partial \Phi''_{2,p}}{\partial X}\right)\right] + \frac{1}{l_p}\frac{\partial}{\partial X}\left[\frac{2\kappa_{\mathrm{eff,p}}RT}{Fc_0}\frac{\left(1-t_+\right)}{l_p}\left(\frac{\partial c''_p}{\partial X}\right)\right] = 0$$ $$\frac{1}{l_p}\frac{\partial}{\partial X}\left[\frac{\sigma_{\mathrm{eff,p}}}{l_p}\frac{\partial}{\partial X}\Phi'_{1,p}\right] = a_p F\left(j'_p + j'_{\mathrm{dl,p}}\right)$$ $$\frac{1}{l_p}\frac{\partial}{\partial X}\left[\frac{\sigma_{\mathrm{eff,p}}}{l_p}\frac{\partial}{\partial X}\Phi''_{1,p}\right] = a_p F\left(j''_p + j''_{\mathrm{dl,p}}\right)$$ $$-\omega c_p^{s}{}'' = \frac{1}{r^2}\frac{\partial}{\partial r}\left[r^2 D_p^s \frac{\partial c_p^{s}{}'}{\partial r}\right]$$ $$\omega c_p^{s}{}' = \frac{1}{r^2}\frac{\partial}{\partial r}\left[r^2 D_p^s \frac{\partial c_p^{s}{}''}{\partial r}\right]$$

Cathode-current collector interface	$\frac{\partial c'_p}{\partial X}\Big\|_{X=1}=0$ $\frac{\partial c''_p}{\partial X}\Big\|_{X=1}=0$ $\frac{\partial \Phi'_{2,p}}{\partial X}\Big\|_{X=1}=0$ $\frac{\partial \Phi''_{2,p}}{\partial X}\Big\|_{X=1}=0$ $\left(\frac{1}{l_p}\frac{\partial \Phi'_{1,p}}{\partial X}\right)\Big\|_{X=1}=-\frac{I}{\sigma_{eff,p}}$ $\left(\frac{1}{l_p}\frac{\partial \Phi''_{1,p}}{\partial X}\right)\Big\|_{X=1}=0$

Table 5-7: List of parameters for a different chemistry with different cell design

Symbol	Parameter	Positive Electrode	Separator	Units
σ_i	Solid phase conductivity	3.8	-	S/m
$\varepsilon_{f,i}$	Filler fraction	0.214	-	
ε_i	Porosity	0.416	0.593	
Brugg	Bruggman Coefficient	5.2	2.4	
D	Electrolyte diffusivity	3.35×10^{-10}	3.35×10^{-10}	m^2/s
κ	Electrolyte conductivity	0.98	0.98	

D_i^s	Solid Phase Diffusivity	1.0×10^{-13}	-	m^2/s
$i0_i$	Reaction Rate constant	4.16	-	A/m^2
c_0	Initial electrolyte concentration	1000	1000	mol/m^3
$R_{p,i}$	Particle Radius	8.5×10^{-6}	-	m
a_i	Particle Surface Area to Volume	130588	-	m^2/m^3
l_i	Region thickness	144.4×10^{-6}	76×10^{-6}	m
t_+	Transference number	0.363	0.363	

Table 5-8: List of Variables for the P2D impedance model

X	Scaled x-coordinate
c_i'	Real part of the electrolyte concentration in region 'i', $i=\{p,s,n\}$
c_i''	Imaginary part of the electrolyte concentration in region 'i', $i=\{p,s,n\}$
$\Phi'_{1,i}$	Real part of the solid-phase potential in region 'i', $i=\{p,n\}$

$\Phi''_{1,i}$	Imaginary part of the solid-phase potential in region 'i', $i=\{p,n\}$
$\Phi'_{2,i}$	Real part of the electrolyte-phase potential in region 'i', $i=\{p,s,n\}$
$\Phi''_{2,i}$	Imaginary part of the electrolyte-phase potential in region 'i', $i=\{p,s,n\}$
$c_i^s{}'$	Real part of the solid-phase concentration in region 'i', $i=\{p,n\}$
$c_i^s{}''$	Imaginary part of the solid-phase concentration in region 'i', $i=\{p,n\}$
j'_i	Real part of the pore-wall flux in region 'i', $i=\{p,n\}$
j''_i	Imaginary part of the pore-wall flux in region 'i', $i=\{p,n\}$
$j'_{dl,i}$	Real part of the double-layer flux in region 'i', $i=\{p,n\}$
$j''_{dl,i}$	Imaginary part of the double-layer flux in region 'i', $i=\{p,n\}$
η'_i	Real part of the overpotential in region 'i', $i=\{p,n\}$
η''_i	Imaginary part of the overpotential in region 'i', $i=\{p,n\}$
cps'	Real part of the solid-phase concentration at the surface of the particle in the positive electrode
cps''	Imaginary part of the solid-phase concentration at the surface of the particle in the positive electrode

cns'	Real part of the solid-phase concentration at the surface of the particle in the negative electrode
cns''	Imaginary part of the solid-phase concentration at the surface of the particle in the negative electrode

Table 5-9: List of Subscripts

eff	Effective, as for diffusivity or conductivity
c	Related to electrolyte concentration
c^s	Related to solid Phase concentration
n	Related to the negative electrode—the anode
p	Related to the positive electrode—the cathode
s	Related to the separator
dl	Related to the double-layer

Table 5-10: List of Superscripts

avg	Average, as for solid phase concentration
$surf$	Surface, as for solid phase concentration
s	Related to solid phase

1	Related to the solid phase potential
2	Related to the liquid phase potential
'	Representing the real part
"	Representing the imaginary part

Chapter 6: Where do we go from here?

Dynamically time-varying optimal charging profiles are critical to the full utilization of Li-ion batteries. This dissertation is an attempt to identify, explore and validate the use of P2D models for battery management purposes. This study explores various methods of controlling batteries including the Generic Model Control. After obtaining the optimal profile, this study also validates the influence of model-based charging on a 16Ah NMC pouch cell. As the parameters of the battery change with aging, updating the model parameters or model with use would likely produce an even higher benefit. The relative improvement would be a function of the materials and chemistry of the battery, along with the temperature and the charging/discharging conditions in which the battery is used.

Future work involves the development of an advanced self-learning battery management system, which could calculate and implement model-based charging on a Li-ion battery of unknown intercalation-based chemistry. In this BMS, the parameters will be calculated and updated on the fly, in real time, based on the error in the voltage-time measurement. The optimal charging profiles can be calculated and updated every few cycles to maximize the capacity or cycle life based on the application the battery is being used for. In our opinion, such a BMS has a potential to be a game-changer in the industry, and could help in more efficient operations of Li-ion batteries, and could open vast avenues for the secondary-use battery market.

References

1. http://energy.gov/technologytransitions/articles/battery500-consortium-spark-ev-innovations-pacific-northwest-national, Battery500 Consortium to Spark EV Innovations: Pacific Northwest National Laboratory-led, 5-year $50M Effory SEEKS to Almost Triple Energy Stored in Electric Car Batteries, in, Department of Energy, US Website (2016).
2. T. Nguyen, and R.F. Savinell, *Electrochem. Soc. Interface*, **19** (2010).
3. R. T. Doucette, and M.D. McCulloch, *Applied Energy*, **88**, 2315 (2011).
4. N. Ding, K. Prasad, and T.T. Lie *International Journal of Electric and Hybrid Vehicles*, **9**, 49 (2017).
5. W. Lei, E.G. Collins, and H. Li, *IEEE Transactions on Vehicular Technology*, **60**, 1419 (2011).
6. V. Ramadesigan, P.W.C. Northrop, S. De, S. Santhanagopalan, R.D. Braatz, and V.R. Subramanian, *Journal of the Electrochemical Society*, **159**, R31 (2012).
7. B. Suthar, *Optimal Battery Operations and Design Considering Capacity Fade Mechanisms*, WASHINGTON UNIVERSITY IN ST. LOUIS, St Louis, MO, US, (2015).
8. A. Bizeray, S.R. Duncan and D.A. Howey, Advanced battery management systems using fast electrochemical modelling, in *IET Hybrid and Electric Vehicles Conference 2013 (HEVC 2013), Hybrid and Electric Vehicles Conference 2013 (HEVC 2013)*, London, UK (2013).
9. G. L. Plett, *Battery management systems, Volume I: Battery modeling*, Artech House Publishers (2015).
10. M. B. Pinson, and M.Z. Bazant, *Journal of the Electrochemical Society*, **160** (2013).
11. M. Safari, and C. Delacourt, *Journal of the Electrochemical Society*, **158** (2011).
12. C. Delacourt, and M. Safari, *Journal of the Electrochemical Society*, **159** (2012).
13. H. Ekstrom, and G. Lindbergh, *Journal of the Electrochemical Society*, **162** (2015).
14. S. Santhanagopalan, and R.E. White, *Journal of Power Sources*, **161**, 1346 (2006).
15. S. J. Moura, N.A. Chaturvedi, and M. Krstic in *Proceedings of the American Control Conference*, p. 559 (2012).
16. B. Suthar, V. Ramadesigan, P.W.C. Northrop, B. Gopaluni, S. Santhanagopalan, R.D. Braatz, and V.R. Subramanian, in *American Control Conference (ACC)*, p. 5350, Seattle, WA, USA (2013).

17. D. D. Domenica, G. Fiengo, and A. Stefanopoulou, in *Proceedings of the IEEE Conference on Control Applications*, p. 702 (2008).
18. D. D. Domenica, A. Stefanopoulou, and G. Fiengo, *Journal of Dynamic Systems, Measurement and Control* **132**, p. 061302 (2010).
19. C. R. Cutler, *Dynamic Matrix Control: An Optimal Multivariable Control Algorithm with Consraints*, University of Houston, Houston, Texas, (1983).
20. C. E. Garcia, and M. Morari, *Industrial & Engineering Chemistry Process Design and Development*, **21**, 308 (1982).
21. J. Richalet, A. Rault, J.L. Testud, and J. Papon, *Automatica*, **14**, 413 (1978).
22. R. N. Methekar, V. Ramadesigan, R.D. Braatz, and V.R. Subramanian, *ECS Transactions*, **25**, 139 (2010).
23. S. K. Rahimian, S.C. Rayman and R.E. White, *Journal of the Electrochemical Society*, **157**, A1302 (2010).
24. H. E. Perez, X.Hu, and S.J. Moura, in *American Control Conference (ACC)*, p. 4000, Boston (2016).
25. B. Suthar, P.W.C. Northrop, R.D. Braatz,and V.R. Subramanian *Journal of the Electrochemical Society*, **161**, F3144 (2014).
26. A. Hoke, A. Brissette, K. Smith, A. Pratt, and D. Maksimovic, *IEEE Journal of Emerging and Selected Topics in Power Electronics*, **2**, 691 (2014).
27. P. L. Lee, and G.R. Sullivan, *Computers and Chemical Engineering*, **12**, 573 (1987).
28. R. D. Bartusiak, C. Georgakis, and M.J. Reilly, *Chem Eng Sci*, **44**, 1837 (1989).
29. S. M. Alsadaie, and I.M. Mujtaba, *Journal of Process Control*, **44**, 92 (2016).
30. M. Barolo, G.B. Guarise, S. Rienzi, and A. Trotta, *Computers and Chemical Engineering*, **17**, S349 (1993).
31. S. Banerjee, and A.K. Jana *Journal of Process Control*, **24**, 235 (2014).
32. L. Cong, X. Liu, Y. Zhou, and Y. Sun, *AIChE*, **59**, 4133 (2013).
33. T. T. Leea, F.Y. Wanga, A. Islamb, and R.B. Newella, *Journal of Process Control*, **9**, 505 (1999).
34. A. S. A. El-Hamid, *World Applied Sciences Journal*, **18**, 1689 (2012).
35. J. B. Rawlings, *IEEE Control Systems*, **20**, 38 (2000).
36. B. Wu, and R.E. White, *Computers and Chemical Engineering*, **25**, 301 (2001).

37. W. E. Schiesser, *The Numerical Method of Lines*, Academic Press (1991).

38. M. Doyle, T.F. Fuller, and J. Newman, *Journal of the Electrochemical Society*, **140**, 1526 (1993).

39. L. Cai, and R.E. White, *Journal of Power Sources*, **217**, 248 (2012).

40. A. Bizeray, S. Zhao, S.R. Duncan and D.A. Howey, *Journal of Power Sources*, **296**, 400 (2015).

41. P. W. C. Northrop, V. Ramadesigan, S. De, and V.R. Subramanian, *Journal of the Electrochemical Society*, **158**, A1461 (2011).

42. P. W. C. Northrop, M. Pathak, D. Rife, S. De, S. Santhanagopalan, and V.R. Subramanian *Journal of the Electrochemical Society*, **162**, A940 (2016).

43. M. T. Lawder, V. Ramadesigan, B. Suthar, and V.R. Subramanian *Computers and Chemical Engineering*, **82**, 283 (2015).

44. H. Rahimi-Eichi, and Mo-Yuen C., in *IECON 2012 - 38th Annual Conference on IEEE Industrial Electronics Society*, Montreal, Quebec, Canada (2012).

45. R. C. Kroeze, and P.T. Krein, Electrical Battery Model for Use in Dynamic Electric Vehicle Simulations, in *Power Electronics Specialists Conference, 2008. PESC 2008. IEEE* (2008).

46. D. Zhang, B.N. Popov and R.E. White, *Journal of the Electrochemical Society*, **147**, 831 (2000).

47. S. Santhanagopalan, Q. Guo, P. Ramadass and R.E. White, *Journal of Power Sources*, **156**, 620 (2006).

48. J. Liu, G. Li and H.K. Fathy, *Journal of Dynamic Systems, Measurement and Control*, **138**, 021009 (2016).

49. H. E. Perez, X. Hu and S.J. Moura, *American Control Conference (ACC)*, 4000 (2016).

50. R. Klein, N.A. Chaturvedi, J. Christensen, J. Ahmed, R. Findeisen, and A. Kojic, in *2011 American Control Conference*, p. 382, San Francisco, CA, USA (2011).

51. V. Ramadesigan, K. Chen, N.A. Burns, V. Boovaragavan, R.D. Braatz, and V.R. Subramanian, *Journal of the Electrochemical Society*, **158**, A1048 (2011).

52. K. B. Hatzell, A. Sharma, and H.K. Fathy, in *2012 American Control Conference*, p. 584, Montreal, Canada (2012).

53. J. C. Forman, S.J. Moura, J.L. Stein, and H.K. Fathy, *Journal of Power Sources*, **210**, 263 (2012).

54. S. Santhanagopalan, Q. Guo, and R.E. White, *Journal of the Electrochemical Society*, **154**, A198 (2007).

55. D. D. Speltino C., G. Fiengo, and A. Stefanopoulou, in *The European Control Conference*, Budapest (2009).

56. P. Ramadass, B. Haran, P. M. Gomadam, R. White and B. N. Popov, *Journal of the Electrochemical Society*, **151**, A196 (2004).

57. M. Torchio, L. Magni, R.D. Braatz, and D.M. Raimondo, in *11th IFAC Symposium on Dynamics and Control of Process Systems, including Biosystems*, p. 827, Trondheim, Norway (2016).

58. M. Torchio, N.A. Wolff, D.M. Raimondo, L. Magni, U. Krewer, R.B. Gopaluni, J.A. Paulson, and R.D. Braatz, in *American Control Conference (ACC)*, p. 4536, Chicago, IL, USA (2015).

59. A. Wachter, and L.T. Biegler, *Mathematical Programming*, **106**, 25 (2006).

60. G. Leitmann, *The Calculus of Variations and Optimal Control*, Plenum Press, New York (1981).

61. L. S. Pontryagin, V.G. Boltyanskii, R.V. Gamkrelidze, and E.F. Mishchenko, *The Mathematical Theory of Optimal Processes*, John Wiley & Sons, New York (1962).

62. J. T. Betts, *Journal of Guidance, Control, and Dynamics*, **21**, 193 (1998).

63. E. Balsa-Canto, Banga, J. R., Alonso, A.A., and V. S. Vassiliadis, *Journal of Process Control*, **12**, 243 (2002).

64. L. T. Biegler, and I.E. Grossmann, *Chemical Engineering Reviews*, **3**, 1 (1985).

65. W. W. Hager, *Numerical Mathematics*, **87**, 247 (2000).

66. E. B. Budak, and E. Soloveva, *USSR Computational Mathematics and Mathematical Physics*, **9**, 30 (1969).

67. J. Cullum, *SIAM J. Control*, **7**, 32 (1969).

68. W. W. Hager, *SIAM Journal on Numerical Analysis*, **13**, 449 (1976).

69. L. Dontchev, *SIAM Journal on Numerical Analysis*, **18**, 500 (1981).

70. A. Engelsone, S.L. Campbell and J.T. Betts, in *44th IEEE Conference on Decision and Control and the European Control Conference 2005*, p. 3723, Seville, Spain (2005).

71. W. Kang, in *CDC 2008. 47th IEEE Conference on Decision and Control, 2008.*, p. 521, Cancun (2008).

72. S. Kameswaran, and L.T. Biegler, *Computational Optimization and Applications*, **41**, 81 (2008).
73. D. Garg, M. A. Patterson, W. W. Hager, A. V. Rao, D. A. Benson, and G. T. Huntington, *Automatica*, **46**, 1843 (2010).
74. W. W. Hager, H. Hou, and A. V. Rao, *Convergence rate for a Gauss collocation method applied to unconstrained optimal control* (2015).
75. C. W. Gear, *SIAM Journal of Scientific and Statistical Computing*, **7**, 734 (1986).
76. E. Hairer, and G. Wanner, *Journal of Computational and Applied Mathematics*, **111**, 93 (1999).
77. E. Hairer, and G. Wanner, *Solving ordinary differential equations II: Stiff and differential-algebraic problems*, Springer-Verlag, Berlin (1996).
78. W. H. Enright, *SIAM J. of Numerical Analysis*, **11**, 321 (1974).
79. L. Dontchev, W. Hager, and V. M. Veliov, *SIAM J Numerical Analysis*, **38**, 202 (2000).
80. J. T. Betts, and W.P. Huffman, *Optimal Control Applications and Methods*, **19**, 1 (1998).
81. M. Herty, L. Pareschi, and S. Steffensen, *SIAM Journal of Numerical Analysis*, **51**, 1875 (2013).
82. M. E. Orazem, and B. Tribollet, *Electrochemical Impedance Spectroscopy*, Wiley, New Jersey (2008).
83. G. Barsoukov, and J.R. Macdonald, *Impedance Spectroscopy: Theory, Experiment, and Applications*, Wiley-Interscience, New Jersey (2005).
84. M. G. S. R. Thomas, P.G. Bruce, and J.B. Goodenough, *Journal of the Electrochemical Society*, **132** (1985).
85. P. Yu, B.N. Popov, J.A. Ritter, and R.E. White, *Journal of the Electrochemical Society*, **146** (1999).
86. M. Dubarry, A. Devie, and B.Y. Liaw, *Journal of Energy and Power Sources*, **1**, 242 (2014).
87. M. Dubarry, C. Truchot, and B.Y. Liaw, *Journal of Power Sources*, **219**, 204 (2012).
88. C. Pastor-Fernandez, K. Uddin, G.H. Chouchelamane, W.D. Widanage, and J. Marco, *Journal of Power Sources*, **360**, 301 (2017).
89. U. Tröltzsch, O. Kanoun, and H.R. Tränkler, *Electrochimica Acta*, **51**, 1664 (2006).
90. S. Fletcher, *Journal of the Electrochemical Society*, **141**, 1823 (1994).
91. M. Doyle, J.P. Meyers, and J. Newman, *Journal of the Electrochemical Society*, **147**, 99 (2000).

92. M. D. Murbach, and D.T. Schwartz, *Journal of the Electrochemical Society*, **164**, E3311 (2017).

93. D. W. Dees, K.G. Gallagher, D.P. Abraham, and A.N. Jansen, *Journal of the Electrochemical Society*, **160**, A478 (2013).

94. S. B. Forman J.C., J.L. Stein, and H.K. Fathy, *Journal of the Electrochemical Society*, **158**, A93 (2011).

95. L. Cai, and R.E. White, *Journal of the Electrochemical Society*, **156**, A154 (2009).

96. S. Lee, Y. Kim, and H. Chun, *Electrochimica Acta*, **47**, 1055 (2002).

97. V. R. Subramanian, V.D. Diwakar, and D. Tapriyal, *Journal of the Electrochemical Society*, **152**, A2002 (2005).

98. C. Y. Wang, W.B. Gu, and B.Y. Liaw, *Journal of the Electrochemical Society*, **145**, 3407 (1998).

99. Q. Zhang, and R.E. White, *Journal of Power Sources*, **165**, 880 (2007).

100. S. Liu, *Solid State Ionics*, **177**, 53 (2006).

101. J. P. Meyers, M. Doyle, R.M. Darling, and J. Newman, *Journal of the Electrochemical Society*, **147**, 2930 (2000).

102. S. Devan, V.R. Subramanian, and R.E. White, *Journal of the Electrochemical Society*, **151**, A905 (2004).

103. P. M. Gomadam, J.W. Weidner, T.A. Zawodzinski, and A.P. Saab, *Journal of the Electrochemical Society*, **150**, E371 (2003).

104. V. R. Subramanian, V. Boovaragavan, K. Potukuchi, V.D. Diwakar, and A. Guduru, *Electrochem. Solid-State Lett.*, **10**, A25 (2007).

105. G. Sikha, and R.E. White, *Journal of the Electrochemical Society*, **155**, A893 (2008).

106. G. Sikha, and R.E. White, *Journal of the Electrochemical Society*, **154**, A43 (2007).

107. COMSOL, [www.comsol.com, last accessed May 2017].

108. J. Villadsen, and M.L. Michelsen, *Solution of Differential Equation Models by Polynomial Approximation*, Prentice-Hall, Inc. , Englewood Cliffs, NJ (1978).

109. B. A. Finlayson, *Nonlinear Analysis in Chemical Engineering*, McGraw-Hill, New York (1980).

110. S. K. Gupta, *Numerical Methods for Engineers*, New Age International (P) Ltd., Publishers, Delhi (2010).

111. C. Liu, Z. G. Neale and G. Cao, *Materials Today*, **19**, 109 (2016).
112. N. Nitta and G. Yushin, *Particle & Particle Systems Characterization*, **31**, 317 (2014).
113. M. Doyle and J. Newman, *Electrochimica Acta*, **40**, 2191 (1995).
114. P. Arora, M. Doyle, A. S. Gozdz, R. E. White and J. Newman, *Journal of Power Sources*, **88**, 219 (2000).

Appendix A

Example for $N = 1$ collocation point

Equations in the Negative Electrode

Consider the governing equations from Table 5-1, for the real and imaginary parts of the electrolyte concentration, potential in the solid-phase, and potential in the liquid-phase, in the negative electrode along with the boundary conditions. The expressions for the current densities and the overpotentials are substituted from Table 5-2.

$$
\begin{aligned}
-\varepsilon_{\mathrm{n}} c''_{n}\,\omega &= \frac{1}{l_n}\frac{\partial}{\partial X}\left[\frac{D_{\mathrm{eff,n}}}{l_n}\frac{\partial c'_{n}}{\partial X}\right] + a_{\mathrm{n}}\left(1-t_{+}\right)\left(\frac{i0_n\left(\alpha_A+\alpha_C\right)}{RT}\left(\Phi'_{1,n}-\Phi'_{2,n}-dUdC_n * cns'\right)-\frac{\omega Cdl_n}{F}\left(\Phi''_{1,n}-\Phi''_{2,n}\right)\right)\\
\varepsilon_{\mathrm{n}} c'_{n}\,\omega &= \frac{1}{l_n}\frac{\partial}{\partial X}\left[\frac{D_{\mathrm{eff,n}}}{l_n}\frac{\partial c''_{n}}{\partial X}\right] + a_{\mathrm{n}}\left(1-t_{+}\right)\left(\frac{i0_n\left(\alpha_A+\alpha_C\right)}{RT}\left(\Phi''_{1,n}-\Phi''_{2,n}-dUdC_n * cns''\right)+\frac{\omega Cdl_n}{F}\left(\Phi'_{1,n}-\Phi'_{2,n}\right)\right)
\end{aligned}
\tag{A.1}
$$

$$
\begin{aligned}
&\frac{1}{l_n}\frac{\partial}{\partial X}\left[\frac{-\sigma_{\mathrm{eff,n}}}{l_n}\left(\frac{\partial \Phi'_{1,n}}{\partial X}\right)\right]-\frac{1}{l_n}\frac{\partial}{\partial X}\left[\frac{\kappa_{\mathrm{eff,n}}}{l_n}\left(\frac{\partial \Phi'_{2,n}}{\partial X}\right)\right]+\frac{1}{l_n}\frac{\partial}{\partial X}\left[\frac{2\kappa_{\mathrm{eff,n}}RT}{Fc_0}\frac{\left(1-t_{+}\right)}{l_n}\left(\frac{\partial c'_{n}}{\partial X}\right)\right]=0\\
&\frac{1}{l_n}\frac{\partial}{\partial X}\left[\frac{-\sigma_{\mathrm{eff,n}}}{l_n}\left(\frac{\partial \Phi''_{1,n}}{\partial X}\right)\right]-\frac{1}{l_n}\frac{\partial}{\partial X}\left[\frac{\kappa_{\mathrm{eff,n}}}{l_n}\left(\frac{\partial \Phi''_{2,n}}{\partial X}\right)\right]+\frac{1}{l_n}\frac{\partial}{\partial X}\left[\frac{2\kappa_{\mathrm{eff,n}}RT}{Fc_0}\frac{\left(1-t_{+}\right)}{l_n}\left(\frac{\partial c''_{n}}{\partial X}\right)\right]=0
\end{aligned}
\tag{A.2}
$$

$$
\begin{aligned}
\frac{1}{l_n}\frac{\partial}{\partial X}\left[\frac{\sigma_{\mathrm{eff,n}}}{l_n}\frac{\partial}{\partial X}\Phi'_{1,n}\right] &= a_{\mathrm{n}}F\left(\frac{i0_n\left(\alpha_A+\alpha_C\right)}{RT}\left(\Phi'_{1,n}-\Phi'_{2,n}-dUdC_n * cns'\right)-\frac{\omega Cdl_n}{F}\left(\Phi''_{1,n}-\Phi''_{2,n}\right)\right)\\
\frac{1}{l_n}\frac{\partial}{\partial X}\left[\frac{\sigma_{\mathrm{eff,n}}}{l_n}\frac{\partial}{\partial X}\Phi''_{1,n}\right] &= a_{\mathrm{n}}F\left(\frac{i0_n\left(\alpha_A+\alpha_C\right)}{RT}\left(\Phi''_{1,n}-\Phi''_{2,n}-dUdC_n * cns''\right)+\frac{\omega Cdl_n}{F}\left(\Phi'_{1,n}-\Phi'_{2,n}\right)\right)
\end{aligned}
\tag{A.3}
$$

Boundary conditions at the anode current collector $\left(X=0\right)$ are given by:

$$\frac{\partial c'_n}{\partial X}\Big|_{X=0} = 0$$
$$\frac{\partial c''_n}{\partial X}\Big|_{X=0} = 0$$
$$\Phi'_{2,n}\Big|_{X=0} = 0$$
$$\Phi''_{2,n}\Big|_{X=0} = 0 \qquad \text{(A.4)}$$
$$\left(\frac{1}{l_n}\frac{\partial \Phi'_{1,n}}{\partial X}\right)\Bigg|_{X=0} = -\frac{I}{\sigma_{eff,n}}$$
$$\left(\frac{1}{l_n}\frac{\partial \Phi''_{1,n}}{\partial X}\right)\Bigg|_{X=0} = 0$$

Boundary Conditions at the anode-separator interface $(X=1)$ are:

$$\frac{-D_{\text{eff,n}}}{l_n}\frac{\partial c'_n}{\partial X}\Big|_{X=1} = \frac{-D_{\text{eff,s}}}{l_s}\frac{\partial c'_s}{\partial X}\Big|_{X=0}$$
$$\frac{-D_{\text{eff,n}}}{l_n}\frac{\partial c''_n}{\partial X}\Big|_{X=1} = \frac{-D_{\text{eff,s}}}{l_s}\frac{\partial c''_s}{\partial X}\Big|_{X=0}$$
$$\frac{-\kappa_{\text{eff,n}}}{l_n}\frac{\partial \Phi'_{2,n}}{\partial X}\Big|_{X=1} = \frac{-\kappa_{\text{eff,s}}}{l_s}\frac{\partial \Phi'_{2,s}}{\partial X}\Big|_{X=0} \qquad \text{(A.5)}$$
$$\frac{-\kappa_{\text{eff,n}}}{l_n}\frac{\partial \Phi''_{2,n}}{\partial X}\Big|_{X=1} = \frac{-\kappa_{\text{eff,s}}}{l_s}\frac{\partial \Phi''_{2,s}}{\partial X}\Big|_{X=0}$$
$$\frac{\partial \Phi'_{1,n}}{\partial X}\Big|_{X=1} = 0$$
$$\frac{\partial \Phi''_{1,n}}{\partial X}\Big|_{X=1} = 0$$

The internal collocation point inside the negative electrode is chosen as the root of the first-order Jacobi polynomial in the scaled region $X \in [0,1]$. The root lies at $X = \frac{1}{2}$.

Including the boundary points, the three points are now given as $X = \left\{0, \frac{1}{2}, 1\right\}$.

As mentioned previously, the variables are assumed to follow a polynomial profile. For example, the concentrations are given by:

$$c'_n(X) = A_0^n + A_1^n X + A_2^n X^2 = \sum_{i=0}^{2} A_i^n X^i$$
$$c''_n(X) = B_0^n + B_1^n X + B_2^n X^2 = \sum_{i=0}^{2} B_i^n X^i \quad \text{(A.6)}$$

Similarly, the potentials in each phase are represented by:

$$\Phi'_{1,n}(X) = C_0^n + C_1^n X + C_2^n X^2 = \sum_{i=0}^{2} C_i^n X^i$$
$$\Phi''_{1,n}(X) = E_0^n + E_1^n X + E_2^n X^2 = \sum_{i=0}^{2} E_i^n X^i \quad \text{(A.7)}$$

$$\Phi'_{2,n}(X) = Q_0^n + Q_1^n X + Q_2^n X^2 = \sum_{i=0}^{2} Q_i^n X^i$$
$$\Phi''_{2,n}(X) = R_0^n + R_1^n X + R_2^n X^2 = \sum_{i=0}^{2} R_i^n X^i \quad \text{(A.8)}$$

where $A_i^n, B_i^n, C_i^n, E_i^n, Q_i^n$ and R_i^n are the coefficients of X^i, and the superscript '*n*' denotes the values in the negative electrode region.

Values of the real and imaginary parts of each of the variables are assumed at these three node points as:

$$c'_n(X) = \left\{c'_{n,1}, c'_{n,2}, c'_{n,3}\right\}$$
$$c''_n(X) = \left\{c''_{n,1}, c''_{n,2}, c''_{n,3}\right\}$$
$$\Phi'_{1,n}(X) = \left\{\varphi'_{n,1}, \varphi'_{n,2}, \varphi'_{n,3}\right\}$$
$$\Phi''_{1,n}(X) = \left\{\varphi''_{n,1}, \varphi''_{n,2}, \varphi''_{n,3}\right\} \quad \text{(A.9)}$$
$$\Phi'_{2,n}(X) = \left\{\psi'_{n,1}, \psi'_{n,2}, \psi'_{n,3}\right\}$$
$$\Phi''_{2,n}(X) = \left\{\psi''_{n,1}, \psi''_{n,2}, \psi''_{n,3}\right\}$$

Substituting the values of *X* in equation (A.6), the following relations can be easily derived.

$$c'_{n,1} = A_0^n + A_1^n(0) + A_2^n(0)^2 = A_0^n$$
$$c'_{n,2} = A_0^n + A_1^n * \left(\frac{1}{2}\right) + A_2^n * \left(\frac{1}{2}\right)^2 \quad \text{(A.10)}$$
$$c'_{n,3} = A_0^n + A_1^n * (1) + A_2^n * (1)^2$$

The coefficients A_0^n, A_1^n, A_2^n can easily be solved in terms of $c'_{n,1}, c'_{n,2}, c'_{n,3}$. Similar equations are obtained for other variables.

$$c''_{n,1} = B_0^n + B_1^n(0) + B_2^n(0)^2 = B_0^n$$
$$c''_{n,2} = B_0^n + B_1^n * \left(\frac{1}{2}\right) + B_2^n * \left(\frac{1}{2}\right)^2 \quad \text{(A.11)}$$
$$c''_{n,3} = B_0^n + B_1^n * (1) + B_2^n * (1)^2$$

$$\varphi'_{n,1} = C_0^n$$
$$\varphi'_{n,2} = C_0^n + C_1^n * \left(\frac{1}{2}\right) + C_2^n * \left(\frac{1}{2}\right)^2 \quad \text{(A.12)}$$
$$\varphi'_{n,3} = C_0^n + C_1^n * (1) + C_2^n * (1)^2$$

$$\varphi''_{n,1} = E_0^n$$
$$\varphi''_{n,2} = E_0^n + E_1^n * \left(\frac{1}{2}\right) + E_2^n * \left(\frac{1}{2}\right)^2 \quad \text{(A.13)}$$
$$\varphi''_{n,3} = E_0^n + E_1^n * (1) + E_2^n * (1)^2$$

$$\psi'_{n,1} = Q_0^n$$
$$\psi'_{n,2} = Q_0^n + Q_1^n * \left(\frac{1}{2}\right) + Q_2^n * \left(\frac{1}{2}\right)^2 \quad \text{(A.14)}$$
$$\psi'_{n,3} = Q_0^n + Q_1^n * (1) + Q_2^n * (1)^2$$

$$\psi''_{n,1} = R_0^n$$
$$\psi''_{n,2} = R_0^n + R_1^n * \left(\frac{1}{2}\right) + R_2^n * \left(\frac{1}{2}\right)^2 \qquad \text{(A.15)}$$
$$\psi''_{n,3} = R_0^n + R_1^n * (1) + R_2^n * (1)^2$$

Equations (A.11)-(A.15) can be used to eliminate all the coefficients B_i^n, C_i^n, E_i^n, Q_i^n and R_i^n in terms of the variables at the specific node points, as shown in the right hand side of equation (A.9).

Equations (A.6)-(A.8) are substituted in the governing equations (A.1)-(A.3) to get:

$$-\varepsilon_n \left(\sum_{i=0}^{2} B_i^n X^i\right)\omega = \frac{1}{l_n}\left[\frac{D_{\text{eff,n}}}{l_n}\left(2A_2^n\right)\right] + a_n\left(1-t_+\right)\left(\begin{array}{l}\dfrac{i0_n\left(\alpha_A+\alpha_C\right)}{RT}\left(\left(\sum_{i=0}^{2} C_i^n X^i\right)-\left(\sum_{i=0}^{2} Q_i^n X^i\right)-dUdC_n * cns'\right)\\ -\ \dfrac{\omega C dl_n}{F}\left(\left(\sum_{i=0}^{2} E_i^n X^i\right)-\left(\sum_{i=0}^{2} R_i^n X^i\right)\right)\end{array}\right)$$

$$\varepsilon_n \left(\sum_{i=0}^{2} A_i^n X^i\right)\omega = \frac{1}{l_n}\left[\frac{D_{\text{eff,n}}}{l_n}\left(2B_2^n\right)\right] + a_n\left(1-t_+\right)\left(\begin{array}{l}\dfrac{i0_n\left(\alpha_A+\alpha_C\right)}{RT}\left(\left(\sum_{i=0}^{2} E_i^n X^i\right)-\left(\sum_{i=0}^{2} R_i^n X^i\right)-dUdC_n * cns''\right)\\ +\ \dfrac{\omega C dl_n}{F}\left(\left(\sum_{i=0}^{2} C_i^n X^i\right)-\left(\sum_{i=0}^{2} Q_i^n X^i\right)\right)\end{array}\right) \qquad \text{(A.16)}$$

$$\frac{1}{l_n}\left[\frac{-\sigma_{\text{eff,n}}}{l_n}\left(2C_2^n\right)\right] - \frac{1}{l_n}\left[\frac{\kappa_{\text{eff,n}}}{l_n}\left(2Q_2^n\right)\right] + \frac{1}{l_n}\left[\frac{2\kappa_{\text{eff,n}}RT}{Fc_0}\frac{\left(1-t_+\right)}{l_n}\left(2A_2^n\right)\right] = 0$$
$$\frac{1}{l_n}\left[\frac{-\sigma_{\text{eff,n}}}{l_n}\left(2E_2^n\right)\right] - \frac{1}{l_n}\left[\frac{\kappa_{\text{eff,n}}}{l_n}\left(2R_2^n\right)\right] + \frac{1}{l_n}\left[\frac{2\kappa_{\text{eff,n}}RT}{Fc_0}\frac{\left(1-t_+\right)}{l_n}\left(2B_2^n\right)\right] = 0 \qquad \text{(A.17)}$$

$$\frac{1}{l_n}\left[\frac{\sigma_{\text{eff,n}}}{l_n}\left(2C_2^n\right)\right] = a_n F\left(\begin{array}{l}\dfrac{i0_n\left(\alpha_A+\alpha_C\right)}{RT}\left(\left(\sum_{i=0}^{2}C_i^n X^i\right)-\left(\sum_{i=0}^{2}Q_i^n X^i\right)-dUdC_n * cns'\right)\\ -\dfrac{\omega Cdl_n}{F}\left(\left(\sum_{i=0}^{2}E_i^n X^i\right)-\left(\sum_{i=0}^{2}R_i^n X^i\right)\right)\end{array}\right)$$

$$\frac{1}{l_n}\left[\frac{\sigma_{\text{eff,n}}}{l_n}\left(2E_2^n\right)\right] = a_n F\left(\begin{array}{l}\dfrac{i0_n\left(\alpha_A+\alpha_C\right)}{RT}\left(\left(\sum_{i=0}^{2}E_i^n X^i\right)-\left(\sum_{i=0}^{2}R_i^n X^i\right)-dUdC_n * cns''\right)\\ +\dfrac{\omega Cdl_n}{F}\left(\left(\sum_{i=0}^{2}C_i^n X^i\right)-\left(\sum_{i=0}^{2}Q_i^n X^i\right)\right)\end{array}\right) \quad \text{(A.18)}$$

Where cns' and cns'' are the real and imaginary parts of the surface concentrations of the particle in the solid-phase respectively, and are given by the analytical solution of the coupled solid-phase equations, in the radial direction.

Equations (A.16)-(A.18) are valid at the internal collocation points, and hence the values of X $\left(X=\frac{1}{2}\right)$ is substituted in (A.16)-(A.18). Further, equations (A.10)-(A.15) can be used to get:

$$-\varepsilon_n\left(c''_{n,2}\right)\omega = \frac{1}{l_n}\left[\frac{D_{\text{eff,n}}}{l_n}\left(2A_2^n\right)\right] + a_n\left(1-t_+\right)\left(\begin{array}{l}\dfrac{i0_n\left(\alpha_A+\alpha_C\right)}{RT}\left(\left(\varphi'_{n,2}\right)-\left(\psi'_{n,2}\right)-dUdC_n * cns'\right)\\ -\dfrac{\omega Cdl_n}{F}\left(\left(\varphi''_{n,2}\right)-\left(\psi''_{n,2}\right)\right)\end{array}\right)$$

$$\varepsilon_n\left(c'_{n,2}\right)\omega = \frac{1}{l_n}\left[\frac{D_{\text{eff,n}}}{l_n}\left(2B_2^n\right)\right] + a_n\left(1-t_+\right)\left(\begin{array}{l}\dfrac{i0_n\left(\alpha_A+\alpha_C\right)}{RT}\left(\left(\varphi''_{n,2}\right)-\left(\psi''_{n,2}\right)-dUdC_n * cns''\right)\\ +\dfrac{\omega Cdl_n}{F}\left(\left(\varphi'_{n,2}\right)-\left(\psi'_{n,2}\right)\right)\end{array}\right) \quad \text{(A.19)}$$

$$\frac{1}{l_n}\left[\frac{-\sigma_{\text{eff,n}}}{l_n}\left(2C_2^n\right)\right]-\frac{1}{l_n}\left[\frac{\kappa_{\text{eff,n}}}{l_n}\left(2Q_2^n\right)\right]+\frac{1}{l_n}\left[\frac{2\kappa_{\text{eff,n}}RT}{Fc_0}\frac{\left(1-t_+\right)}{l_n}\left(2A_2^n\right)\right]=0$$

$$\frac{1}{l_n}\left[\frac{-\sigma_{\text{eff,n}}}{l_n}\left(2E_2^n\right)\right]-\frac{1}{l_n}\left[\frac{\kappa_{\text{eff,n}}}{l_n}\left(2R_2^n\right)\right]+\frac{1}{l_n}\left[\frac{2\kappa_{\text{eff,n}}RT}{Fc_0}\frac{\left(1-t_+\right)}{l_n}\left(2B_2^n\right)\right]=0 \quad \text{(A.20)}$$

$$\frac{1}{l_n}\left[\frac{\sigma_{\text{eff,n}}}{l_n}\left(2C_2^n\right)\right] = a_{\text{n}}F\left(\frac{i0_n\left(\alpha_A+\alpha_C\right)}{RT}\left(\left(\varphi'_{n,2}\right)-\left(\psi'_{n,2}\right)-dUdC_n*cns'\right)-\frac{\omega Cdl_n}{F}\left(\left(\varphi''_{n,2}\right)-\left(\psi''_{n,2}\right)\right)\right)$$

$$\frac{1}{l_n}\left[\frac{\sigma_{\text{eff,n}}}{l_n}\left(2E_2^n\right)\right] = a_{\text{n}}F\left(\frac{i0_n\left(\alpha_A+\alpha_C\right)}{RT}\left(\left(\varphi''_{n,2}\right)-\left(\psi''_{n,2}\right)-dUdC_n*cns''\right)+\frac{\omega Cdl_n}{F}\left(\left(\varphi'_{n,2}\right)-\left(\psi'_{n,2}\right)\right)\right)$$

(A.21)

It should be noted that equation (A.20) remains the same as equation (A.17) in this case, as there is no X term in equation (A.17). However, when collocation for higher internal node points is considered, equation (A.20) will have more terms owing to more number of roots of the resulting higher order polynomial.

At the boundary points $\left(X=0 \text{ and } X=1\right)$, the boundary conditions (A.4)-(A.5) give additional sets of equations for each variable. Equations (A.6)-(A.8) can be used in the boundary conditions to get:

$$\begin{aligned}
&A_1^n = 0\\
&B_1^n = 0\\
&Q_1^n = 0\\
&R_1^n = 0\\
&\frac{1}{l_n}C_1^n = -\frac{I}{\sigma_{eff,n}}\\
&E_1^n = 0
\end{aligned}$$

(A.22)

$$\frac{-D_{\text{eff,n}}}{l_n}\left(A_1^n + 2A_2^n(1)\right) = \frac{-D_{\text{eff,s}}}{l_s}\left(A_1^s\right)$$
$$\frac{-D_{\text{eff,n}}}{l_n}\left(B_1^n + 2B_2^n(1)\right) = \frac{-D_{\text{eff,s}}}{l_s}\left(B_1^s\right)$$
$$\frac{-\kappa_{\text{eff,n}}}{l_n}\left(Q_1^n + 2Q_2^n(1)\right) = \frac{-\kappa_{\text{eff,s}}}{l_s}\left(Q_1^s\right) \qquad \text{(A.23)}$$
$$\frac{-\kappa_{\text{eff,n}}}{l_n}\left(R_1^n + 2R_2^n(1)\right) = \frac{-\kappa_{\text{eff,s}}}{l_s}\left(R_1^s\right)$$
$$C_1^n + 2C_2^n(1) = 0$$
$$E_1^n + 2E_2^n(1) = 0$$

Equations in the separator

A similar treatment as done in the negative electrode can be done to obtain the resulting equations in the separator region. For the sake of brevity, below we only show the resulting equations in the separator region.

$$c'_{s,1} = A_0^s$$
$$c'_{s,2} = A_0^s + A_1^s * \left(\frac{1}{2}\right) + A_2^s * \left(\frac{1}{2}\right)^2 \qquad \text{(A.24)}$$
$$c'_{s,3} = A_0^s + A_1^s * (1) + A_2^s * (1)^2$$

$$c''_{s,1} = B_0^s$$
$$c''_{s,2} = B_0^s + B_1^s * \left(\frac{1}{2}\right) + B_2^s * \left(\frac{1}{2}\right)^2 \qquad \text{(A.25)}$$
$$c''_{s,3} = B_0^s + B_1^s * (1) + B_2^s * (1)^2$$

$$\varphi'_{s,1} = C_0^s$$
$$\varphi'_{s,2} = C_0^s + C_1^s * \left(\frac{1}{2}\right) + C_2^s * \left(\frac{1}{2}\right)^2 \qquad \text{(A.26)}$$
$$\varphi'_{s,3} = C_0^s + C_1^s * (1) + C_2^s * (1)^2$$

$$\varphi''_{s,1} = E_0^s$$
$$\varphi''_{s,2} = E_0^s + E_1^s * \left(\frac{1}{2}\right) + E_2^s * \left(\frac{1}{2}\right)^2 \qquad \text{(A.27)}$$
$$\varphi''_{s,3} = E_0^s + E_1^s * (1) + E_2^s * (1)^2$$

$$\psi'_{s,1} = Q_0^s$$
$$\psi'_{s,2} = Q_0^s + Q_1^s * \left(\frac{1}{2}\right) + Q_2^s * \left(\frac{1}{2}\right)^2 \qquad \text{(A.28)}$$
$$\psi'_{s,3} = Q_0^s + Q_1^s * (1) + Q_2^s * (1)^2$$

$$\psi''_{s,1} = R_0^s$$
$$\psi''_{s,2} = R_0^s + R_1^s * \left(\frac{1}{2}\right) + R_2^s * \left(\frac{1}{2}\right)^2 \qquad \text{(A.29)}$$
$$\psi''_{s,3} = R_0^s + R_1^s * (1) + R_2^s * (1)^2$$

$$-\varepsilon_s \left(c''_{s,2}\right)\omega = \frac{1}{l_s}\left[\frac{D_{\text{eff,s}}}{l_s}\left(2A_2^s\right)\right]$$
$$\varepsilon_s \left(c'_{s,2}\right)\omega = \frac{1}{l_s}\left[\frac{D_{\text{eff,s}}}{l_s}\left(2B_2^s\right)\right] \qquad \text{(A.30)}$$

$$
\begin{aligned}
&-\frac{1}{l_s}\left[\frac{\kappa_{\text{eff,s}}}{l_s}\left(2Q_2^s\right)\right]+\frac{1}{l_s}\left[\frac{2\kappa_{\text{eff,s}}RT}{Fc_0}\frac{\left(1-t_+\right)}{l_s}\left(2A_2^s\right)\right]=0\\
&-\frac{1}{l_s}\left[\frac{\kappa_{\text{eff,s}}}{l_s}\left(2R_2^s\right)\right]+\frac{1}{l_s}\left[\frac{2\kappa_{\text{eff,s}}RT}{Fc_0}\frac{\left(1-t_+\right)}{l_s}\left(2B_2^s\right)\right]=0
\end{aligned}
\qquad \text{(A.31)}
$$

The boundary conditions at the anode-separator interface lead to:

$$
\begin{aligned}
&c'_{n,3}=c'_{s,1}\\
&c''_{n,3}=c''_{s,1}\\
&\psi'_{n,3}=\psi'_{s,1}\\
&\psi''_{n,3}=\psi''_{s,1}
\end{aligned}
\qquad \text{(A.32)}
$$

And the boundary conditions at the separator-cathode interface lead to:

$$
\begin{aligned}
&c'_{s,3}=c'_{p,1}\\
&c''_{s,3}=c''_{p,1}\\
&\psi'_{s,3}=\psi'_{p,1}\\
&\psi''_{s,3}=\psi''_{p,1}
\end{aligned}
\qquad \text{(A.33)}
$$

Equations in the positive electrode

Again, a similar treatment in the positive electrode leads to the following set of equations.

$$
\begin{aligned}
&c'_{p,1}=A_0^p\\
&c'_{p,2}=A_0^p+A_1^p*\left(\frac{1}{2}\right)+A_2^p*\left(\frac{1}{2}\right)^2\\
&c'_{p,3}=A_0^p+A_1^p*(1)+A_2^p*(1)^2
\end{aligned}
\qquad \text{(A.34)}
$$

$$
\begin{aligned}
&c''_{p,1}=B_0^p\\
&c''_{p,2}=B_0^p+B_1^p*\left(\frac{1}{2}\right)+B_2^p*\left(\frac{1}{2}\right)^2\\
&c''_{p,3}=B_0^p+B_1^p*(1)+B_2^p*(1)^2
\end{aligned}
\qquad \text{(A.35)}
$$

$$\varphi'_{p,1} = C_0^p$$
$$\varphi'_{p,2} = C_0^p + C_1^p * \left(\frac{1}{2}\right) + C_2^p * \left(\frac{1}{2}\right)^2 \quad \text{(A.36)}$$
$$\varphi'_{p,3} = C_0^p + C_1^p * (1) + C_2^p * (1)^2$$

$$\varphi''_{p,1} = E_0^p$$
$$\varphi''_{p,2} = E_0^p + E_1^p * \left(\frac{1}{2}\right) + E_2^p * \left(\frac{1}{2}\right)^2 \quad \text{(A.37)}$$
$$\varphi''_{p,3} = E_0^p + E_1^p * (1) + E_2^p * (1)^2$$

$$\psi'_{p,1} = Q_0^p$$
$$\psi'_{p,2} = Q_0^p + Q_1^p * \left(\frac{1}{2}\right) + Q_2^p * \left(\frac{1}{2}\right)^2 \quad \text{(A.38)}$$
$$\psi'_{p,3} = Q_0^p + Q_1^p * (1) + Q_2^p * (1)^2$$

$$\psi''_{p,1} = R_0^p$$
$$\psi''_{p,2} = R_0^p + R_1^p * \left(\frac{1}{2}\right) + R_2^p * \left(\frac{1}{2}\right)^2 \quad \text{(A.39)}$$
$$\psi''_{p,3} = R_0^p + R_1^p * (1) + R_2^p * (1)^2$$

The governing equations in the positive electrode at the collocation point are given by:

$$-\varepsilon_p \left(c''_{p,2}\right)\omega = \frac{1}{l_p}\left[\frac{D_{\text{eff,p}}}{l_p}\left(2A_2^p\right)\right] + a_p(1-t_+)\left(\frac{i0_p(\alpha_A+\alpha_C)}{RT}\left(\left(\varphi'_{p,2}\right)-\left(\psi'_{p,2}\right)-dUdC_p * cps'\right)-\frac{\omega Cdl_p}{F}\left(\left(\varphi''_{p,2}\right)-\left(\psi''_{p,2}\right)\right)\right)$$
$$\varepsilon_p \left(c'_{p,2}\right)\omega = \frac{1}{l_p}\left[\frac{D_{\text{eff,p}}}{l_p}\left(2B_2^p\right)\right] + a_p(1-t_+)\left(\frac{i0_p(\alpha_A+\alpha_C)}{RT}\left(\left(\varphi''_{p,2}\right)-\left(\psi''_{p,2}\right)-dUdC_p * cps''\right)+\frac{\omega Cdl_p}{F}\left(\left(\varphi'_{p,2}\right)-\left(\psi'_{p,2}\right)\right)\right)$$

(A.40)

$$\frac{1}{l_p}\left[\frac{-\sigma_{\text{eff,p}}}{l_p}\left(2C_2^p\right)\right]-\frac{1}{l_p}\left[\frac{\kappa_{\text{eff,p}}}{l_p}\left(2Q_2^p\right)\right]+\frac{1}{l_p}\left[\frac{2\kappa_{\text{eff,p}}RT}{Fc_0}\frac{\left(1-t_+\right)}{l_p}\left(2A_2^p\right)\right]=0$$
$$\frac{1}{l_p}\left[\frac{-\sigma_{\text{eff,p}}}{l_p}\left(2E_2^p\right)\right]-\frac{1}{l_p}\left[\frac{\kappa_{\text{eff,p}}}{l_p}\left(2R_2^p\right)\right]+\frac{1}{l_p}\left[\frac{2\kappa_{\text{eff,p}}RT}{Fc_0}\frac{\left(1-t_+\right)}{l_p}\left(2B_2^p\right)\right]=0 \tag{A.41}$$

$$\frac{1}{l_p}\left[\frac{\sigma_{\text{eff,p}}}{l_p}\left(2C_2^p\right)\right]=a_{\text{p}}F\left(\frac{i0_p\left(\alpha_A+\alpha_C\right)}{RT}\left(\left(\varphi'_{p,2}\right)-\left(\psi'_{p,2}\right)-dUdC_p*cps'\right)-\frac{\omega Cdl_p}{F}\left(\left(\varphi''_{p,2}\right)-\left(\psi''_{p,2}\right)\right)\right)$$
$$\frac{1}{l_p}\left[\frac{\sigma_{\text{eff,p}}}{l_p}\left(2E_2^p\right)\right]=a_{\text{p}}F\left(\frac{i0_p\left(\alpha_A+\alpha_C\right)}{RT}\left(\left(\varphi''_{p,2}\right)-\left(\psi''_{p,2}\right)-dUdC_p*cps''\right)+\frac{\omega Cdl_p}{F}\left(\left(\varphi'_{p,2}\right)-\left(\psi'_{p,2}\right)\right)\right) \tag{A.42}$$

Where cps' and cps'' are the real and imaginary parts of the surface concentrations of the particle in the solid-phase respectively in the positive electrode, and similar to the negative electrode, are given by the analytical solution of the solid-phase equations.

The additional boundary conditions at the separator-cathode interface are given by:

$$\frac{-D_{\text{eff,s}}}{l_s}\left(A_1^s+2A_2^s\left(1\right)\right)=\frac{-D_{\text{eff,p}}}{l_p}\left(A_1^p\right)$$
$$\frac{-D_{\text{eff,s}}}{l_s}\left(B_1^s+2B_2^s\left(1\right)\right)=\frac{-D_{\text{eff,p}}}{l_p}\left(B_1^p\right)$$
$$\frac{-\kappa_{\text{eff,s}}}{l_s}\left(Q_1^s+2Q_2^s\left(1\right)\right)=\frac{-\kappa_{\text{eff,p}}}{l_p}\left(Q_1^p\right) \tag{A.43}$$
$$\frac{-\kappa_{\text{eff,s}}}{l_s}\left(R_1^s+2R_2^s\left(1\right)\right)=\frac{-\kappa_{\text{eff,p}}}{l_p}\left(R_1^p\right)$$
$$\left(C_1^p\right)=0$$
$$\left(E_1^p\right)=0$$

The remaining boundary conditions at the cathode current collector are given by:

$$
\begin{aligned}
&A_1^p + 2\,A_2^p(1) = 0 \\
&B_1^p + 2\,B_2^p(1) = 0 \\
&\frac{1}{l_p}\left(Q_1^p + 2Q_2^p(1)\right) = 0 \\
&\frac{1}{l_p}\left(R_1^p + 2R_2^p(1)\right) = 0 \\
&\left(\frac{1}{l_p}\left(C_1^p + 2C_2^p(1)\right)\right) = -\frac{I}{\sigma_{eff,p}} \\
&\left(\frac{1}{l_p}\left(E_1^p + 2E_2^p(1)\right)\right) = 0
\end{aligned}
\tag{A.44}
$$

The resulting set of equations (A.10)-(A.15) and (A.19)-(A.44) can now be solved simultaneously to obtain all the unknowns of the system. The linear impedance of the battery is given by:

$$
\begin{aligned}
&\mathrm{Re}\left(\bar{Z}\right) = \left|\frac{\varphi'_{p,1} - \varphi'_{n,N+2}}{I}\right| \\
&\mathrm{Im}\,g\left(\bar{Z}\right) = \left|\frac{\varphi''_{p,1} - \varphi''_{n,N+2}}{I}\right|
\end{aligned}
\tag{A.45}
$$

Appendix B

Analytical solution for solid-phase equations

The dynamics of diffusion inside the solid particles for constant diffusivity is represented in the spherical coordinates by the equation:

$$\frac{\partial c_i^s}{\partial t} = \frac{1}{r^2}\frac{\partial}{\partial r}\left[r^2 D_i^s \frac{\partial c_i^{s\,'}}{\partial r} \right] \tag{B.1}$$

Applying Fourier transform, the following equations can be derived for the respective real and imaginary parts:

$$\begin{aligned} -\omega c_i^{s\,''} &= \frac{1}{r^2}\frac{\partial}{\partial r}\left[r^2 D_i^s \frac{\partial c_i^{s\,'}}{\partial r} \right] \\ \omega c_i^{s\,'} &= \frac{1}{r^2}\frac{\partial}{\partial r}\left[r^2 D_i^s \frac{\partial c_i^{s\,''}}{\partial r} \right] \end{aligned} \tag{B.2}$$

With the corresponding boundary conditions given by:

$$\begin{aligned} &\left.\frac{\partial c_i^{s\,'}}{\partial r}\right|_{r=0} = 0 \\ &\left.\frac{\partial c_i^{s\,''}}{\partial r}\right|_{r=0} = 0 \\ &-D_i^s \left.\frac{\partial c_i^{s\,'}}{\partial r}\right|_{r=R_i} = j'_i \\ &-D_i^s \left.\frac{\partial c_i^{s\,''}}{\partial r}\right|_{r=R_i} = j''_i \end{aligned} \tag{B.3}$$

The following equation can be derived using a simple variable transformation as shown:

$$
\begin{aligned}
-w^2 cim(Y) &= \frac{d^2}{dY^2} cre(Y) \\
w^2 cre(Y) &= \frac{d^2}{dY^2} cim(Y)
\end{aligned}
\tag{B.4}
$$

Where the new variables are given by the relations:

$$
\begin{aligned}
Y &= \frac{r}{R_i} \\
cre(Y) &= Y \bullet c_i^s{}'(r) \\
cim(Y) &= Y \bullet c_i^s{}''(r) \\
w &= \sqrt{\frac{\omega R_i^2}{D_i^s}}
\end{aligned}
\tag{B.5}
$$

The boundary conditions for the transformed variables $cre(Y)$ and $cim(Y)$ at $Y = 0$ are given by:

$$
\begin{aligned}
cre(Y)\big|_{Y=0} &= 0 \bullet c_i^s{}'(r) = 0 \\
cim(Y)\big|_{Y=0} &= 0 \\
\left.\frac{d\, cre(Y)}{dY}\right|_{Y=0} &= \beta \\
\left.\frac{d\, cim(Y)}{dY}\right|_{Y=0} &= \delta
\end{aligned}
\tag{B.6}
$$

Where β and δ are unknowns to be determined.

The analytical solution for equation (B.4) and boundary conditions (B.6) is given by:

$$
\begin{aligned}
cre(Y) &= \frac{\sqrt{2}\begin{pmatrix} \cosh\left(1/2\sqrt{2}wY\right)\sin\left(1/2\sqrt{2}wY\right)\beta - \cosh\left(1/2\sqrt{2}wY\right)\sin\left(1/2\sqrt{2}wY\right)\delta \\ + \sinh\left(1/2\sqrt{2}wY\right)\cos\left(1/2\sqrt{2}wY\right)\beta + \sinh\left(1/2\sqrt{2}wY\right)\cos\left(1/2\sqrt{2}wY\right)\delta \end{pmatrix}}{2w} \\
cim(Y) &= \frac{\sqrt{2}\begin{pmatrix} \cosh\left(1/2\sqrt{2}wY\right)\sin\left(1/2\sqrt{2}wY\right)\beta + \cosh\left(1/2\sqrt{2}wY\right)\sin\left(1/2\sqrt{2}wY\right)\delta \\ - \sinh\left(1/2\sqrt{2}wY\right)\cos\left(1/2\sqrt{2}wY\right)\beta + \sinh\left(1/2\sqrt{2}wY\right)\cos\left(1/2\sqrt{2}wY\right)\delta \end{pmatrix}}{2w}
\end{aligned}
\tag{B.7}
$$

This relation can be used to obtain the original variables as:

$$c_i^s{}'(r) = \frac{cre(Y)}{Y} = \frac{\sqrt{2}\begin{pmatrix}\cosh\left(1/2\sqrt{2}wY\right)\sin\left(1/2\sqrt{2}wY\right)\beta - \cosh\left(1/2\sqrt{2}wY\right)\sin\left(1/2\sqrt{2}wY\right)\delta \\ + \sinh\left(1/2\sqrt{2}wY\right)\cos\left(1/2\sqrt{2}wY\right)\beta + \sinh\left(1/2\sqrt{2}wY\right)\cos\left(1/2\sqrt{2}wY\right)\delta\end{pmatrix}}{2wY}$$

$$c_i^s{}''(r) = \frac{cim(Y)}{Y} = \frac{\sqrt{2}\begin{pmatrix}\cosh\left(1/2\sqrt{2}wY\right)\sin\left(1/2\sqrt{2}wY\right)\beta + \cosh\left(1/2\sqrt{2}wY\right)\sin\left(1/2\sqrt{2}wY\right)\delta \\ - \sinh\left(1/2\sqrt{2}wY\right)\cos\left(1/2\sqrt{2}wY\right)\beta + \sinh\left(1/2\sqrt{2}wY\right)\cos\left(1/2\sqrt{2}wY\right)\delta\end{pmatrix}}{2wY}$$

(B.8)

The real and imaginary parts of the surface concentration of the particle is defined as:

$$cis' = c_i^s{}'(r)\Big|_{r=R_i} = \frac{cre(Y)}{Y}\Big|_{Y=1} = \frac{\sqrt{2}\begin{pmatrix}\cosh\left(1/2\sqrt{2}w\right)\sin\left(1/2\sqrt{2}w\right)\beta - \cosh\left(1/2\sqrt{2}w\right)\sin\left(1/2\sqrt{2}w\right)\delta \\ + \sinh\left(1/2\sqrt{2}w\right)\cos\left(1/2\sqrt{2}w\right)\beta + \sinh\left(1/2\sqrt{2}w\right)\cos\left(1/2\sqrt{2}w\right)\delta\end{pmatrix}}{2w}$$

$$cis'' = c_i^s{}''(r)\Big|_{r=R_i} = \frac{cim(Y)}{Y}\Big|_{Y=1} = \frac{\sqrt{2}\begin{pmatrix}\cosh\left(1/2\sqrt{2}w\right)\sin\left(1/2\sqrt{2}w\right)\beta + \cosh\left(1/2\sqrt{2}w\right)\sin\left(1/2\sqrt{2}w\right)\delta \\ - \sinh\left(1/2\sqrt{2}w\right)\cos\left(1/2\sqrt{2}w\right)\beta + \sinh\left(1/2\sqrt{2}w\right)\cos\left(1/2\sqrt{2}w\right)\delta\end{pmatrix}}{2w}$$

(B.9)

The boundary conditions at $r = R_i$ contains and j''_i, which are functions of cis' and cis'' respectively. Same conditions are used to obtain the unknown variables β and δ. From Table 5-2, after substituting the expressions for j'_i, j''_i, η'_i and η''_i, the boundary conditions can be rewritten as:

$$\left.\frac{\partial c_i^s{}'}{\partial r}\right|_{r=R_i} = -\frac{j'_i}{D_i^s} = A_1 + B_1\left(cis'\right)$$
$$\left.\frac{\partial c_i^s{}''}{\partial r}\right|_{r=R_i} = -\frac{j''_i}{D_i^s} = A_2 + B_2\left(cis''\right) \qquad \text{(B.10)}$$

Where A_1, B_1, A_2 *and* B_2 are given by:

$$A_1 = -\frac{i0_i R_i\left(\alpha_a + \alpha_c\right)\left(\Phi'_{1,i} - \Phi'_{2,i}\right)}{RTD_i^s}$$
$$B_1 = \frac{i0_i R_i\left(\alpha_a + \alpha_c\right) dUdC_i}{RTD_i^s}$$
$$A_2 = -\frac{i0_i R_i\left(\alpha_a + \alpha_c\right)\left(\Phi''_{1,i} - \Phi''_{2,i}\right)}{RTD_i^s} \qquad \text{(B.11)}$$
$$B_2 = \frac{i0_i R_i\left(\alpha_a + \alpha_c\right) dUdC_i}{RTD_i^s}$$

Equation (B.8) is used to calculate the slope of $c_i^s{}'$ and $c_i^s{}''$ required in equation (B.10), which is then solved simultaneously with equation (B.9) to get the required unknowns β and δ. The last step is too complicated to be written here, but can be performed using a symbolic mathematical tool, such as *Mathematica* or *Maple*. Once β and δ are known, equation (B.9) can be used to calculate the surface concentration, and the effect of the pseudo radial coordinate can be decoupled.